Probing brain microstructure with multidimensional diffusion MRI: Encoding, interpretation, and the role of exchange

Lampinen, Björn

2021

Document Version:
Publisher's PDF, also known as Version of record

Probing brain microstructure with multidimensional diffusion MRI:

Encoding, interpretation, and the role of exchange

BJÖRN LAMPINEN
DEPARTMENT OF MEDICAL RADIATION PHYSICS | LUND UNIVERSITY

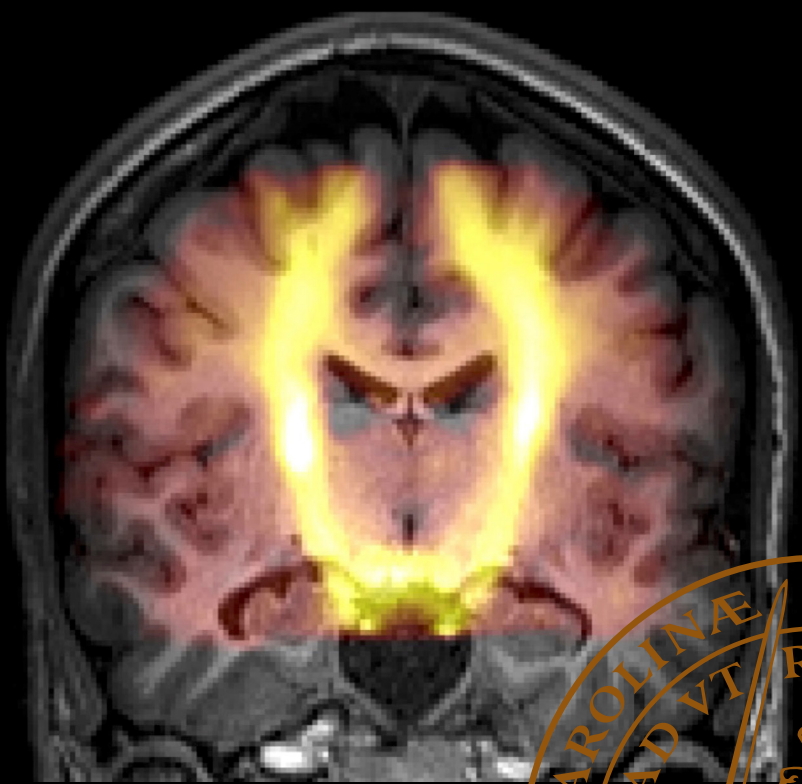

Probing brain microstructure with multidimensional diffusion MRI:
Encoding, interpretation, and the role of exchange

Probing brain microstructure with multidimensional diffusion MRI: Encoding, interpretation, and the role of exchange

Björn Lampinen

LUND
UNIVERSITY

DOCTORAL DISSERTATION

by due permission of the Faculty of Science, Lund University, Sweden.
To be defended at Skåne University Hospital in Lund, lecture hall 2, on Thursday, October 28, 2021 at 13:00.

Faculty opponent
Dr Susie Huang, Athinoula A. Martinos Center for Biomedical Imaging,
Department of Radiology, Massachusetts General Hospital,
Harvard Medical School, Boston, MA, USA

Organization	Document name
LUND UNIVERSITY Faculty of Sciences Clinical Sciences Lund Department of Medical Radiation Physics	DOCTORAL DISSERTATION **Date of disputation** 2021-10-28
Author Björn Lampinen	Sponsoring organization

Title and subtitle

Probing brain microstructure with multidimensional diffusion MRI: Encoding, interpretation, and the role of exchange

Abstract

Diffusion MRI (dMRI) is a non-invasive probe of human brain microstructure. It is a long-standing promise to use dMRI for 'in vivo histology' and estimate tissue quantities. However, this faces several challenges. First, the microstructure models used for dMRI data are based on assumptions that may cause erroneous interpretations. Also, probing neurites in gray matter assumes high microscopic diffusion anisotropy in both axons and dendrites, which is not supported by evidence. Furthermore, dMRI data analysis typically ignores diffusional exchange between microscopic environments. This thesis investigates and addresses these challenges using 'multidimensional' dMRI techniques that vary additional sequence encoding parameters to obtain new information on the tissue.

In Paper I, we optimized an acquisition protocol for filter exchange imaging (FEXI). We found slow rates of diffusional exchange in normal brain tissue. In patients with gliomas and meningiomas, faster exchange was tentatively associated with higher tumor grade.

In Paper II, we used tensor-valued diffusion encoding to test the NODDI microstructure model. The NODDI assumptions were contradicted by independent data and parameter estimates were found to be biased in normal brain and in gliomas. The CODIVIDE model combined data acquired with different b-tensor shapes to remove NODDI assumptions and reduce the susceptibility to bias.

In Paper III, we used tensor-valued diffusion encoding with multiple echo times to investigate challenges in estimating neurite density. We found that microscopic anisotropy in the brain reflected axons but not dendrites. We could not separate the densities and T_2 values of a two-component model in normal brain, but we did detect different component T_2 values in white matter lesions. Microstructure models ranked regions from normal brain and white matter lesions inconsistently with respect to neurite density.

In Paper IV, we optimized an acquisition protocol for tensor-valued diffusion encoding with multiple echo times. The data allowed removing all assumptions on diffusion and T_2 relaxation from a two-component model. This increased the measurable parameters from two to six and reduced their susceptibility to bias. Data from the normal brain showed different component T_2 values and contradicted common model assumptions.

In Paper V, we used tensor-valued diffusion encoding in malformations of cortical development. Lesions that appeared gray matter-like in T_1- and T_2-weighted contrasts featured white matter-like regions with high microscopic diffusion anisotropy. We interpreted these regions as myelin-poor white matter with a high axonal content. By primarily reflecting axons and not dendrites or myelin, microscopic anisotropy may differentiate tissue where alterations to myelin confound conventional MRI contrasts.

In Paper VI, we used SDE with multiple diffusion times in patients with acute ischemic stroke. Subacute lesions exhibited elevated diffusional exchange that predicted later infarction. MD reduction was partially reversible and did not predict infarction. Diffusional exchange may improve definition of ischemic core and identify additional patients for late revascularization.

Key words		
Classification system and/or index terms		
Supplementary bibliographical information		**Language** English
ISSN and key title		**ISBN** 978-91-8039-037-8 (print) 978-91-8039-038-5 (pdf)
Recipient's notes	**Number of pages** 225	Price
	Security classification	

Signature  Date 2021-09-20

Probing brain microstructure with multidimensional diffusion MRI: Encoding, interpretation, and the role of exchange

Björn Lampinen

LUND
UNIVERSITY

Cover image adapted from Paper IV, Figure 7.

Lund University
Faculty of Science
Clinical Sciences Lund
Department of Medical Radiation Physics

978-91-8039-037-8 (printed)
978-91-8039-038-5 (pdf)

Printed in Sweden by Media-Tryck,
Lund University
Lund 2021

For Tomas

Table of Contents

Populärvetenskaplig sammanfattning

Magnetisk resonanstomografi (MR) tar bilder av människokroppens insida. MR-kamerans starka magnetfält skapar en magnetisering av kroppens vattenmolekyler som med hjälp av radiovågor fås att generera en bildsignal. Jämfört med datortomografi ger MR en överlägsen bildkontrast av hjärnan och utsätter den inte för farlig strålning. Med hjälp av ett stort antal bildsekvenser och 'viktningar' kan man också via MR få bildkontraster som återspeglar olika vävnadsegenskaper.

Diffusionsviktad MR (dMRI) ger en bildkontrast som återspeglar de kontinuerliga slumpmässiga (diffusiva) rörelserna hos kroppens vattenmolekyler. Eftersom dessa rörelser påverkas av tätheten och formen av cellmembran fångar dMRI vävnadens struktur på mikrometerskalan. Detta används kliniskt, till exempel, för att kartlägga kopplingar i hjärnans vitvävnad inför kirurgi eller för att snabbt detektera stroke. dMRI används också inom medicinsk forskning och neurovetenskap för att utforska mikroskopiska processer i både den normala och den sjuka hjärnan.

Det finns sedan länge en förhoppning om att i detalj kunna beskriva hjärnans mikroskopiska sammansättning med hjälp av dMRI—att kunna skatta form och täthet av hjärnans nervceller som en form av icke-invasivt vävnadsprov. Detta är dock behäftat med stora utmaningar. Till exempel bygger dagens modeller av hjärnans mikrostruktur på osäkra antaganden. Vidare baseras tolkningen av dMRI på närvaron av kraftigt olikriktad (anisotrop) diffusion, men det är inte klarlagt vilka strukturer som bidrar till detta. Diffusion leder dessutom till ett konstant utbyte av vatten mellan olika mikroskopiska miljöer, men detta tas normalt inte hänsyn till i tolkningen av dMRI.

Denna avhandling söker utforska och förbättra tolkningen av dMRI med hjälp av nya 'multidimensionella' dMRI-metoder. Dessa metoder kombinerar olika sekvensparametrar för att ta fram ny information om vävnaden. Multidimensionell dMRI kan, till exempel, skilja mellan cellform och variation i celltäthet i hjärnans komplexa gråvävnad, separera bidragen från mikroskopiska vävnadskomponenter med olika kemiska egenskaper, eller detektera och mäta diffusivt vattenutbyte.

Original papers

This thesis is based on six publications, which are referred to by Roman numerals.

I. **Lampinen B**, Szczepankiewicz F, van Westen D, Englund E, Sundgren PC, Lätt J, Ståhlberg F, Nilsson M. Optimal experimental design for filter exchange imaging: Apparent exchange rate measurements in the healthy brain and in intracranial tumors. *Magnetic Resonance in Medicine.* 2017;77(3):1104–1114

II. **Lampinen B**, Szczepankiewicz F, Mårtensson J, van Westen D, Sundgren PC, Nilsson M. Neurite density imaging versus imaging of microscopic anisotropy in diffusion MRI: A model comparison using spherical tensor encoding. *NeuroImage.* 2017;147:517–531.

III. **Lampinen B**, Szczepankiewicz F, Novén M, van Westen D, Hansson O, Englund E, Mårtensson J, Westin C-F, Nilsson M. Searching for the neurite density with diffusion MRI: Challenges for biophysical modeling. *Human Brain Mapping*. 2019;40(8):2529–2545.

IV. **Lampinen B**, Szczepankiewicz F, Mårtensson J, van Westen D, Hansson O, Westin C-F, Nilsson M. Towards unconstrained compartment modeling in white matter using diffusion-relaxation MRI with tensor-valued diffusion encoding. *Magnetic Resonance in Medicine.* 2020;84(3): 1605–1623.

V. **Lampinen B**, Zampeli A, Björkman-Burtscher I, Szczepankiewicz F, Källén K, Compagno Strandberg M, Nilsson M. Tensor-valued diffusion MRI differentiates cortex and white matter in malformations of cortical development associated with epilepsy. *Epilepsia.* 2020;61(8):1701–1713.

VI. **Lampinen B**, Lätt J, Wasselius J, van Westen D, Nilsson M. Time dependence in diffusion MRI predicts tissue outcome in ischemic stroke patients. *Magnetic Resonance in Medicine.* 2021;86(2):754–764.

List of contributions

Below is a summary of my contributions to each published paper:

I. I participated in the study design, data acquisition, data analysis and statistical analysis. I wrote the code for the protocol optimization and the simulations. I was the main author of the paper.

II. I conceived the study and performed the theoretical and interpretational work together with the co-authors. I contributed to the CODIVIDE model. I performed the post-processing and data analysis. I wrote the code for the simulations. I was the main author of the paper.

III. I conceived the study and performed the theoretical and interpretational work together with the co-authors. I conceived the normalized residual variance test for degeneracy. I performed the post-processing and data analysis. I wrote the code for the simulations. I was the main author of the paper.

IV. I conceived the study and performed most of the theoretical work. I wrote the code for the protocol optimization and the simulations. I participated in sequence protocol implementation and data acquisition. I performed the post-processing and data analysis. I was the main author of the paper.

V. I participated in the study design. I performed the post-processing and the data analysis and contributed to data interpretation. I was the main author of the paper.

VI. I participated in the study design and contributed to data interpretation. I performed the post-processing, data analysis and statistical analysis. I wrote the main part of the paper.

Papers not included in this thesis

- Surova Y, Nilsson M, Lätt J, **Lampinen B**, Lindberg O, Hall S, Widner H, Nilsson C, Van Westen D, Hansson O. Disease-specific structural changes in thalamus and dentatorubrothalamic tract in progressive supranuclear palsy. *Neuroradiology*. 2015;57:1079–1091
- Surova Y, **Lampinen B**, Nilsson M, Lätt J, Hall S, Widner H, Van Westen D, Hansson O. Alterations of Diffusion Kurtosis and Neurite Density Measures in Deep Grey Matter and White Matter in Parkinson's Disease. *PLoS One*. 2016;11(6):e0157755
- Svard D, Nilsson M, **Lampinen B**, Lätt J, Sundgren PC, Stomrud E, Minthon L, Hansson O, Van Westen D. The effect of white matter hyperintensities on statistical analysis of diffusion tensor imaging in cognitively healthy elderly and prodromal Alzheimer's disease. *PLoS One*. 2017;12(9):e0185239
- Mattsson M, Eriksson O, Lindberg O, Schöll M, **Lampinen B**, Nilsson M, Insel PS, Lautner R, Strandberg O, Van Westen D, Zetterberg H, Blennow K, Palmqvist S, Stomrud E, Hansson O. Effects of APOE epsilon 4 on neuroimaging, cerebrospinal fluid biomarkers, and cognition in prodromal Alzheimer's disease. *Neurobiology of aging*. 2018;71:81–90
- Surova Y, Nilsson M, **Lampinen B**, Lätt J, Hall S, Widner H, Van Westen D, Hansson O. Alteration of putaminal fractional anisotropy in Parkinson's disease: a longitudinal diffusion kurtosis imaging study. *Neuroradiology*. 2018;60(3):247–254
- Andersson E, Janelidze S, **Lampinen B**, Nilsson M, Leuzy A, Stomrud E, Blennow K, Zetterberg H, Hansson O. Blood and cerebrospinal fluid neurofilament light differentially detect neurodegeneration in early Alzheimer's disease. *Neurobiology of aging*. 2020;95:143–153
- de Almeida Martins JP, Nilsson M, **Lampinen B**, Palombo M, While PT, Westin CF, Szczepankiewicz F. Neural Networks for parameter estimation in microstructural MRI: a study with a high-dimensional diffusion-relaxation model of white matter microstructure. *NeuroImage*. Accepted Sep 2021.

Conference abstracts

- **Lampinen B**, Szczepankiewicz F, Van Westen D, Sundgren PC, Ståhlberg F, Lätt J, Nilsson M. Protocol optimization of the double pulsed field gradient (d-PFG) based filter-exchange imaging (FEXI) sequence enables comparative studies of the diffusional apparent exchange rate (AXR) at reduced scan times and smaller group sizes. Oral presentation at ISMRM 21st Annual Meeting, Salt Lake City, UT, USA, 2013.
- **Lampinen B**, Szczepankiewicz F, Van Westen D, Sundgren PC, Ståhlberg F, Lätt J, Nilsson M. Apparent Exchange Rate (AXR) Mapping in Diffusion MRI: An In Vivo Test-Retest Study and Analysis of Statistical Power. Poster presentation at ISMRM 22nd Annual Meeting, Milan, Italy, 2014.
- **Lampinen B**, Van Westen D, Ståhlberg F, Lätt J, Hansson O, Nilsson M. Neurite Density Imaging (NDI): rapid acquisition and estimation of the intracellular volume fraction. Poster presentation at ISMRM 23rd Annual Meeting, Toronto, ON, Canada, 2015.
- **Lampinen B**, Szczepankiewicz F, Novén M, Westin C-F, Englund E, Mårtensson J, Nilsson M. Microscopic anisotropy in gray matter is evidence of myelinated axons but not dendrites? An in vivo study using diffusion MRI with variable shape of the b-tensor. Oral presentation at ISMRM 25th Annual Meeting, Honolulu, HI, USA, 2017.
- **Lampinen B**, Szczepankiewicz F, Topgaard D, Hansson O, Van Westen D, Nilsson M. Constrained analysis of b-tensor encoding diffusion data with multiple echo times allows estimation of compartment-specific T_2 relaxation times in white matter. Poster presentation at ISMRM 26th Annual Meeting, Paris, France, 2018.
- **Lampinen B**, Zampeli A, Szczepankiewicz F, Compagno Strandberg M, Källén K, Björkman-Burtscher IM, Nilsson M. Microscopic diffusion anisotropy reveals microstructural heterogeneity of malformations of cortical development associated with epilepsy: A b-tensor encoding study at 7T. Oral presentation at ISMRM 26th Annual Meeting, Paris, France, 2018.
- **Lampinen B**, Zampeli A, Szczepankiewicz F, Källén K, Compagno Strandberg M, Björkman-Burtscher I, Nilsson M. Diffusion MRI with tensor-valued diffusion encoding as a marker of axonal content within malformations of cortical development. Poster presentation at ISMRM Virtual Conference, 2020.
- **Lampinen B**, Szczepankiewicz F, Mårtensson J, van Westen D, Hansson O, Westin C-F, Nilsson M. Towards unconstrained compartment modeling in white matter using diffusion-relaxation MRI with tensor-valued diffusion encoding. Power pitch presentation at ISMRM Virtual Conference, 2020.
- **Lampinen B**, Lätt J, Wasselius J, van Westen D, Nilsson M. Diffusion time dependence and tissue outcome in ischemic stroke. Oral presentation at ISMRM Virtual Conference, 2020.

1 Introduction

Diffusion MRI (dMRI) is a non-invasive probe of brain tissue microstructure (Le Bihan 2003). By using magnetic field gradients to manipulate the magnetization of diffusing water protons (Stejskal et al. 1965b), diffusion-weighted MRI pulse sequences encode the random displacements of water molecules within a time window of milliseconds. In brain tissue, these displacements are determined by the shape and densities of cell membranes (Beaulieu 2002). The sensitivity of dMRI to tissue microstructure has had an important clinical impact (Sundgren et al. 2004). For example, dMRI captures early changes associated with ischemic stroke (Moseley et al. 1990, Albers 1999) and maps sensitive white matter connections in surgical planning (Mori et al. 1999, Romano et al. 2009). dMRI has also been widely used in research, for example, to detect microstructural alterations in the brain both due to disease (Werring et al. 1999, Horsfield et al. 2002, Goveas et al. 2015) and normal processes such as maturation (Lebel et al. 2008, Löbel et al. 2009) and learning (Scholz et al. 2009, Sagi et al. 2012, Zatorre et al. 2012).

It is a long-standing promise to use dMRI for 'in vivo histology' and estimate specific brain tissue quantities such as the volume fraction (density) of axons (Alexander et al. 2019). A major challenge, however, is that dMRI has low specificity for any given tissue feature. The information on tissue microstructure that is encoded by dMRI can be captured in a few parameters that describe the acquired signal. For example, the mean diffusivity from diffusion tensor imaging (Basser et al. 1994) and the mean kurtosis from diffusion kurtosis imaging (Jensen et al. 2005) capture the signal's initial slope and curvature with respect to the encoding b-value, respectively. These parameters reflect many microstructural features simultaneously and do not report directly on any tissue quantity. For example, a change in the mean kurtosis could reflect a change in axonal density (Fieremans et al. 2011), myelination (Falangola et al. 2014), cell density variation (Szczepankiewicz et al. 2016b), T_2 relaxation rates (Ning et al. 2019) or diffusional exchange (Ning et al. 2018).

Microstructure modeling, or 'biophysical modeling,' aims to estimate specific brain tissue quantities from dMRI data. The technique uses a forward model to separate the signal between different microstructural components, and estimates quantities associated with these components by fitting the model to acquired data (Nilsson et al. 2013b, Novikov et al. 2018a, Alexander et al. 2019, Jelescu et al. 2020). The ability to estimate quantities like the density of 'neurites' (axons and dendrites combined) has made microstructure modeling very

popular in brain research. Models like Neurite Orientation Dispersion and Density Imaging (NODDI) (Zhang et al. 2012) have been used to interpret changes to brain diffusion in a wide variety of conditions, including: glioma brain tumors (Wen et al. 2015), ischemic stroke (Wang et al. 2019), multiple sclerosis (Collorone et al. 2020), cortical dysplasia (Winston et al. 2014) and Alzheimer's disease (Colgan et al. 2016). However, despite the success of microstructure modeling, several important challenges remain in the interpretation of dMRI data.

Microstructure models require assumptions to separate the contributions from different tissue features to the dMRI signal. For example, models use parameter constraints that fix or interrelate the diffusion properties of different microstructural components (Jelescu et al. 2016a, Novikov et al. 2018b). In conditions where the assumptions do not hold true, they may bias the estimated parameters and cause errors in interpretation. For example, studies using NODDI have reported elevated neurite densities in the enhancing parts of high-grade gliomas (Wen et al. 2015, Zhao et al. 2018), where few neurites are expected (Szczepankiewicz et al. 2016b). Also, applying NODDI to acute ischemic stroke has suggested a sharp increase in the neurite density in the lesions (Caverzasi et al. 2016, Wang et al. 2019). To obtain parameters that are less susceptible to bias requires models based on fewer assumptions. However, to simply remove model assumptions generally results in degeneracy in model fitting (Jelescu et al. 2016a, Novikov et al. 2018b), meaning that the model parameters cannot be uniquely determined by the data. Thus, to reduce the risk of erroneous interpretations, model assumptions need to be replaced with independent data.

The interpretation of dMRI data in terms of 'neurites' is based on the property of microscopic diffusion anisotropy. However, this connection has not been experimentally established. Microscopic diffusion anisotropy is induced by environments where obstructions cause the rate of diffusion to be different across directions (Chenevert et al. 1990, Moseley et al. 1991). In white matter, a high level of microscopic anisotropy has been associated with the presence of axons (Beaulieu et al. 1994a, Beaulieu et al. 1994b, Beaulieu 2002)—reflecting a diffusional displacement that is free in the parallel direction but restricted by cell membranes in the perpendicular direction (McKinnon et al. 2017, Veraart et al. 2019). Accordingly, microstructure models of white matter represent axons with a 'stick' component with completely anisotropic diffusion (Behrens et al. 2003). When microstructure models have been extended to gray matter, the 'stick' component has been interpreted as representing neurites and thus dendrites as well as axons (Jespersen et al. 2007, Jespersen et al. 2010, Zhang et al. 2012, White et al. 2013, Kaden et al. 2016). This assumes that dendrites induce a similarly high microscopic anisotropy as axons, based on the rationale that both these structures are elongated membranous processes with small diameters. However, the evidence that dendrites do induce high microscopic anisotropy is inconclusive (Jespersen et al. 2007, Jespersen et al. 2010, Lawrenz et al. 2018, Novikov et al. 2018b, Veraart et al. 2020). Thus, the source of microscopic anisotropy in the brain needs to be elucidated.

The interpretation of dMRI data does typically not account for diffusional exchange, which refers to mixing of water molecules between different microscopic environments. The effects of diffusional exchange on dMRI data range between negligible and dramatic depending on the rate of exchange versus the timing of the experiment (Harkins et al. 2009). Although exchange of water occurs continuously in brain tissue (Amiry-Moghaddam et al. 2003), the evidence for its impact on dMRI in human brain is inconclusive. On the one hand, several studies have indicated negligible diffusion time dependence in normal brain (Clark et al. 2000, Clark et al. 2001, Lätt et al. 2009, Nilsson et al. 2009). On the other hand, diffusional exchange has been demonstrated in normal brain (Nilsson et al. 2013a, Nedjati-Gilani et al. 2017, Li et al. 2021) as well as in brain tumors (Nilsson et al. 2013a), ischemic stroke (Lätt et al. 2009) and multiple sclerosis (Nedjati-Gilani et al. 2017). Thus, to avoid interpretation errors or missing out on potentially clinically useful information, the role of diffusional exchange needs to be further investigated.

Multidimensional dMRI is an umbrella term for dMRI techniques that vary experimental parameters beyond the conventional b-value (Topgaard 2017, de Almeida Martins et al. 2018, Benjamini et al. 2020). This encodes additional tissue information into the data and allows the separation of features that are otherwise entangled. For example, most dMRI studies still use the diffusion-encoding design introduced by Stejskal et al. (1965b), which is also referred to as single diffusion encoding (SDE) (Shemesh et al. 2016). Because SDE only applies diffusion-encoding gradients in a single direction per signal readout, it entangles the shape of microscopic structures with their dispersion in orientations and their variance in isotropic diffusivities (Mitra 1995). Tensor-valued diffusion encoding separates these features by using gradient waveform designs to apply diffusion encoding in multiple directions per readout (Jespersen et al. 2013, Lawrenz et al. 2013, Lasič et al. 2014, Szczepankiewicz et al. 2015, Szczepankiewicz et al. 2016a, Szczepankiewicz et al. 2021). We refer to this as varying the shape of the b-tensor (Westin et al. 2014, Westin et al. 2016). Also, dMRI data is typically acquired using a single echo time. This entangles the volume fractions of tissue components with their signal contributions due to their T_2 relaxation rates (Paper III). Diffusion-relaxation MRI separates these features by acquiring dMRI data using multiple echo times (Beaulieu et al. 1998, Clark et al. 2000, Does et al. 2000, Benjamini et al. 2016, Veraart et al. 2017, de Almeida Martins et al. 2018, Ning et al. 2019, Slator et al. 2019). Furthermore, accounting for diffusional exchange is possible with SDE using multiple diffusion times (Kärger 1985). However, such data entangle diffusional exchange with restricted diffusion (Nilsson et al. 2009). Filter exchange imaging (FEXI) isolates the effects of exchange by using a double diffusion-encoding (DDE) design and varying the mixing time (Åslund et al. 2009, Lasič et al. 2011, Nilsson et al. 2013a).

In this thesis, we investigated four gaps in the current knowledge: First, to what degree do the additional data from multidimensional dMRI alleviate the need for assumptions in microstructure models? Second, to what extent can the interpretations suggested for microstructure model parameters be trusted? Third, what is the source of microscopic diffusion anisotropy in the brain? Fourth, what is the impact of diffusional exchange on dMRI in normal brain, and what is its clinical potential in intracranial tumors and in ischemic stroke? Our approach was to combine different multidimensional dMRI techniques in normal human brain and in brain pathologies. To this end, we used tensor-valued diffusion encoding, diffusion-relaxation MRI, SDE with multiple diffusion times, and FEXI to acquire data from normal brain tissue, white matter lesions, intracranial tumors, malformations of cortical development, and ischemic stroke.

2 Aims

The central subject of this thesis concerns the use of multidimensional dMRI to probe the microstructure of the living human brain. The thesis is structured around two main parts. The background part (Chapters 3–7) reviews important concepts on brain tissue microstructure, diffusion in a heterogeneous environment, diffusion encoding, and microstructure modeling. The results part (Chapters 8–12) reports, extends, and discusses results from Papers I–VI concerning the aims listed below.

The aims of this thesis were:

- To explore how multidimensional dMRI data alleviate the need for model assumptions on diffusion and T_2 relaxation, and to remove assumptions in vivo using efficient acquisition protocols (Papers II, III and IV).
- To investigate to what extent the interpretations suggested for microstructure model parameters can be trusted (Papers II, III and IV).
- To investigate the source of microscopic diffusion anisotropy in the brain (Papers II, III, IV and V).
- To assess the impact of diffusional exchange on dMRI in normal brain and to explore its clinical potential in intracranial tumors and ischemic stroke (Papers I and VI).

3 Brain tissue microstructure

Brain tissue microstructure primarily concerns the shape and density of cell membranes. It is a topic in-between neuroanatomy—which describes nervous structures on the centimeter-to-millimeter scale—and brain tissue ultrastructure, which describes subcellular structures on the nanometer scale.

3.1 Microstructural components of brain tissue

Key components of brain tissue microstructure are illustrated in Figure 3.1 and are reviewed below.

3.1.1 The neuron

The neuron is the principal cell of the nervous system and is specialized to receive, generate, and conduct electrical signals (Clark et al. 2010). The brain has two main types of neurons: the larger pyramidal neurons that form long-range connections between different parts of the nervous system, and the smaller stellate neurons that form short-range connections within local neural circuits (Braitenberg et al. 2013).

The neural cell bodies (soma, Figure 3.1A) have diameters between a few micrometers for stellate cells to between 10 and 100 µm for pyramidal cells (Braitenberg et al. 2013). The soma contains the nucleus whose dark genetic substance yields gray matter its appearance to the naked eye. The soma also features membranous processes in the form of multiple signal-receiving dendrites and one signal-conducting axon (Clark et al. 2010). Dendrites form branching structures that, for pyramidal neurons, measure a few 100 µm between base and tip, have an average segment length of 80 µm between branch points, and diameters from 10 µm at the base to between 0.5 and 2 µm at the distal end (Bennett 2013). The axon is a long a long process that originates from the soma at a region referred to as the axon hillock (Clark et al. 2010) and continues into white matter (pyramidal axons) or remains in gray matter (stellate axons). Axons in the gray matter of the cerebral cortex are highly branching and largely consist of thin collaterals with an average diameter of 0.4 µm (Bennett 2013).

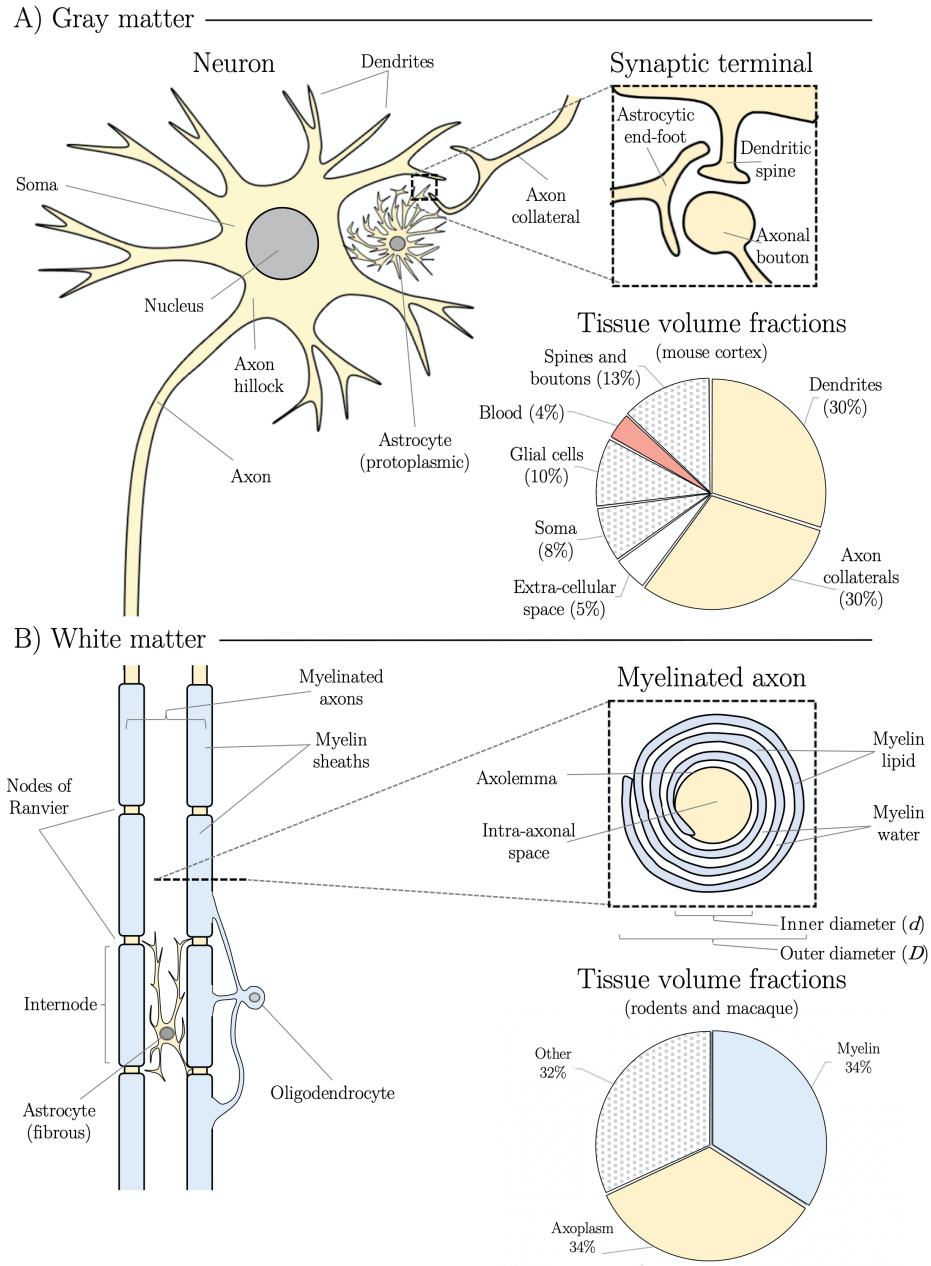

Figure 3.1 | Microstructural components of brain tissue. A) Gray matter contains the neurons' cell bodies (soma) with multiple dendrites and a single axon. The end-processes of axons (boutons) and dendrites (spines) form synaptic terminals that are enveloped by the end-feet of astrocyte glial cells. B) White matter contains axons covered by myelin sheaths from oligodendrocytes. Compacted membrane folds (myelin lipid) are wrapped around the axolemma and separated by narrow spaces (myelin water, excaggerated for ilustration). Pie charts show tissue component volume fractions from histology (Section 3.2).

3.1.2 The synaptic terminal

The dendrites of pyramidal cells and of most stellate cells are densely populated with up to 5000 'spines'—end-processes up to 3 µm long and 0.5 µm wide with a thin neck and a bulbous head (Figure 3.1A) (Bennett 2013). The most distal parts of axon collaterals branch further and form 'boutons'—end-processes approximately 0.6 µm in diameter (Bennett 2013). The spines and boutons combine to form synaptic terminals—the sites of the electrochemical couplings (synapses) that convey signals between neurons. Upon sufficient excitatory stimulation by axons, the soma generates an action potential at the axon hillock to form a new signal that is conducted distally along the axonal membrane (axolemma) and eventually reaches other neurons (Clark et al. 2010).

3.1.3 Myelinated axons

Myelinated axons are the principal component of white matter, where they form long-distance connections for rapid electric signalling between different cortical and subcortical structures (Clark et al. 2010). The high lipid content of the myelin sheaths yields white matter its appearance to the naked eye. Myelinated axons are present also in gray matter and in the cortex, where they appear on myelin stains as radial and tangential bands (with respect to the cortical surface) (Vogt 1910).

Myelin is produced by oligodendrocytes, a type of glial cells that have a cell body approximately 6–8 µm in diameter and a few membranous processes that may provide up to 60 myelin sheaths (Figure 3.1B) (Edgar et al. 2009). The myelin sheaths line up along the length of the axons with each internode covering between 100 and 1700 µm of axolemma (Hildebrand et al. 1993). The sheaths are separated by the 1–5 µm-wide nodes of Ranvier, where the axolemma is dense with ion channels that allow the propagation of action potentials (Trapp et al. 2004). Each myelin sheath consists of membrane folds that wrap around the axolemma up to 160 times to form a concentric spiral structure (Figure 3.1B) (Hildebrand et al. 1993). The myelin sheath's membranous, or lipid, portion is mostly compact with no remaining cytoplasm. It functions as an electrical insulator that increases the axon's conduction speed between 10- and 100-fold (Trapp et al. 2004). The myelin sheath's water portion is the narrow space between folds where the myelin is not fully compact (Edgar et al. 2009).

3.1.4 Astrocytes

Astrocytes are a type of glial cells that have a cell body approximately 9 µm in diameter and many membranous processes (McCaslin et al. 2011). In gray matter, the end-processes (end-feet) of protoplasmic astrocytes envelop all synaptic terminals (Figure 3.1A) where they support synaptic activity by regulating the extracellular balance in ions and neurotransmitters (Sofroniew et al. 2010). In white matter, fibrous astrocytes occupy the extracellular space between myelinated axons and contact the nodes of Ranvier with their long processes (Figure 3.1B) (Sofroniew et al. 2010).

3.2 Volume fractions of microstructural components

Approximate estimates of the volume fractions occupied by different microstructural components in brain tissue are reported from animal histology below and in Figure 3.1.

For cortical gray matter, volume fraction estimates from electron microscopy in mice are shown in Figure 3.1A (Ikari et al. 1981, Schüz et al. 1989, Chklovskii et al. 2002, Kasthuri et al. 2015). Neurites occupied almost two thirds of the space, with an even split between axons (30%) and dendrites (30%). The remaining space was occupied by neurite projections—dendritic spines and axonal boutons (13%)—as well as glial cells (10%), soma (8%), extracellular space (5%) and blood vessels (4%).

For white matter, volume fraction estimates from electron and light microscopy in guinea pigs, rats, macaque, and mice are shown in Figure 3.1B (Perge et al. 2009, Xu et al. 2014, Stikov et al. 2015, Jelescu et al. 2016b). Myelinated axons occupied approximately two thirds of the space, with an even split between intra-axonal space (34%) and myelin (34%). The composition of the remaining space is not detailed in all studies, although some report intra-axonal space of unmyelinated axons (15%) (Jelescu et al. 2016b), cell bodies and processes of astrocytes and oligodendrocytes (41%) (Perge et al. 2009) and extracellular space (2%) (Perge et al. 2009). According to PET data, white matter is composed of 2–3% blood vessels (Leenders et al. 1990).

The above numbers should be interpreted with caution. First, they are from studies on animals and not humans. Second, volume fractions in MRI voxels may be smaller due to partial volume effects with cerebrospinal fluid (CSF). Such partial volume effects are mostly expected in the cerebral cortex and periventricular white matter, although small amounts of CSF are present throughout brain tissue within the perivascular spaces surrounding blood vessels (Sepehrband et al. 2019). Third, the cortex is not homogeneous but features six histologically distinct layers with different microstructural composition (Bennett 2013). However, this layering is not resolved in the millimeter-sized voxels of clinical dMRI.

Fourth, the volume fractions of extracellular space reported in histology are markedly smaller than the approximately 20% estimated in vivo using tracer-diffusion studies (Syková et al. 2008). This may reflect negative bias of histology estimates from fixation-induced swelling (Van Harreveld et al. 1965) or positive bias of tracer-diffusion estimates from conflating extracellular space with astrocytes that are interconnected by gap junctions (Sofroniew et al. 2010).

3.2.1 The volume fractions associated with myelinated axons

The volume fraction of myelinated axons (v_{MA}) is a composite quantity (Figure 3.1B). It is related to the volume fractions of the intra-axonal space (v_{IA}), myelin (v_{M}), myelin lipid (v_{ML}) and myelin water (v_{MW}), according to

$$\begin{aligned} v_{\mathrm{MA}} &= v_{\mathrm{IA}} + v_{\mathrm{M}}, \text{where} \\ v_{\mathrm{M}} &= v_{\mathrm{ML}} + v_{\mathrm{MW}}. \end{aligned} \tag{3.1}$$

The volume fractions of intra-axonal space (v_{IA}) and myelin (v_{M}) are related by the g-ratio between the (inner) diameter of the axolemma (d) and the (outer) diameter of the myelin sheath (D, Figure 3.1), according to

$$g = \sqrt{\frac{v_{\mathrm{IA}}}{v_{\mathrm{IA}} + v_{\mathrm{M}}}} = \sqrt{\frac{v_{\mathrm{IA}}}{v_{\mathrm{MA}}}} = \frac{d}{D}, \tag{3.2}$$

assuming parallel and cylindrical structures. The g-ratio theoretically has a range from zero (only myelin) to unity (no myelin). In human white matter, estimates of the g-ratio are approximately 0.6, possibly reflecting an optimal balance between conduction speed and size restrictions (Rushton 1951, Perge et al. 2009).

The volume fractions of myelin lipid (v_{ML}) and myelin water (v_{ML}) are expected to be proportional, although no clear relation has been established. Stikov et al. (2015) combined magnetization-transfer MRI with electron microscopy in the corpus callosum of the macaque to estimate $v_{\mathrm{ML}} \approx 1.6 v_{\mathrm{MW}}$. With an estimated myelin volume fraction $v_{\mathrm{M}} \approx 0.4$, this corresponded to $v_{\mathrm{ML}} \approx 0.25$ and $v_{\mathrm{MW}} \approx 0.15$. Furthermore, an estimated intra-axonal volume fraction $v_{\mathrm{IA}} \approx 0.3$ yielded a total volume fraction of myelinated axons $v_{\mathrm{MA}} \approx 0.7$.

4 Mathematical concepts

This chapter defines important mathematical concepts and relationships that simplify the reading of the subsequent chapters. The first section defines tensors and tensor operators, which are later used to describe diffusion and tensor-valued diffusion encoding. The second section defines moments and cumulants of probability distributions, which are later used to describe diffusion tensors and relaxation rates, as well as the precession phase, displacement, and velocity of spins.

4.1 Tensor algebra

Tensors are mathematical objects composed of scalar elements that describe multilinear relationships (Comon 2014). This thesis considers tensors of four different orders, which is the number of indices required to specify an element. Zeroth-order tensors are scalars represented by italic letters, for example; diffusion coefficient $D_{\mathbf{r}}$ or b-tensor trace b. First-order tensors are vectors represented by boldface lowercase letters, for example; displacement $\mathbf{r}$ or symmetry axis $\mathbf{u}$. Second-order tensors are represented by 3×3 matrices in boldface capital letters, for example; diffusion tensor $\mathbf{D}$ or b-tensor $\mathbf{B}$. Fourth-order tensors are represented by $3 \times 3 \times 3 \times 3$ matrices in blackboard bold capital letters, for example, diffusion covariance tensor $\mathbb{C}$. Tensors of unspecified order are represented by a roman lowercase t.

4.1.1 Inner and outer tensor products

The Frobenius inner product between two tensors of order > 1 is designated by the 'double-dot' operator (:). For two tensors of equal order and size, it yields a scalar that equals the sum of the tensor elements after point-wise multiplication. For example, the inner product between two second-order tensors $\mathbf{T}_{\mathrm{A}}$ and $\mathbf{T}_{\mathrm{B}}$ is given by

$$\mathbf{T}_\mathrm{A} \colon \mathbf{T}_\mathrm{B} = \sum_{i=1} \sum_{j=1} T_{\mathrm{A};ij} T_{\mathrm{B};ij}. \tag{4.1}$$

The outer product between two tensors is designated by the 'circled cross' operator ($\otimes$). For two tensors of order n and m, it yields an $n+m$ order tensor whose elements equal the different product combinations between the elements of the two tensors (Comon 2014). For example, the outer product between two second-order tensors $\mathbf{T}_\mathrm{A}$ and $\mathbf{T}_\mathrm{B}$ yields a fourth-order tensor with the elements

$$(\mathbf{T}_\mathrm{A} \otimes \mathbf{T}_\mathrm{B})_{ijkl} = T_{\mathrm{A};ij} T_{\mathrm{B};kl}. \tag{4.2}$$

The outer product of a tensor of unspecified order with itself is written as $\mathrm{t}^{\otimes 2}$.

4.1.2 Eigenvalue operators for second-order tensors

For a second-order tensor $\mathbf{T}$ with eigenvalues $\{\lambda_i\}_{i \in \{1\ 2\ 3\}}$, the eigenvalue expectancy is a third of the tensor trace, according to

$$\mathrm{E}_\lambda[\mathbf{T}] = \frac{1}{3} \sum_{i=1}^{3} \lambda_i, \tag{4.3}$$

and the population variance of the eigenvalues is defined as (Westin et al. 2016)

$$\mathrm{V}_\lambda[\mathbf{T}] = \frac{1}{3} \sum_{i=1}^{3} (\lambda_i - \mathrm{E}_\lambda[\mathbf{T}])^2. \tag{4.4}$$

The eigenvalue variance can be determined without calculating the eigenvalues, according to $\mathrm{V}_\lambda[\mathbf{T}] = \mathbf{T}^{\otimes 2} \colon \mathbb{E}_\mathrm{shear}$, where $\mathbb{E}_\mathrm{shear}$ is the 'shear' component of the fourth-order unit tensor $\mathbb{E}_\mathrm{I}$ (Westin et al. 2016).

4.1.3 Parameterization of axisymmetric second-order tensors

An axisymmetric second-order tensor represented by a 3×3 matrix has four degrees of freedom. By eigendecomposition, these degrees of freedom specify two rotationally invariant eigenvalues—the radial eigenvalue $T_\perp$ (duplicate) and the axial eigenvalue $T_\parallel$ (non-duplicate unless $T_\parallel = T_\perp$)—as well as two spherical coordinate angles for the rotational symmetry axis $\mathbf{n}$.

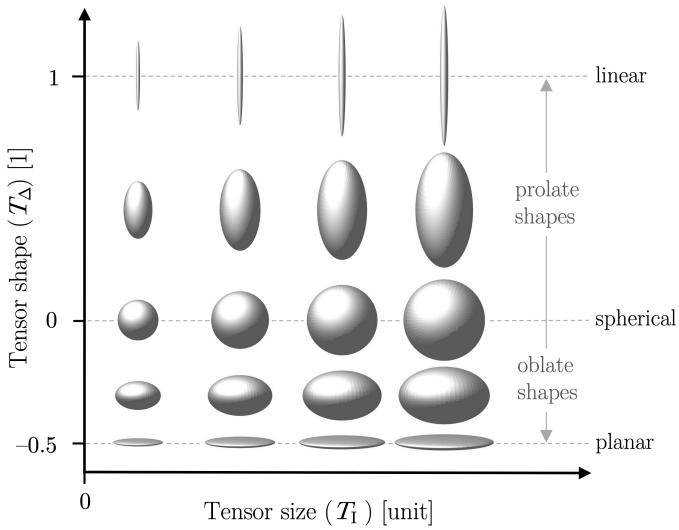

Figure 4.1 | The rotationally invariant properties of axisymmetric second-order tensors are represented by the (isotropic) tensor size (T_I) and the (anisotropic) tensor shape (T_Δ). The tensor size has the unit of the tensor elements and ranges between zero and arbitrarily large. The tensor shape is dimensionless and ranges between -0.5 (planar), through 0 (spherical) to 1 (linear), with the intermediate values corresponding to oblate ($-0.5 < T_\Delta < 1$) and prolate ($0 < T_\Delta < 1$) shapes.

We re-parameterize the two tensor eigenvalues as in Eriksson et al. (2015) (Figure 4.1) in terms of the tensor 'size,' the eigenvalue expectancy, given by

$$T_\mathrm{I} = \mathrm{E}_\lambda[\mathbf{T}] = \frac{1}{3}\left(T_\parallel + 2T_\perp\right), \tag{4.5}$$

and the tensor 'shape,' a normalized eigenvalue standard deviation given by

$$T_\Delta = \sqrt{\frac{\mathrm{V}_\lambda[\mathbf{T}]}{2\mathrm{E}_\lambda[\mathbf{T}]^2}} = \frac{T_\parallel - T_\perp}{3T_\mathrm{I}}. \tag{4.6}$$

Equivalently,

$$\begin{aligned} T_\perp &= T_\mathrm{I}(1 - T_\Delta) \text{ and} \\ T_\parallel &= T_\mathrm{I}(1 + 2T_\Delta). \end{aligned} \tag{4.7}$$

In the principal axis system where $\mathbf{T}$ is diagonal,

$$\mathbf{T} = \frac{T_\mathrm{I}}{3}\left[\mathbf{I} + T_\Delta \begin{vmatrix} -1 & 0 & 0 \\ 0 & -1 & 0 \\ 0 & 0 & 2 \end{vmatrix}\right], \tag{4.8}$$

where $\mathbf{I}$ is the identity matrix.

4.2 Moments and cumulants of probability distributions

For a probability distribution $P(\mathrm{t})$ of a stochastic tensor variable t, the first raw moment is the mean, given by (Kollo 2005)

$$\langle \mathrm{t} \rangle = \int \mathrm{t} P(\mathrm{t}) \, \mathrm{dt}. \tag{4.9}$$

The mean defines the distribution's *central moments* m_n according to

$$m_n = \int (\mathrm{t} - \langle \mathrm{t} \rangle)^{\otimes n} P(\mathrm{t}) \, \mathrm{dt}. \tag{4.10}$$

The second central moment m_2 is the distribution variance, given by

$$\mathrm{V}[\mathrm{t}] = \langle \mathrm{t}^{\otimes 2} \rangle - \langle \mathrm{t} \rangle^{\otimes 2}. \tag{4.11}$$

The distribution's *cumulants* c_n are related to its central moments. For the first four cumulants

$$\begin{aligned} c_1 &= m_1, \\ c_2 &= m_2, \\ c_3 &= m_3, \text{and} \\ c_4 &= m_4 - 3{m_2}^{\otimes 2}. \end{aligned} \tag{4.12}$$

5 Description of diffusion

Diffusion, or 'self-diffusion', of water refers to the continuous thermal motion of water molecules that does not result in net transport (Minati et al. 2007). The displacement path of a diffusing water molecule is shaped by constant collisions and referred to as a 'random walk.' The diffusional displacement for a single molecule during a given 'diffusion time' T_d is a stochastic variable $\mathbf{r}(T_\mathrm{d}) = \mathbf{r}_1 - \mathbf{r}_0$ described by a probability distribution $P(\mathbf{r}|T_\mathrm{d})$, referred to as the diffusion propagator.

All work in this thesis assumes diffusion in 'Gaussian environments,' meaning that the diffusional displacements are described by a Gaussian propagator $P(\mathbf{r}|T_\mathrm{d})$. For this to hold true, the displacements must be unrestricted (not fully confined) as well as homogeneous with respect to T_d. Homogeneity means that barriers within the environment affect all diffusing particles similarly during T_d. It can be expressed mathematically as $\tau_\mathrm{c} \ll T_\mathrm{d}$, where τ_c is the 'characteristic time' required for the initial and final velocities of a diffusing particle to become statistically independent. By this property, the displacement $\mathbf{r}(T_\mathrm{d})$ is a sum of many small independent displacements and the propagator $P(\mathbf{r}|T_\mathrm{d})$ is a Gaussian function by the central limit theorem (Van Kampen 1992). Investigation of the limits of assuming Gaussian diffusion in dMRI of the human brain is ongoing work (Henriques et al. 2020, Lee et al. 2020).

In this chapter, we describe diffusion in a single Gaussian environment by a diffusion tensor and then describe diffusion in an ensemble of Gaussian environments by a diffusion tensor distribution (DTD).

5.1 A single Gaussian environment: The diffusion tensor

In a Gaussian environment, diffusional displacement during the diffusion time T_d is described by a propagator on the form

$$P(\mathbf{r}|T_\mathrm{d}) = \frac{1}{\sqrt{|\mathbf{D}|(4\pi T_\mathrm{d})^3}} \exp\left(-\frac{\mathbf{r}^{\otimes 2}\!:\mathbf{D}^{-1}}{4T_\mathrm{d}}\right), \tag{5.1}$$

where $|\mathbf{D}|$ and $\mathbf{D}^{-1}$are the determinant and inverse of the diffusion tensor $\mathbf{D}$, respectively (Minati et al. 2007). The diffusion tensor is a symmetric positive-definite 3×3 matrix given by (Boss et al. 1965, Basser et al. 1994)

$$\mathbf{D} = \begin{pmatrix} D_{\mathrm{xx}} & D_{\mathrm{xy}} & D_{\mathrm{xz}} \\ D_{\mathrm{yx}} & D_{\mathrm{yy}} & D_{\mathrm{yz}} \\ D_{\mathrm{zx}} & D_{\mathrm{zy}} & D_{\mathrm{zz}} \end{pmatrix}. \tag{5.2}$$

This thesis considers axisymmetric diffusion tensors with rotationally invariant properties parameterized by the tensor size (isotropic diffusivity) D_I (Eq. 4.5) and the tensor shape (anisotropy) D_Δ (Eq. 4.6; Figure 4.1) (Eriksson et al. 2015).

The diffusion tensor is proportional to the variance of $P(\mathbf{r})$, according to

$$\mathrm{V}[\mathbf{r}] = \langle \mathbf{r}^{\otimes 2} \rangle - \langle \mathbf{r} \rangle^{\otimes 2} = 2T_\mathrm{d}\mathbf{D}, \tag{5.3}$$

where $\langle \mathbf{r} \rangle = 0$ by the condition of zero net transport. In any normalized direction $\mathbf{u}$, the diffusion coefficient, or diffusivity, with unit m^2/s describes the rate of mean squared displacement, according to

$$D_\mathrm{u} = \mathbf{u}^{\otimes 2}\!:\mathbf{D} = \frac{\langle r_\mathrm{u}^2 \rangle}{2T_\mathrm{d}}. \tag{5.4}$$

The standard deviation of the displacement during T_d is referred to as the 'diffusion length,' given by (Einstein 1905)

$$l_\mathrm{u} = \sqrt{2D_\mathrm{u}T_\mathrm{d}}. \tag{5.5}$$

5.2 An ensemble of non-exchanging Gaussian environments: The diffusion tensor distribution (DTD)

In an ensemble of non-exchanging Gaussian environments, the diffusional displacements in each environment follow a single Gaussian distribution described by a single propagator $P(\mathbf{r}|T_\mathrm{d})$ (Eq. 5.1) and diffusion tensor $\mathbf{D}$ (Eq. 5.2). However, the diffusional displacements of the whole ensemble follow different Gaussian distributions described by a DTD—a probability distribution $P(\mathbf{D})$ over the space of diffusion tensors, where is $\mathbf{D}$ a stochastic variable (Mitra 1995, Basser et al. 2003, Jian et al. 2007, Westin et al. 2014, Westin et al. 2016).

5.2.1 Statistical properties of the DTD

The mean of the DTD is the ensemble-average diffusion tensor $\langle\mathbf{D}\rangle$. The variance of the DTD is given by (Eq. 4.11)

$$\mathrm{V}[\mathbf{D}] = \langle\mathbf{D}^{\otimes 2}\rangle - \langle\mathbf{D}\rangle^{\otimes 2} = \mathbb{C}, \tag{5.6}$$

where the $3 \times 3 \times 3 \times 3$ matrix $\mathbb{C}$ is the fourth-order diffusion covariance tensor. It has 21 unique elements comprising the variances in the 6 unique tensor elements and the 15 covariances between these elements across $P(\mathbf{D})$ (Basser et al. 2007, Westin et al. 2016).

5.2.2 Scalar rotational invariants of the DTD

Tensor scalar rotational invariants can be obtained by inner products with isotropic tensors of the appropriate order. The ensemble-average diffusion tensor $\langle\mathbf{D}\rangle$ has one scalar rotational invariant; its eigenvalue expectancy (Eq. 4.3), or mean diffusivity (MD), given by (Westin et al. 2016)

$$\langle\mathbf{D}\rangle{:}\frac{1}{3}\mathbf{I} = \mathrm{E}_\lambda[\langle\mathbf{D}\rangle] = \mathrm{MD}. \tag{5.7}$$

The diffusion covariance tensor $\mathbb{C}$ has two scalar rotational invariants corresponding to inner products with the two orthogonal components of the fourth-order isotropic tensor $\mathbb{E}_\mathrm{I}$ (which is diagonal with the elements 1/3). The 'bulk' component, $\mathbb{E}_\mathrm{bulk} = {\mathbb{E}_\mathrm{I}}^{\otimes 2}$, yields the isotropic diffusional variance (V_I), or 'isotropic heterogeneity' (Szczepankiewicz et al. 2016b), according to (Westin et al. 2016)

$$
\begin{aligned}
V_{\mathrm{I}} &= \langle \mathbf{D}^{\otimes 2} \rangle \colon \mathbb{E}_{\mathrm{bulk}} - \langle \mathbf{D} \rangle^{\otimes 2} \colon \mathbb{E}_{\mathrm{bulk}} \\
&= \langle \mathrm{E}_{\lambda}[\mathbf{D}]^2 \rangle - \mathrm{E}_{\lambda}[\langle \mathbf{D} \rangle]^2 \\
&= \mathrm{V}[D_{\mathrm{I}}],
\end{aligned}
\tag{5.8}
$$

which is the ensemble-variance in the diffusion tensors' isotropic diffusivities $\mathrm{V}[D_{\mathrm{I}}]$. The 'shear' component, $\mathbb{E}_{\mathrm{shear}} = \mathbb{E}_{\mathrm{I}} - \mathbb{E}_{\mathrm{bulk}}$, yields the shear variance (V_{S}), according to (Westin et al. 2016)

$$
\begin{aligned}
V_{\mathrm{S}} &= \langle \mathbf{D}^{\otimes 2} \rangle \colon \mathbb{E}_{\mathrm{shear}} - \langle \mathbf{D} \rangle^{\otimes 2} \colon \mathbb{E}_{\mathrm{shear}} \\
&= \langle \mathrm{V}_{\lambda}[\mathbf{D}] \rangle - \mathrm{V}_{\lambda}[\langle \mathbf{D} \rangle] \\
&= 5/2\, V_{\mu\mathrm{A}} - V_{\mathrm{MA}}.
\end{aligned}
\tag{5.9}
$$

The shear variance is a composite quantity. The *microscopic* anisotropic diffusional variance $V_{\mu\mathrm{A}} = 2/5 \, \langle \mathrm{V}_{\lambda}(\mathbf{D}) \rangle$ (Westin et al. 2016) reflects the ensemble-average of the diffusion tensors' eigenvalue variances (Eq. 4.4). The *macroscopic* anisotropic diffusional variance $V_{\mathrm{MA}} = \mathrm{V}_{\lambda}[\langle \mathbf{D} \rangle]$ is the eigenvalue variance of the ensemble-average diffusion tensor and reflects macroscopic anisotropy like the fractional anisotropy from diffusion tensor imaging (Westin et al. 2016).

5.2.3 Representation of diffusion in a voxel by a DTD

For diffusion times between 1 and 1000 ms, and free water at 37°C with $D_u \approx 3.0\ \mu\mathrm{m}^2/\mathrm{ms}$ (Mills 1973), the diffusion length (Eq. 5.5) ranges between 2 and 80 µm. This is several orders of magnitude smaller than the side of a dMRI image element (voxel), which ranges between 1 and 4 mm. Thus, under the assumption of no exchange between environments, each voxel contains a large ensemble of Gaussian environments that can be described by a DTD. Figure 5.1 shows two example voxels together with their corresponding DTDs and scalar rotational invariants.

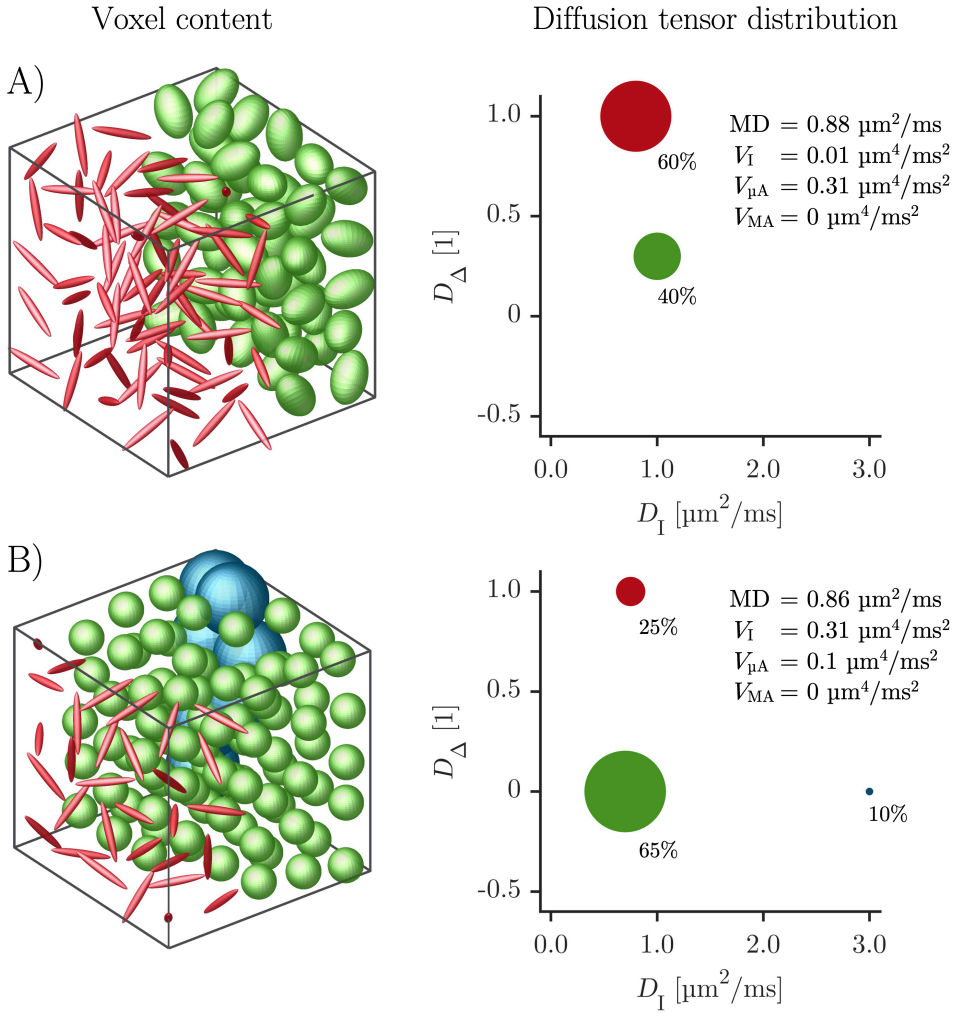

Figure 5.1 | The content within a voxel described as an ensemble of Gaussian environments (represented by diffusion tensors) together with the corresponding DTDs and scalar rotational invariants. The volume fractions of the different environments are indicated by percentages. A) Voxel with two different microscopic environments: one 'linear' (red, $D_I = 0.80$ µm²/ms, $D_\Delta = 1$) and one 'prolate' (green, $D_I = 1.00$ µm²/ms, $D_\Delta = 0.3$). In this voxel, diffusional variance is mostly due to microscopic anisotropy ($V_{µA}$). B) Voxel with three different microscopic environments: one 'linear' (red, $D_I = 0.75$ µm²/ms, $D_\Delta = 1$) and two 'spherical' (green, $D_I = 0.80$ µm²/ms, $D_\Delta = 0$; blue, $D_I = 3.00$ µm²/ms, $D_\Delta = 0$). In this voxel, diffusional variance is mostly due to differences in isotropic diffusivities (V_I).

6 Encoding of diffusion in MRI

The physical principles of MRI are described in detail in, for example, Plewes et al. (2012). Briefly, the strong magnetic field in the MRI scanner focuses the magnetic moments of proton spins and creates a net magnetization parallel to the field. To form an image signal, a radiofrequency (RF) pulse is applied whose frequency matches the spin precession frequency of water hydrogen protons. This redirects parallel magnetization to the transverse plane, perpendicular to the field, where it rotates and induces a detectable current within receive-coils. The rotational phase coherence among spins with transverse magnetization then decreases over time. This causes signal attenuation by destructive interference and yields an image contrast that depends on the 'relaxation properties' of tissue. In dMRI, magnetic field gradients are applied to induce an additional phase dispersion among diffusing spins to create a diffusion-weighted image contrast (Stejskal et al. 1965b, Le Bihan et al. 1986).

6.1 The diffusion-encoding pulse sequence

The basic composition of the spin-echo pulse sequence that is used for most dMRI acquisitions is illustrated in two examples in Figure 6.1. The sequence has three parts: the spin excitation by the 90° RF pulse, the spin refocusing by the 180° RF pulse, and the spin-echo readout using echo-planar imaging around the echo time (TE). Diffusion encoding is performed by the time-dependent magnetic field gradient waveform $\mathbf{g}(t)$. The effect of the gradients is, for Gaussian diffusion, fully described by the b-tensor, a symmetric 3×3 matrix given by

$$\mathbf{B} = \int_0^{\mathrm{TE}} \mathbf{q}(t)^{\otimes 2} dt, \tag{6.1}$$

where

$$\mathbf{q}(t) = \gamma \int_0^t \mathbf{g}(t')dt', \tag{6.2}$$

and γ is the gyromagnetic ratio (Westin et al. 2014). This thesis considers axisymmetric b-tensors that are parameterized in terms of the conventional b-factor $b = 3\mathrm{E}_\lambda[\mathbf{B}]$, b-tensor

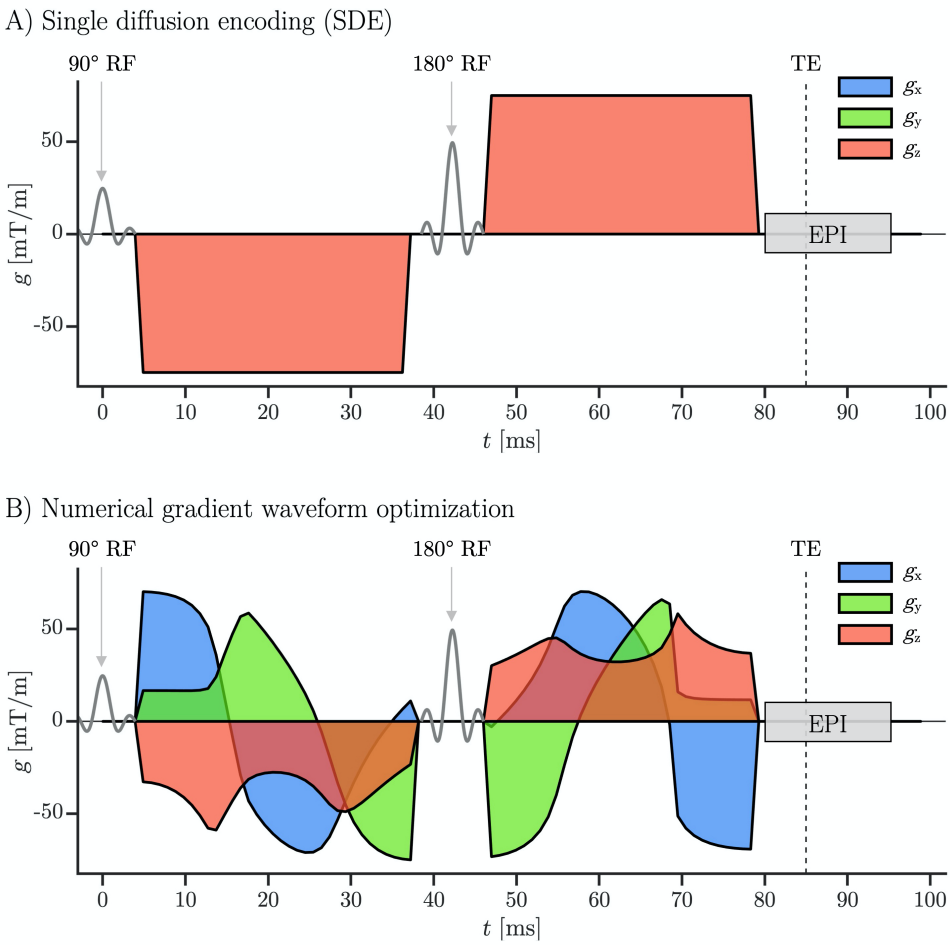

Figure 6.1 | The spin-echo pulse sequence used in dMRI. A signal is generated by the 90° RF pulse and refocused by the 180° RF pulse at the echo time (TE), where it is read out using echo-planar imaging (EPI). Diffusion encoding is applied by the gradient waveform $\mathbf{g}(t) = [g_x(t)\ g_y(t)\ g_z(t)]$. Different gradient waveform designs can yield b-tensors with different shapes (Figure 4.1). A) The conventional Stejskal-Tanner design (SDE) applies two trapezoidal gradient pulses in a single direction and yields LTE ($b_\Delta = 1$). B) Numerical gradient waveform optimization uses three-dimensional gradient waveforms and can yield any b-tensor shape. The example yields prolate tensor encoding ($b_\Delta = 0.6$) and is taken from Paper IV (protocol II).

shape b_Δ (Eq. 4.6), and the rotational symmetry axis $\mathbf{u}$. The diffusion encoding yielded by a given gradient waveform $\mathbf{g}(t)$ can be classified based on shape of the b-tensor (Figure 4.1), according to: linear tensor encoding (LTE), prolate tensor encoding, spherical tensor encoding (STE), oblate tensor encoding, and planar tensor encoding (PTE) (Szczepankiewicz et al. 2021).

Using different gradient waveform designs in the diffusion-encoding sequence (Figure 6.1) can yield b-tensors with different shapes (Figure 4.1) (Szczepankiewicz et al. 2021). The rank (number of non-zero eigenvalues) of the b-tensor equals the number of orthogonal basis vectors required to describe $\mathbf{g}(t)$. A rank-1 b-tensor is linear, a rank-2 b-tensor is planar (assuming axisymmetric $\mathbf{B}$) and a rank-3 b-tensor is prolate, spherical or oblate. The conventional Stejskal-Tanner design (SDE) applies two trapezoidal gradient pulses in a single direction (Figure 6.1A) (Stejskal et al. 1965a). This yields a rank-1 b-tensor and thus LTE. The double diffusion encoding (DDE) design applies two sets of trapezoidal gradient pulses in two directions (Cory et al. 1990, Özarslan 2009, Shemesh et al. 2010, Shemesh et al. 2016). This yields a rank ≤ 2 b-tensor and thus LTE or PTE. Triple diffusion encoding (Mori et al. 1995, Wong et al. 1995) and magic angle spinning of the q-vector (Eriksson et al. 2013) both yield a rank ≤ 3 b-tensor and thus any b-tensor shape. Another design that can yield any b-tensor shape is numerical gradient waveform optimization (Sjölund et al. 2015, Szczepankiewicz et al. 2018) (Figure 6.1B), which was used in Papers II–V.

6.2 The diffusion-weighted signal

The signal attenuation at the time of readout (TE) caused by phase dispersion among spins that diffuse in magnetic field gradients is given by

$$A = \langle \exp(-i\phi(\mathrm{TE})) \rangle, \tag{6.3}$$

where the average is across the complex transverse magnetization vectors of all individual spins with phase $\phi(\mathrm{TE})$. The spin phase is determined by the spin path $\mathbf{r}(t)$ and gradient waveform $\mathbf{g}(t)$, according to (Kiselev 2010)

$$\begin{aligned} \phi(\mathrm{TE}) &= \gamma \int_0^{\mathrm{TE}} \mathbf{g}(t) \cdot \mathbf{r}(t)\, dt \\ &= -\int_0^{\mathrm{TE}} \mathbf{q}(t) \cdot \mathbf{v}(t)\, dt, \end{aligned} \tag{6.4}$$

where $\mathbf{v}(t)$ is the spin velocity (using integration by parts).

The signal attenuation in Eq. 6.3 averages an exponential function of the stochastic phase variable ϕ, allowing it to be expressed in terms of the cumulants (Eq. 4.12) of the phase distribution $c_n(P(\phi))$, according to (Kiselev 2010)

$$\ln\langle\exp(-i\phi)\rangle = \sum_{n=1}^{\infty} \frac{i^n}{n!} c_n(P(\phi)). \tag{6.5}$$

The n^{th} phase cumulant is related to the n^{th} cumulant of the velocity distribution $c_n^v(\mathbf{v}_1 \otimes ... \mathbf{v}_n)$, according to (Kiselev 2010)

$$c_n(P(\phi)) = \int_0^{\text{TE}} (\mathbf{q}_1 \otimes ... \mathbf{q}_n) : c_n^v(\mathbf{v}_1 \otimes ... \mathbf{v}_n) dt_1 ... dt_n. \tag{6.6}$$

In the absence of spin flow, $P(\phi)$ is symmetric with non-zero c_n only for even n, and the diffusion-weighted signal is given by

$$S = S_0 \exp\Big(-\frac{1}{2}c_2 + \frac{1}{24}c_4 + \cdots\Big), \tag{6.7}$$

where S_0 is the signal without diffusion encoding. The diffusion-weighted signal for a given medium and experimental condition can be obtained by deriving the phase cumulants in Eq. 6.7 up to an order of appropriate approximation.

6.3 Diffusion encoding in a single Gaussian environment

To derive the cumulants of the phase distribution $c_n\big(P(\phi)\big)$ (Eq. 6.6), we recognize that a particle's velocity $\mathbf{v}$ at a given timepoint t can be related to the displacement $\mathbf{r}$ within a short time Δt, according to $\mathbf{v}(t) \approx \Big(\mathbf{r}(t + \frac{\Delta t}{2}) - \mathbf{r}(t - \frac{\Delta t}{2})\Big)/\Delta t$. By the Gaussianity of $P(\mathbf{r}|\Delta t)$, $\tau_c \ll \Delta t$ such that $\mathbf{v}(t)$ is the sum of many independent velocities and $P(\mathbf{v})$ is Gaussian by the central limit theorem (Van Kampen 1992). Accordingly, c_n^v is non-zero only for $n = 2$ and equal time points: $c_2^v(\mathbf{v}^{\otimes 2})$ (Stepišnik 1993). Then, from Eq. 6.6, only $c_2(P(\phi))$ is non-zero wherefore $P(\phi)$ is also Gaussian. The second velocity cumulant is given by

$$\begin{aligned} c_2^v &= \langle \mathbf{v}^{\otimes 2} \rangle - \langle \mathbf{v} \rangle^{\otimes 2} \\ &= \frac{1}{\Delta t^2} (\langle \mathbf{r}^{\otimes 2} \rangle - \langle \mathbf{r} \rangle^{\otimes 2}) = \frac{1}{\Delta t} 2\mathbf{D}. \end{aligned} \tag{6.8}$$

using Eqs. 4.11 and 5.3. Letting $\Delta t \to 0$ yields the second phase cumulant from Eq. 6.6, according to

$$
\begin{aligned}
c_2(P(\phi)) &= \int_0^{\mathrm{TE}} (\mathbf{q}_1 \otimes \mathbf{q}_2) \colon \big(2\mathbf{D}\delta(t_2 - t_1)\big) dt_1 dt_2 \\
&= \left(\int_0^{\mathrm{TE}} \mathbf{q}(t)^{\otimes 2} dt \right) : (2\mathbf{D}) = 2\mathbf{B} \colon \mathbf{D},
\end{aligned}
\tag{6.9}
$$

using the definition of the b-tensor (Eq. 6.1). The diffusion-weighed signal for a single Gaussian environment is thus given by

$$
S = S_0 \exp(-\mathbf{B} \colon \mathbf{D}). \tag{6.10}
$$

For axisymmetric tensors $\mathbf{B}$ and $\mathbf{D}$ with the respective symmetry axes $\mathbf{u}$ and $\mathbf{n}$, Eq. 6.10 is simplified to

$$
S = S_0 \exp(-bD_{\mathrm{I}}[1 + 2b_{\Delta} D_{\Delta} L_2(\beta)]), \tag{6.11}
$$

where $\beta = \mathbf{u} \cdot \mathbf{n}$, and $L_2(\beta) = (3\beta^2 - 1)/2$ is the second Legendre polynomial (Eriksson et al. 2015). Note that, for isotropic diffusion tensors ($D_{\Delta} = 0$) or encoding tensors ($b_{\Delta} = 0$), the diffusion-weighted signal is invariant to anisotropy, according to

$$
S = S_0 \exp(-bD_{\mathrm{I}}). \tag{6.12}
$$

6.4 Diffusion encoding in an ensemble of non-exchanging Gaussian environments

To derive the cumulants of the phase distribution $c_n(P(\phi))$ for an ensemble of non-exchanging Gaussian environments, we recognize that the diffusion-weighted signal is the ensemble-average (Eq. 4.9) of the signals from each environment, according to

$$
S = S_0 \int P(\mathbf{D}) \exp(-\mathbf{B} \colon \mathbf{D}) \, \mathrm{d}\mathbf{D}, \tag{6.13}
$$

where $P(\mathbf{D})$ is the DTD, and that the phase distribution is the ensemble-average of the phase distributions from each environment $P(\phi'|\mathbf{D})$, according to

$$
P(\phi) = \int P(\mathbf{D}) P(\phi'|\mathbf{D}) \mathrm{d}\mathbf{D}. \tag{6.14}
$$

Then, by linearity, the central moments of the phase distribution $m_n\big(P(\phi)\big)$ (Eq. 4.10) are given by

$$\begin{aligned} m_n &= \int (\phi - \langle\phi\rangle)^{\otimes n} P(\phi)\, d\phi \\ &= \int (\phi - \langle\phi\rangle)^{\otimes n} \left(\int P(\mathbf{D}) P(\phi'|\mathbf{D}) \mathrm{d}\mathbf{D} \right) d\phi \\ &= \int P(\mathbf{D}) \left(\int (\phi' - \langle\phi'\rangle)^{\otimes n} P(\phi'|\mathbf{D}) d\phi' \right) \mathrm{d}\mathbf{D} \\ &= \int P(\mathbf{D}) m'_n(\mathbf{D})\, \mathrm{d}\mathbf{D} = \langle m'_n \rangle. \end{aligned} \tag{6.15}$$

The second phase cumulant is then given by Eqs. 4.12, 5.6, 6.9 and 6.15, according to

$$c_2 = 2\mathbf{B}\colon \langle \mathbf{D} \rangle, \tag{6.16}$$

where $\langle \mathbf{D} \rangle$ is the ensemble-average diffusion tensor. The fourth cumulant of $P(\phi)$ is given by Eqs. 4.11, 4.12, 6.9 according to[1]

$$c_4 = 12\mathbf{B}^{\otimes 2}\colon \mathbb{C} \tag{6.17}$$

using $c'_4 = 0$ for the individual environments (Section 6.3). Thus, for an ensemble of non-exchanging Gaussian environments, a fourth-order approximation of the diffusion-weighted signal in terms of phase cumulants (Eq. 6.7) is given by

$$S(\mathbf{B}) \approx S_0 \exp\left(-\mathbf{B}\colon \langle \mathbf{D} \rangle + \frac{1}{2} \mathbf{B}^{\otimes 2}\colon \mathbb{C} \right). \tag{6.18}$$

The equation is also referred to as the covariance tensor model (Westin et al. 2016) and was used for joint analysis of LTE and STE data in Paper V. An expression up to the sixth order that includes the diffusion skew tensor has been presented in Ning et al. (2021).

[1] The full derivation is: $c_4 = \langle m'_4 \rangle - 3\langle m'_2 \rangle^2 = \langle c'_4 + 3{c'_2}^2 \rangle - 3\langle c'_2 \rangle^2 = \langle c'_4 \rangle + 3\big(\langle {c'_2}^2 \rangle - \langle c'_2 \rangle^2 \big)$ $= 3\mathrm{V}[c'_2] = 12\mathbf{B}^{\otimes 2}\colon \mathrm{V}[\mathbf{D}] = 12(\mathbf{B}^{\otimes 2})\colon \mathbb{C}$.

6.4.1 Diffusion-relaxation encoding

The MRI signal is also influenced by non-diffusion phenomena. T_2 relaxation has a large impact on the signal of the spin-echo sequences used in dMRI. For a single environment with T_2 relaxation properties described by the time constant T_2, the signal without diffusion encoding at TE is given by

$$S_0(\mathrm{TE}) = S_0(0)\exp(-\mathrm{TE}/T_2). \tag{6.19}$$

In an ensemble of non-exchanging Gaussian environments with different T_2, Eq. 6.13 generalizes to

$$S = S_0|_{\mathrm{TE}=0} \int P(\mathbf{D}, R_2)\exp(-\mathrm{TE}\cdot R_2)\exp(-\mathbf{B}\colon\mathbf{D})\mathrm{d}\mathbf{D}dR_2 \tag{6.20}$$

where the diffusion-relaxation distribution $P(\mathbf{D}, R_2)$ is a probability distribution over the space of diffusion tensors $\mathbf{D}$ and relaxation rates $R_2 = 1/T_2$.

A cumulant expansion of Eq. 6.20 for a given b-tensor symmetry axis $\mathbf{u}$ using LTE ($\mathbf{B} = b\mathbf{u}^{\otimes 2}$) was presented by Ning et al. (2019). Here, we present a new formulation by extending that expression to any $\mathbf{B}$, according to

$$\begin{aligned} S(\mathbf{B}) \approx S_0\exp\,(& \\ & -\mathbf{B}\colon\langle\mathbf{D}\rangle + \frac{1}{2}\mathbf{B}^{\otimes 2}\colon\mathbb{C} \\ & -\mathrm{TE}\cdot\langle R_2\rangle + \frac{1}{2}\mathrm{TE}^2\cdot\mathrm{Var}[R_2] \\ & +\mathrm{TE}\cdot\mathbf{B}\colon\mathbf{M}_{11} - \frac{1}{2}\mathrm{TE}^2\cdot\mathbf{B}\colon\mathbf{M}_{12} - \frac{1}{2}\mathrm{TE}\cdot\mathbf{B}^{\otimes 2}\colon\mathbb{M}_{21}) \end{aligned} \tag{6.21}$$

where the tensors m_{nm} are the $(n,m)^{\mathrm{th}}$ central moments of $P(\mathbf{D}, R_2)$, $\mathrm{m}_{nm} = \langle(\mathbf{D} - \langle\mathbf{D}\rangle)^{\otimes n}(R_2 - \langle R_2\rangle)^m\rangle$, here given by

$$\begin{aligned} &\mathbf{M}_{11} = \mathrm{cov}(\mathbf{D}, R_2), \\ &\mathbf{M}_{12} = \mathrm{cov}(\mathbf{D}, R_2^2 - 2\langle R_2\rangle R_2) \text{ and} \\ &\mathbb{M}_{21} = \mathrm{cov}(\mathbf{D}^{\otimes 2} - 2\langle\mathbf{D}\rangle\otimes\mathbf{D}, R_2), \end{aligned} \tag{6.22}$$

where the second term in $\mathbb{M}_{21}$ assumes $\langle\mathbf{D}\rangle\otimes\langle R_2\mathbf{D}\rangle = \langle R_2\mathbf{D}\rangle\otimes\langle\mathbf{D}\rangle$. For simplicity, Eq. 6.21 includes the mean and variance terms $\langle\mathbf{D}\rangle, \mathbb{C}, \langle R_2\rangle$ and $\mathrm{Var}[R_2]$ of the marginal distributions $P(\mathbf{D}, R_2|\mathrm{TE} = 0)$ and $P(\mathbf{D}, R_2|b = 0)$, but excludes the higher order terms.

6.5 Powder-averaged signal expressions

So-called powder averaging corresponds to arithmetic averaging of the signal across different b-tensor symmetry axes ($\mathbf{u}$) to mimic a complete orientation dispersion of the diffusion tensors across the DTD. In the limit of a fully homogeneous directional average, the signal depends only on the scalar rotational invariants of the tensors that describe diffusion and diffusion encoding (Callaghan et al. 1979). This section derives powder-averaged versions of the signal expressions in Sections 6.3 and 6.4.

6.5.1 A single Gaussian environment

For a single Gaussian environment, assuming axisymmetric diffusion and encoding tensors, the powder-averaged version of Eq. 6.11 is given by

$$\begin{aligned}\bar{S} &= S_0 \int_{\mathbf{u}\in\mathbb{S}^2} (-bD_{\mathrm{I}}[1 + 2b_\Delta D_\Delta L_2(\mathbf{u}\cdot\mathbf{n})])\mathrm{d}\mathbf{u} \\ &= S_0 \exp(-bD_{\mathrm{I}} + \alpha/3) \int_{\mathbf{u}\in\mathbb{S}^2} \exp(-\alpha(\mathbf{u}\cdot\mathbf{n})^2)\mathrm{d}\mathbf{u} \\ &= S_0 \exp(-bD_{\mathrm{I}} + \alpha/3) \sqrt{\frac{\pi}{4\alpha}}\mathrm{erf}(\sqrt{\alpha}),\end{aligned} \tag{6.23}$$

which uses the substitution $\mathbf{u}\cdot\mathbf{n} = x$, and where

$$\alpha = 3bD_{\mathrm{I}}b_\Delta D_\Delta \tag{6.24}$$

and erf is the error function. Eq. 6.23 was initially presented for $b_\Delta = 1$ in Callaghan et al. (1979) and extended to any b_Δ in Eriksson et al. (2015). It was used to derive the powder-averaged version of the NODDI model (Zhang et al. 2012) in Paper II and of multiple models in Paper III.

6.5.2 An ensemble of non-exchanging Gaussian environments

The powder-averaged signal for an ensemble of non-exchanging Gaussian environments can be expanded in isotropic cumulants of the phase distribution $c_{n;\mathrm{I}}(P(\phi))$, obtained by replacing the tensors in Eq. 6.18 with their isotropic projections. For a tensor $\mathbf{t}$, the projection onto an isotropic basis $\mathbf{e}_{\mathrm{I}}$ is given by $\mathbf{t}_{\mathrm{I}} = (\mathbf{t}\colon\mathbf{e}_{\mathrm{I}}/\mathbf{e}_{\mathrm{I}}\colon\mathbf{e}_{\mathrm{I}})\mathbf{e}_{\mathrm{I}}$. For second-order

tensors and the isotropic basis $\mathbf{E}_{\mathrm{I}} = \frac{1}{3}\mathbf{I}$, where $\mathbf{E}_{\mathrm{I}} \colon \mathbf{E}_{\mathrm{I}} = \frac{1}{3}$, the isotropic projections are given by $\mathbf{T}_{\mathrm{I}} = 3\mathrm{E}_{\lambda}[\mathbf{T}]\mathbf{E}_{\mathrm{I}}$. For $\mathbf{B}$ and $\langle \mathbf{D} \rangle$, we obtain

$$\begin{aligned} \mathbf{B}_{\mathrm{I}} &= b\mathbf{E}_{\mathrm{I}}, \\ \langle \mathbf{D} \rangle_{\mathrm{I}} &= 3\mathrm{MD}\mathbf{E}_{\mathrm{I}} \text{ and} \\ c_{2;\mathrm{I}} &= 2b\mathrm{MD}. \end{aligned} \tag{6.25}$$

For fourth-order tensors and the isotropic basis $\mathbb{E}_{\mathrm{I}} = \mathbb{E}_{\mathrm{bulk}} + \mathbb{E}_{\mathrm{shear}}$, where $\mathbb{E}_{\mathrm{bulk}} \colon \mathbb{E}_{\mathrm{bulk}} = \frac{1}{9}$, $\mathbb{E}_{\mathrm{shear}} \colon \mathbb{E}_{\mathrm{shear}} = \frac{5}{9}$ and $\mathbb{E}_{\mathrm{bulk}} \colon \mathbb{E}_{\mathrm{shear}} = 0$, the isotropic projections are given by $\mathbb{T}_{\mathrm{I}} = (9\mathbb{T} \colon \mathbb{E}_{\mathrm{bulk}})\mathbb{E}_{\mathrm{bulk}} + (9/5\,\mathbb{T} \colon \mathbb{E}_{\mathrm{shear}})\mathbb{E}_{\mathrm{shear}}$. For $\mathbf{B}^{\otimes 2}$ and $\mathbb{C}$, we obtain

$$\begin{aligned} (\mathbf{B}^{\otimes 2})_{\mathrm{I}} &= b^2 \left(\mathbb{E}_{\mathrm{bulk}} + \frac{2}{5} b_{\Delta}^2 \mathbb{E}_{\mathrm{shear}} \right), \\ \mathbb{C}_{\mathrm{I}} &= 9 \left(V_{\mathrm{I}} \mathbb{E}_{\mathrm{bulk}} + \frac{1}{2} V_{\mu\mathrm{A}} \mathbb{E}_{\mathrm{shear}} \right) \text{ and} \\ c_{4;\mathrm{I}} &= 12b^2 (V_{\mathrm{I}} + b_{\Delta}^2 V_{\mu\mathrm{A}}), \end{aligned} \tag{6.26}$$

using Eqs. 5.8 and 5.9 and that $V_{\mathrm{MA}} = 0$ in the powder average. The variances can be scaled to the dimensionless isotropic kurtosis ($\mathrm{MK_I}$) and anisotropic kurtosis ($\mathrm{MK_A}$), according to (Szczepankiewicz et al. 2016a)

$$\begin{aligned} \mathrm{MK_I} &= 3 \frac{V_{\mathrm{I}}}{\mathrm{MD}^2}, \\ \mathrm{MK_A} &= 3 \frac{V_{\mu\mathrm{A}}}{\mathrm{MD}^2}, \text{and} \\ \mathrm{MK_E} &= \mathrm{MK_I} + b_{\Delta}^2 \mathrm{MK_A}, \end{aligned} \tag{6.27}$$

where the 'effective kurtosis' $\mathrm{MK_E}$ depends on the shape of the b-tensor. Notably, the $\mathrm{MK_E}$ resulting from LTE ($b_{\Delta} = 1$) is referred to as the 'total kurtosis,' $\mathrm{MK_T} = \mathrm{MK_I} + \mathrm{MK_A}$ (Lasič et al. 2014, Szczepankiewicz et al. 2016a). The powder-averaged version of Eq. 6.18 is then given by

$$\bar{S} \approx S_0 \exp\left(-b \cdot \mathrm{MD} + \frac{1}{6} b^2 \cdot (\mathrm{MK_I} + b_{\Delta}^2 \cdot \mathrm{MK_A}) \mathrm{MD}^2 \right). \tag{6.28}$$

The equation is also referred to as the powder-averaged covariance tensor model and was used for joint analysis of LTE and STE data in Paper III. For LTE, Eq. 6.28 yields the powder-averaged diffusion kurtosis model (Jensen et al. 2005).

6.5.3 An ensemble of non-exchanging Gaussian environments with T_2 relaxation

To derive the powder-averaged signal in an ensemble of non-exchanging Gaussian environments with T_2 relaxation, we use the approach in Section 6.5.2 and replace the tensors in Eq. 6.21 with isotropic projections. For $\mathbf{D}$ and $\mathbf{D}^{\otimes 2}$, we obtain

$$\begin{aligned} \mathbf{D}_\mathrm{I} &= 3D_\mathrm{I}\mathbf{E}_\mathrm{I}, \\ (\mathbf{D}^{\otimes 2})_\mathrm{I} &= 9D_\mathrm{I}^2\mathbb{E}_\mathrm{bulk} + \frac{9}{5}\mathrm{V}_\lambda[\mathbf{D}]\mathbb{E}_\mathrm{shear}. \end{aligned} \tag{6.29}$$

Then, using Eqs. 6.25 and 6.26, we obtain the powder-averaged version of Eq. 6.21, according to

$$\begin{aligned} \log\left(\frac{\bar{S}}{S_0}\right) \approx & \\ & -b\cdot\mathrm{MD} + \frac{1}{6}b^2\cdot(\mathrm{MK_I} + b_\Delta^2\cdot\mathrm{MK_A})\mathrm{MD}^2 \\ & -\mathrm{TE}\cdot\langle R_2\rangle + \frac{1}{2}\mathrm{TE}^2\cdot\mathrm{Var}[R_2] \\ & +\mathrm{TE}b\cdot\mathrm{cov}(D_\mathrm{I}, R_2) \\ & -\frac{1}{2}\mathrm{TE}^2 b\cdot\mathrm{cov}(D_\mathrm{I}, R_2^2 - 2\langle R_2\rangle\cdot R_2) \\ & -\frac{1}{2}\mathrm{TE}b^2\cdot\mathrm{cov}(D_\mathrm{I}^2 + \frac{9}{5}b_\Delta^2\cdot\mathrm{V}_\lambda[\mathbf{D}], R_2). \end{aligned} \tag{6.30}$$

Similar to how the b-tensor shape (b_Δ) determines the effective kurtosis ($\mathrm{MK_E}$, Eq. 6.27), the b-tensor shape determines the 'effective eigenvalue variance' of the diffusion tensors (Eriksson et al. 2015, Szczepankiewicz et al. 2021), here derived as

$$\mathrm{V}_{\lambda,\mathrm{E}}[\mathbf{D}] = D_\mathrm{I}^2 + \frac{9}{5}b_\Delta^2\cdot\mathrm{V}_\lambda[\mathbf{D}], \tag{6.31}$$

where LTE ($b_\Delta = 1$) yields the 'total eigenvalue variance' $\mathrm{V}_{\lambda,\mathrm{T}}$.

7 Estimating brain tissue quantities with microstructure modeling

This chapter describes the use of model fitting to extract the information that has been encoded into the dMRI signal, and how using a forward microstructure model allows the information to be interpreted in terms of brain tissue quantities.

7.1 Model fitting for extracting tissue information

The acquired dMRI signal reflects the tissue in the voxel but also experimental parameters such as $\mathbf{B}$ and $\mathbf{TE}$ as well as noise and measurement artifacts. To estimate quantities that reflect the tissue independently on the details of the experiment, the signal is expressed a priori using a forward model that separates the influence of model parameters and experimental parameters. The model parameters are then estimated from an acquired signal by solving the inverse problem of finding the set of parameters that best explains the signal given the experiment. Measurement noise and artifacts are typically not included in the forward model and will generally reduce model parameter precision and trueness, respectively.

7.2 Microstructure models are constrained DTDs

Two main types of forward models are used for dMRI data: signal representations and microstructure models (Novikov et al. 2018a). Signal representations include the truncated cumulant expansions in Eqs. 6.18, 6.21, 6.28 and 6.30. These models parameterize the encoded tissue information in terms of statistical properties of the DTD. For example, the powder-averaged covariance tensor model (Eq. 6.28) is parameterized by the MD, $\mathrm{MK_I}$ and $\mathrm{MK_A}$. Microstructure models are DTDs constrained down to a few 'components' that represent tissue microstructure (Nilsson et al. 2013b, Novikov et al. 2018a, Alexander et al. 2019, Jelescu et al. 2020). These models parameterize the encoded tissue information in

terms of tissue quantities. For example, the NODDI model is parameterized by the 'neurite density' and the 'free water density' (Zhang et al. 2012).

7.2.1 Separation between ODF and kernel

The DTDs of microstructure models are constrained by three fundamental assumptions. First, the diffusion tensors are assumed to be axisymmetric (Figure 4.1). Second, tensors are assumed to feature a finite number (J) of different size/shape combinations ($D_{\mathrm{I};j}, D_{\Delta;j}$), which are referred to as 'components.' Third, symmetry axes $\{\mathbf{n}\}_j$ are assumed to follow the same orientation distribution function (ODF) $P(\mathbf{n})$ for tensors of all component combinations. Then, for axisymmetric b-tensors, Eq. 6.13 can be simplified to the isotropic convolution ($\circledast$) on the unit sphere (Driscoll et al. 1994) between a rotationally invariant kernel K and $P(\mathbf{n})$ using Eq. 6.11, according to

$$\begin{aligned} S &= S_0(K \circledast P(\mathbf{n}))(\mathbf{u}) \\ &= S_0 \int_{|\mathbf{n}|=1} K(\mathbf{u}\cdot\mathbf{n})\, P(\mathbf{n})\mathrm{d}\mathbf{n}, \text{where} \\ K(\mathbf{u}\cdot\mathbf{n}) &= \sum\nolimits_{j=1}^{\mathrm{J}} f_j \exp(-bD_{\mathrm{I}}[1 + 2b_{\Delta}D_{\Delta}L_2(\mathbf{u}\cdot\mathbf{n})]) \end{aligned} \tag{7.1}$$

and f_j ($\sum f_j = 1, f_j \geq 0$) is the signal fraction without diffusion encoding of the j^{th} component. The kernel captures the rotationally invariant (microstructural) aspects of the DTD—the signal fractions and the tensor isotropic invariants ($D_{\mathrm{I};j}$ and $D_{\Delta;j}$)—while the ODF captures the orientational variation of that configuration.

7.2.2 ODF expansion in spherical harmonics

Some microstructure models assume an ODF on a closed form to yield a minimal but realistic representation of the arrangement of anisotropic structures within tissue. Such ODFs include the axisymmetric three-parameter Watson distribution (Mardia et al. 2009, Zhang et al. 2012) and the biaxial five-parameter Bingham distribution (Bingham 1974, Tariq et al. 2016). Other models use a truncated spherical harmonic (SH) expansion of the ODF (Jespersen et al. 2007, Jespersen et al. 2010). This approach, which was used in Paper IV, has the advantage of being more general and removing the integral from Eq. 7.1.

In the SH basis, the kernel coefficients (k_{lm}) are rotationally invariant and factor with the ODF coefficients (p_{lm}), according to

$$(K \circledast P)(\mathbf{u}) = \sum_{l,m} S_{lm}(\mathbf{u}) = \sum_{l,m} k_{l0} p_{lm} Y_{lm}(\mathbf{u}) \sqrt{\frac{4\pi}{2l+1}}, \tag{7.2}$$

where the sum is over the SH basis functions Y_{lm} of order $l = 0, 2, ...$ and degree $m = -l, -l+1, ..., l$. Due to the axial symmetry of K, its coefficients are non-zero only for even l (odd-order harmonics are anti-symmetric) and $m = 0$ (invariance to symmetry-axis rotation). The kernel coefficients are obtained from inner products with SH basis functions of the appropriate order and have been derived for LTE, for example, in Jespersen et al. (2007). In Paper IV, we derived the kernel coefficients for any shape of the b-tensor, according to

$$\begin{aligned} k_{l0} &= \sqrt{4\pi(2l+1)} \sum\nolimits_{j=1}^{J} f_j \exp\left(-bD_{\mathrm{I};j} + \frac{\alpha_j}{3}\right) I_{lj}, \text{where} \\ \mathrm{I}_{lj} &= \int_0^1 e^{-\alpha_j \mathrm{x}^2} L_l(x) dx, \end{aligned} \tag{7.3}$$

where L_l is the l^{th} Legendre polynomial and α_j is from Eq. 6.24. Note that the zeroth-order coefficient features the powder-averaged diffusion attenuations for each component (Eq. 6.23).

7.2.3 Kernel component selection

The kernel components of microstructure models are selected to capture the diffusion characteristics of water within different microstructural components of brain tissue (Alexander et al. 2019). Figure 7.1A illustrates the three main components used by contemporary models to represent tissue microstructure in white matter.

- The 'stick' component (S) with zero radial diffusivity ($D_{\Delta;\mathrm{S}} = 1$) represents the intra-axonal space (Behrens et al. 2003), whose elongated shape induces a maximally anisotropic diffusion (McKinnon et al. 2017, Veraart et al. 2019).
- The 'zeppelin' component (Z) with non-zero radial diffusivity ($D_{\Delta;\mathrm{Z}} < 1$) represents the extra-axonal space (or extra-axonal tissue in fast exchange) with less anisotropic diffusion.
- The 'ball' component (B) with isotropic diffusion ($D_{\Delta;\mathrm{B}} = 0$) and fixed isotropic diffusivity $D_{\mathrm{I};\mathrm{B}} = 3\ \mu\mathrm{m}^2/\mathrm{ms}$ represents CSF (Pasternak et al. 2009).

Note that no component represents myelin. Despite a relatively large volume fraction in white matter (Figure 3.1B, Section 3.2), the low T_2 values of myelin water and myelin lipid result in a very small signal fraction at the TE used in dMRI (Mackay et al. 1994).

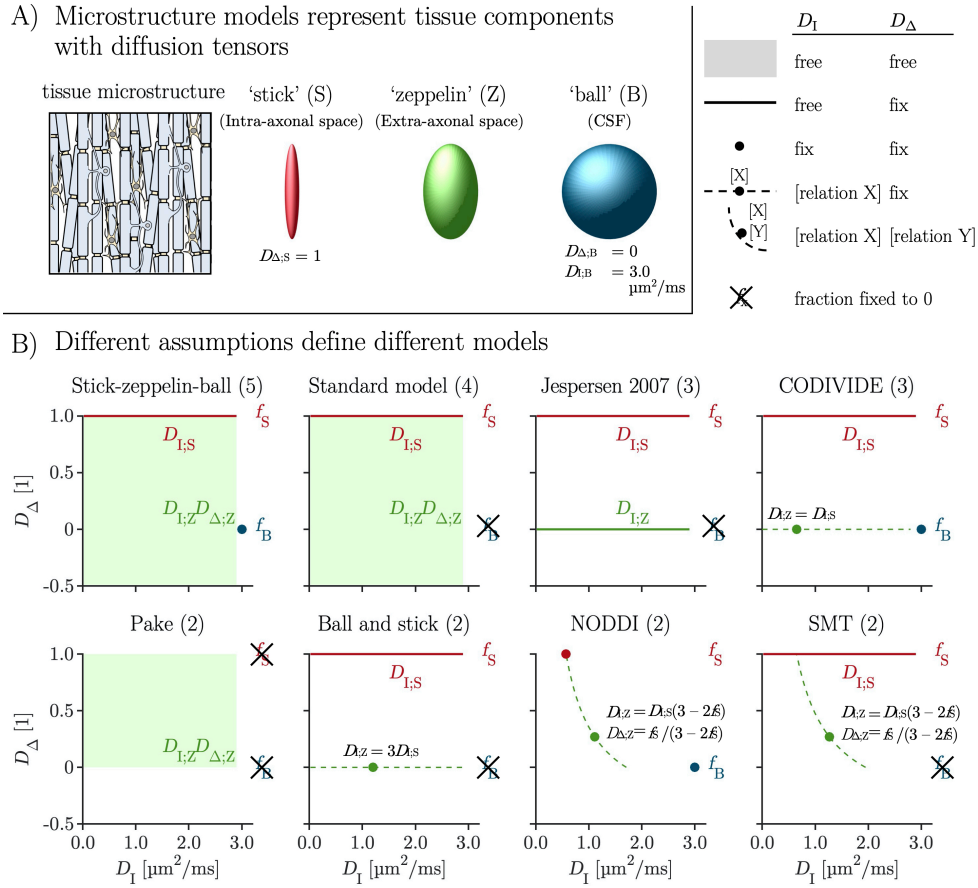

Figure 7.1 | A) Microstructure models represent tissue components with diffusion tensors with different characteristics. 'Sticks' and 'zeppelins' represent the intra- and extra-axonal space and 'balls' represent CSF. B) Assumptions that fix or enforce relations between the parameters of the Stick-Zeppelin-Ball model result in different microstructure models with different number of free parameters (in parenthesis, Table 7.1). The DTD that corresponds to each model is illustrated by representing each component (coded by color) with its allowed position in the tensor size/shape landscape (Figure 4.1). Free parameters are written out explicitly (coded by color). Areas denote unconstrained components, lines denote components with fixed shapes, dots denote components that are fully constrained by fixing and/or relations. Crossed fractions indicate fixing its value to zero.

7.3 Different assumptions define different models

The full 'Stick-Zeppelin-Ball' model features five kernel parameters (Table 7.1, excluding S_0): the 'stick' fraction (f_{S}), the 'stick' isotropic diffusivity ($D_{\mathrm{I;S}}$), the 'zeppelin' isotropic diffusivity ($D_{\mathrm{I;Z}}$), the 'zeppelin' anisotropy ($D_{\Delta;\mathrm{Z}}$), and the 'ball' fraction (f_{B}). Fitting all five parameters results in a degenerate inverse problem for most dMRI acquisitions (Jelescu et al. 2016a). Therefore, microstructure models use assumptions that reduce the number of free kernel parameters.

Different assumptions on the Stick-Zeppelin-Ball model define different microstructure models from the literature (Table 7.1, Figure 7.1B). Assumptions take the form of constraints that reduce the number of free parameters by fixing a parameter's value or by enforcing a relation between two parameters. The four-parameter 'Standard model' assumes no CSF ($f_{\mathrm{B}} = 0$). The three-parameter 'Jespersen 2007' model additionally assumes isotropic diffusion in the 'zeppelin' component ($D_{\Delta;\mathrm{Z}} = 0$). CODIVIDE equals Jespersen 2007 but assumes equal 'stick' and 'zeppelin' isotropic diffusivities ($D_{\mathrm{I;Z}} = D_{\mathrm{I;S}}$) instead of no CSF. Among the two-parameter models, 'Pake' only includes the 'zeppelin' component. 'Ball and stick' equals Jespersen 2007 but assumes equal 'stick' and 'zeppelin' axial diffusivities ($D_{\mathrm{I;Z}} = 3D_{\mathrm{I;S}}$). The NODDI and SMT models fully constrain the 'zeppelin' component. Its shape is defined by a tortuosity relation (Szafer et al. 1995), according to

$$D_{\Delta;\mathrm{Z}} = f_{\mathrm{S}}/(3 - 2f_{\mathrm{S}}), \tag{7.4}$$

and its size is determined by assuming equal 'stick' and 'zeppelin' axial diffusivities, according to (using Eq. 7.4)

$$D_{\mathrm{I;Z}} = D_{\mathrm{I;S}}(3 - 2f_{\mathrm{S}}). \tag{7.5}$$

NODDI and SMT differ in their third assumption, where NODDI uses $D_{\mathrm{I;S}} = 0.57\ \mu\mathrm{m}^2/\mathrm{ms}$ and SMT uses $f_{\mathrm{B}} = 0$.

Table 7.1 | Different sets of assumptions on the Stick-Zeppelin-Ball model results in different microstructure models from the literature. Extending the Stick-Zeppelin-Ball model to include free 'stick' and 'zeppelin' T_2 values results in the diffusion-relaxation models used in Papers III and IV.

Diffusion models	Model constraints (- indicates a free parameter)					# free
	f_{S}	$D_{\mathrm{I;S}}$	$D_{\mathrm{I;Z}}$	$D_{\Delta;\mathrm{Z}}$	f_{B}	pars.
Stick-Zeppelin-Ball	-	-	-	-	-	5
Standard model[a]	-	-	-	-	0	4
Jespersen 2007[b]	-	-	-	0	0	3
CODIVIDE[c]	-	-	$D_{\mathrm{I;S}}$	0	-	3
Pake[d]	0	N/A	-	-	0	2
Ball and stick[e]	-	-	$3D_{\mathrm{I;S}}$	0	0	2
NODDI[f]	-	0.57	Eq. 7.5	Eq. 7.4	-	2
SMT[g]	-	-	Eq. 7.5	Eq. 7.4	0	2
Diffusion-relaxation models						
PIV+[h]	-	-	-	-	-	7
PIV[i]	-	-	-	-	0	6
PIII[j]	-	-	-	0	0	5

Diffusivities are in $\mu\mathrm{m}^2/\mathrm{ms}$.

The number of free parameters counts the kernel parameters but excludes S_0.

Diffusion-relaxation models include $T_{2;\mathrm{S}}$ and $T_{2;\mathrm{Z}}$ as free parameters.

[a](Novikov et al. 2018b), [b](Jespersen et al. 2007) (with $D_{\Delta;\mathrm{S}} = 1$), [c]Paper II, [d](Kroenke et al. 2004, Eriksson et al. 2015, Kaden et al. 2015), [e](Behrens et al. 2003), [f](Zhang et al. 2012), [g](Kaden et al. 2016), [h]Paper IV (Supporting information), [i]Paper IV, [j]Paper III

7.4 The role of T_2 relaxation

Heterogeneity in T_2 values across microscopic environments impacts the relationship between the environments' signal fractions and volume fractions. In an ensemble of non-exchanging environments with different T_2 values, the signal fraction at TE (without diffusion encoding) for an environment with volume fraction v_j and T_2 value $T_{2;j}$ is given by

$$f_j(\mathrm{TE}) = \frac{S_{0;j}(\mathrm{TE})}{S_0(\mathrm{TE})} = \frac{v_j \exp(-\mathrm{TE}/T_{2;j})}{\int P(\mathbf{D}, R_2|b=0)\exp(-\mathrm{TE}\cdot R_2)\,\mathrm{d}\mathbf{D}dR_2} \tag{7.6}$$

where $P(\mathbf{D}, R_2)$ is the diffusion-relaxation distribution of the ensemble. Thus, signal fractions are generally TE-dependent and different from volume fractions.

7.4.1 The density assumption

When signal fractions are interpreted as volume fractions (densities), an implicit 'density assumption' is made that the T_2 values are approximately equal across environments, according to

$$T_{2j} \approx T_{2j'} \;\forall\; j, j', \tag{7.7}$$

which allows the T_2-dependency in Eq. 6.20 to be factored into the S_0 parameter.

7.4.2 Diffusion-relaxation models

Extending microstructure models to include T_2-relaxation is straightforward. By using the diffusion-relaxation distribution $P(\mathbf{D}, R_2)$ and Eq. 6.20 instead of $P(\mathbf{D})$ and Eq. 6.13, the kernel is modified as

$$K(\mathbf{u}\cdot\mathbf{n}, \mathrm{TE}) = \textstyle\sum_{j=1}^{\mathrm{J}} f_j\, A_{\mathrm{D};j}(\mathbf{u}\cdot\mathbf{n})\exp(-\mathrm{TE}/T_{2;j}), \tag{7.8}$$

using $A_{\mathrm{D};j}$ from Eq. 6.11. Example diffusion-relaxation models are shown in Table 7.1, and include the models used in Paper III (PIII) and Paper IV (PIV), as well as the model in the supporting information of Paper IV (PIV+). In PIV+, the 'ball' T_2 value was fixed as $T_{2;\mathrm{B}} = 1.4$ s to represent free water (Weigel et al. 2006).

8 Removing model assumptions with multidimensional dMRI

This chapter investigates to what degree multidimensional dMRI data alleviate the need for model assumptions on diffusion and T_2 relaxation. First, we formalize the relationship between the acquisition and the tissue information that it encodes into the signal. We define the concept of an acquisition protocol and how different protocols use different encoding dimensions that are sensitive to different tissue observables. Then, we use a test for degeneracy to investigate the relationship between acquisition protocols and the ability of the resulting data to support different microstructure models. Finally, we optimize a multidimensional acquisition protocol to remove most assumptions on diffusion and T_2 relaxation in vivo.

8.1 Acquisition protocols, encoding dimensions, and tissue observables

This section analyses the information content of a general diffusion-relaxation acquisition from the perspective of the powder-averaged cumulant expansion (Eq. 6.30). Notably, powder-averaging removes the information provided by the signal differences across b-tensors symmetry axes ($\mathbf{u}$). On the one hand, this has a small but non-negligible negative impact also on the precision of non-orientational model parameters, as investigated in Paper IV. On the other hand, powder-averaging simplifies the signal descriptors to scalar rotationally invariants and focuses the analysis to the information that is present independently of the true orientation dispersion in an image voxel.

We define an 'acquisition protocol' as a set of encoding parameters b_n, $b_{\Delta;n}$, TE_n, and $\mathbf{u}_n$ that specify the acquisition of a full dataset intended for model fitting. For b-values, we define the 'low interval' as $b \leq 1\ \mathrm{ms}/\mu\mathrm{m}^2$ and the 'high interval' as $1 < b \leq 2.5\ \mathrm{ms}/\mu\mathrm{m}^2$.

We define an 'encoding dimension' as a unique product of the scalar encoding parameters b, b_Δ and $\mathbf{TE}$ that form the acquisition-related part of a term in the cumulant expansion (Eq. 6.30).

We define a 'tissue observable' as a product of scalar model parameters (such as $\mathbf{MD}$ or $\mathbf{MK}_\mathrm{A}$) that form the tissue-related parts of a term in the cumulant expansion (Eq. 6.30). Note that, by definition, encoding dimensions and tissue observables are coupled and equal in number. For example, the encoding dimensions b and b^2 have sensitivity to the tissue observables $\mathbf{MD}$ and $\mathbf{MK}_\mathrm{T}$ (Eq. 6.27 with $b_\Delta = 1$), respectively (excluding repeated quantities).

For a given acquisition protocol, we define the associated set of encoding dimensions and tissue observables as those that form the cumulant expansion terms that are necessary and sufficient to describe the signal. This means that fitting the signal representation that includes these terms would be statistically favored by, for example, an F-test over fitting representations with fewer or more terms. Thus, the set of tissue observables captures all rotationally invariant tissue information that is provided by varying the encoding parameters. This also means that extending the acquisition to use additional encoding dimensions may yield sensitivity to additional observables. This is the key benefit of multidimensional dMRI (Topgaard 2017, de Almeida Martins et al. 2018, Benjamini et al. 2020).

The relationship between acquisition protocols and tissue observables clearly depends on the specifics of the tissue as well as the noise level in each situation. As a rule of thumb, the signal contribution from the b^2 and b^3 cumulant expansion terms can be considered small for b-values $b \leq 1\,\mathrm{ms/\mu m^2}$ (Jones et al. 2004) and $b \leq 2.5\,\mathrm{ms/\mu m^2}$ (Kiselev et al. 2007, Ianuş et al. 2018), respectively, corresponding to the low and high intervals defined above. Notably, the contribution from higher-order terms is generally not negligible wherefore the choice of signal representation is a compromise between precision and trueness (Ianuş et al. 2018).

Table 8.1 lists six acquisition protocols together with the encoding dimensions that they use and the tissue observables they are sensitive to (rephrased to only feature independent quantities).

- 'SDE_1' features a single shape of the b-tensor (LTE, $b_\Delta = 1$) and b-values in the low interval. This uses encoding dimension b with sensitivity to observable $\mathbf{MD}$.
- 'SDE_2' also features b-values in the high interval. This uses encoding dimension b^2 with sensitivity to observable $\mathbf{MK}_\mathrm{T}$.
- 'QTI' also features two or more b-tensor shapes (b_Δ) for b-values in the high interval. This uses encoding dimension $b^2 b_\Delta^2$ with sensitivity to observable $\mathbf{MK}_\mathrm{E}$.

- 'DR_1' also features multiple TE for b-values in the low interval. This uses encoding dimensions TE, TE^2, $b\mathrm{TE}$ and $\mathrm{TE}^2 b$ with sensitivity to observables $\langle R_2 \rangle$, $\mathrm{V}[R_2]$, $\mathrm{cov}(D_\mathrm{I}, R_2)$ and $\mathrm{cov}(D_\mathrm{I}, R_2^2)$, respectively.
- 'DR_2' also features multiple TE for b-values in the high interval for $b_\Delta = 1$.This uses dimension $b^2\mathrm{TE}$ with sensitivity to observable $\mathrm{cov}(\mathrm{V}_{\lambda,\mathrm{T}}[\mathbf{D}], R_2)$.
- 'DR_3' also features multiple TE in the high interval for different b_Δ. This uses dimension $\mathrm{TE}b^2 b_\Delta^2$ with sensitivity to observable $\mathrm{cov}(\mathrm{V}_{\lambda,\mathrm{E}}[\mathbf{D}], R_2)$.

Table 8.1 | Encoding dimensions and tissue observables associated with acquisition protocols.

Encoding dimension	Tissue observable		Acquisition protocol					
			SDE_1	SDE_2	QTI	DR_1[a]	DR_2[b]	DR_3[c]
b	MD		1	1	1	1	1	1
b^2	$\mathrm{MK_T}$[d]		0	1	1	1	1	1
$b^2 b_\Delta^2$	$\mathrm{MK_E}$[e]		0	0	1	1	1	1
TE	$\langle R_2 \rangle$		0	0	0	1	1	1
TE^2	$\mathrm{V}[R_2]$		0	0	0	1	1	1
$\mathrm{TE}b$	$\mathrm{cov}(D_\mathrm{I}, R_2)$		0	0	0	1	1	1
$\mathrm{TE}^2 b$	$\mathrm{cov}(D_\mathrm{I}, R_2^2)$		0	0	0	1	1	1
$\mathrm{TE}b^2$	$\mathrm{cov}(\mathrm{V}_{\lambda,\mathrm{T}}[\mathbf{D}], R_2)$[f]		0	0	0	0	1	1
$\mathrm{TE}b^2 b_\Delta^2$	$\mathrm{cov}(\mathrm{V}_{\lambda,\mathrm{E}}[\mathbf{D}], R_2)$[g]		0	0	0	0	0	1
		Σ	1	2	3	7	8	9

[a]Paper III (Group C)
[b]Paper IV (in vivo protocol)
[c](de Almeida Martins et al. 2018)
[d]Assuming SDE ($b_\Delta = 1$) (Eq. 6.27)
[e]Separation of $\mathrm{MK_I}$ and $\mathrm{MK_A}$ (Eq. 6.27)
[f]Assuming SDE ($b_\Delta = 1$) (Eq. 6.31)
[g]Separation of D_I^2 and $\mathrm{V}_\lambda[\mathbf{D}]$ (Eq. 6.31)

8.2 Test for degeneracy

In Paper III, we devised a test for degeneracy that assesses whether a given acquisition protocol yields sufficient data to support a given microstructure model. In the test, a signal is first synthesized using the acquisition protocol, the forward microstructure model, and a relevant set of prior values of the free model parameters. Then, after adding noise, the model is repeatedly fitted to the signal with one of its free parameters pre-fixed in the fit to different values along its prior range. A goodness-of-fit metric is calculated, for each fixed value, as the variance of the fit residuals normalized with the variance due to noise, or the 'normalized residual variance' (NRV), according to

$$\mathrm{NRV} = \tfrac{1}{\mathrm{I}} \textstyle\sum_{i=1}^{\mathrm{I}} \big(\sum_{k=1}^{\mathrm{K}} [(S_{ki} - S'_{ki})^2 / (\mathrm{K} - \mathrm{M})] / \sigma^2_{\mathrm{noise}} \big), \tag{8.1}$$

where the average is across I realizations of Gaussian noise with variance $\sigma^2_{\mathrm{noise}}$, S_{ki} is the noised signal, S'_{ki} is the fitted signal, K is the total number of measurements and M is the number of free model parameters after fixing. Plotting the NRV against the values of the fixed parameter illustrates how precisely this parameter is determined by the acquired data. If the protocol yields sufficient data to determine the parameter, then the plot should exhibit a single prominent minimum. If the protocol yields insufficient data, however, multiple parameter values will yield similar goodness-of-fit and the plot will indicates degeneracy by being flat or having multiple minima.

8.3 Acquisition protocol versus model support

In Papers III and IV, we used the test for degeneracy to assess the ability of different diffusion-relaxation acquisition protocols to support microstructure models with free component T_2 values. In Figure 8.1, we extend this analysis to more cases to fully illustrate the relationship between the acquisition protocol and the ability to support different models. The test was applied to twenty-four cases comprised of four different acquisition protocols and six different microstructure models. The protocols (Table 8.1, with its associated number of tissue observables) were: SDE_2 (2), QTI (3), DR_1 (7) and DR_2 (8). The models (Table 7.1, with number of free kernel parameters, excluding S_0) were powder-averaged versions of four diffusion models: Ball and stick (2), Jespersen 2007 (3) and Standard model (4); and three diffusion-relaxation models: PIII (5), PIV (6) and PIV+ (7).

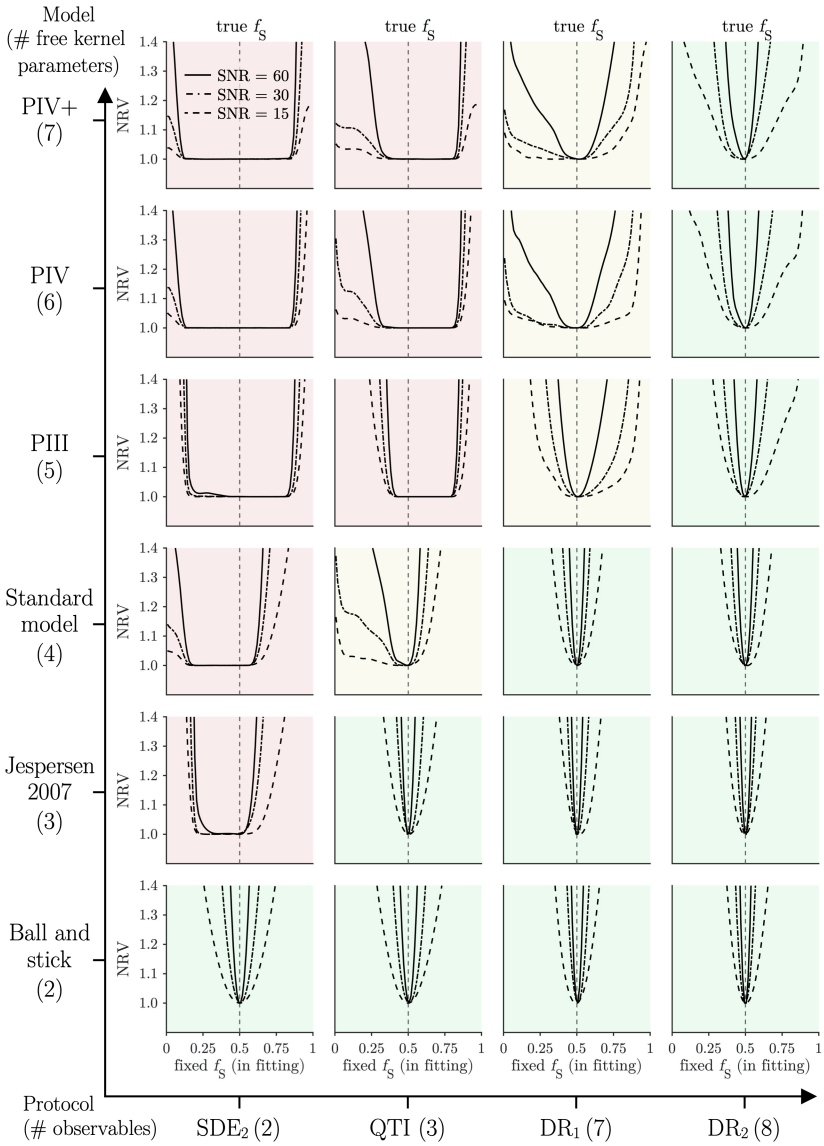

Figure 8.1 | The ability of different acquisition protocols (Table 8.1) to support different models (Table 7.1), illustrated by the normalized residual variance (NRV, Eq. 8.1). Narrow NRV minima indicate that the protocol yielded sufficent data to uniquely determine the 'stick' fraction parameter (f_S). Flat minima indicate insufficient data that are equally well explained by multiple sets of model parameters. The plots are colored based on whether the protocol could support the model at all noise levels (green), some noise-level (yellow) or no noise level (red) Data were synthesized assuming the priors: $S_0 = 1$, $f_S = 0.5$, $D_{I;S} = 0.8 \times 10^{-9} \frac{\mu m^2}{ms}$, $T_{2;S} = 100$ ms, $D_{I;Z} = 0.8 \times 10^{-9}$ $\mu m^2/ms$, $D_{\Delta;Z} = 0.4$, $T_{2;Z} = 60$ ms, and $f_B = 0$. Gaussian noise was added at SNR corresponding to 15, 30 and 60 at $TE = 70$ ms. To correct for protocol differences in acquisition time (T_{Acq}), the actual SNR was adjusted according to $SNR = SNR_{ref}(T_{Acq}/T_{Acq;ref})^{1/2}$, with $T_{Acq;ref} = 30$ min. The NRV (Eq. 8.1) was calculated when pre-fixing the 'stick' fraction (f_S) between zero and unity. Data were powder-averaged before fitting.

In all cases where the protocol yielded sufficient data to support the model at all noise levels (Figure 8.1, green plots), the number of tissue observables associated with the protocol was greater than or equal to the model's number of free kernel parameters. Conversely, in all cases where the protocol yielded insufficient data to support the model at any noise level (red plots), the number of tissue observables associated with the protocol was smaller than the model's number of free kernel parameters. Thus, the number of tissue observables required to describe the acquired data appears to be closely related to the maximal number of free kernel parameters of models that the data can support. However, as shown by the yellow plots in Figure 8.1, the exact data requirements in each situation may depend on the noise level and likely also on tissue priors and orientational information (absent here due to powder-averaging).

The results in Figure 8.1 were consistent with previous results from the literature. Conventional dMRI using SDE with b-values in the high interval (SDE_2, Table 8.1) yielded data that supported two but not three kernel parameters (Figure 8.1). This is consistent with Kiselev et al. (2007) and explains the prevalence of two-parameter models like NODDI and SMT in research. Tensor-valued diffusion encoding (QTI) yielded data that supported three parameters. This is consistent with Paper II and with Szczepankiewicz et al. (2016b). For high SNR, QTI would also support the four-parameter Standard model (Table 7.1). This is consistent with Coelho et al. (2019b) and Reisert et al. (2019), noting that the low precision in Figure 8.1 may reflect the absence of orientational information after powder averaging, as well as low sensitivity to the sixth phase cumulant for $b \leq 2.5$ ms/μm^2 (Kiselev et al. 2007, Ianuş et al. 2018). QTI extended to multiple $\mathbf{TE}$ for b-values in the low interval (DR_1) yielded data that supported the four-parameter diffusion model at all noise levels. This is consistent with results from Paper IV that diffusion-relaxation MRI may compensate for the lack of orientational information. However, the DR_1 data did not support any diffusion-relaxation model except under very high SNR conditions. This is consistent with results from Paper III, where in vivo use of this protocol did not support the PIII model. Even though DR_1 is sensitive to 7 observables, only $\mathbf{cov}(D_\mathrm{I}, R_2)$ provides information that can separate the components' T_2 values. This results in degeneracy when the difference in component diffusivities is small (here absent). Diffusion-relaxation MRI using multiple TE for b-values in the high interval (DR_2) yielded data that supported all models, including the seven-parameter diffusion-relaxation model (PIV+). This is consistent with in vivo results from Paper IV using this protocol. Being sensitive also to the tissue observable $\mathbf{cov}(\mathrm{V}_{\lambda,\mathrm{T}}[\mathbf{D}], R_2)$ (Eq. 6.31), DR_2 can separate the components' T_2 values based on their difference in anisotropy, which tends to be large between 'sticks' and 'zeppelins.'

8.4 Designing multidimensional dMRI acquisitions

The previous section showed that multidimensional dMRI data can be used to remove most assumptions on diffusion and T_2 relaxation (Figure 8.1). However, it also showed that the exact data requirements may be multifactorial and difficult to predict in each situation. The access to multiple encoding parameters also results in high protocol complexity, where a brute force strategy of using all encoding parameter combinations will inflate the acquisition time. Thus, it can be challenging to design a multidimensional acquisition protocol for practical purposes. In Papers I and IV, this problem was solved by optimizing acquisition protocols based on Cramer-Rao lower bounds (CRLB) (Rao 1945, Cramér 1946, Cercignani et al. 2006, Alexander 2008, Alexander et al. 2010, Coelho et al. 2019a). By finding a protocol that minimizes parameter variances approximated with CRLB, this approach can ensure both model support and experimental efficiency for relevant tissue priors.

8.4.1 Protocol optimization using Cramer-Rao lower bounds

CRLB are the diagonal elements of the inverse of the Fisher information matrix (F). For Gaussian noise with standard deviation σ_{noise}, F is given by (Alexander 2008)

$$F_{ij} = \sigma_{\mathrm{noise}}^{-2} \sum_{k=1}^{\mathrm{K}} \frac{\partial S_k}{\partial m_i} \frac{\partial S_k}{\partial m_j} (\mathbf{p}_k, \mathbf{m}), \tag{8.2}$$

where $\partial S_k / \partial m_{\mathrm{i}}$ and $\partial S_k / \partial m_{\mathrm{j}}$ are partial derivatives of the forward model $S(\mathbf{m}, \mathbf{p})$ with respect to the free model parameters m_i and m_j, and the sum is over the set of K encoding parameter combinations $\{\mathbf{p}_k\}$. Thus, the Fisher information matrix is a correlation matrix that describes the impact on the signal from variation in the model parameters. Conversely, the inverse Fisher information matrix describes the impact on (estimated) model parameters from variation in the signal, and thus the propagation of noise. It has been shown that if S is an unbiased model of $\mathbf{m}$, then the CLRB are lower bounds on the noise-induced variance on its estimates (Rao 1945, Cramér 1946)

The CRLB can be used to construct a metric for a protocol's efficiency at yielding data that determine the free parameters of a target model. In Paper IV, we defined the 'weighted parameter variance' (V_{W}), according to

$$V_{\mathrm{W}} = \tfrac{1}{\mathrm{J}} \textstyle\sum_j^{\mathrm{J}} \mathbf{w^T CRLB}_j \, f_{\mathrm{Tacq}}, \tag{8.3}$$

where $\mathbf{w^T}$ is a vector of weights, f_{Tacq} is an efficiency factor, and the average was taken across different sets of model priors. Weights were chosen for the metric to ignore certain

model parameters while bringing the remaining to comparable scales, and the factor $f_{\mathrm{Tacq}} = T_{\mathrm{Acq}}/T_{\mathrm{Acq;ref}}$ ensured that the metric reflected the protocol's efficiency rather than its absolute acquisition time.

Protocol optimization in Papers I and IV was performed as in Alexander (2008) using the Stochastic self-Organized Migrating Algorithm (SOMA) (Zelinka 2004), which is described in detail and available in open source at https://github.com/belampinen/lampinen_mrm_2019.

8.4.2 Optimized multidimensional dMRI in vivo

In Paper III, data were acquired using a naïve diffusion-relaxation acquisition protocol (Table 8.1, DR_1) with the aim to support a diffusion-relaxation model (Table 7.1, PIII). However, as demonstrated in Figure 8.1, this generally resulted in degeneracy in model fitting. Precise parameter estimates were only obtained in white matter lesions with large differences in isotropic diffusivities between components. In Paper IV, we optimized an acquisition protocol with the aim to support an extended diffusion-relaxation model (Table 7.1, PIV), based on a 15-minutes whole-brain acquisition on a MAGNETOM Prisma 3T system (Siemens Healthcare, Erlangen, Germany) using a multi-band factor 2 (Setsompop et al. 2012). The resulting protocol (adapted for an in vivo acquisition, Table 8.1, DR_2) yielded data that supported not only the PIII and PIV models but also the seven-parameter PIV+ model (Table 7.1), and thus removed all conventional assumptions on both diffusion and T_2 relaxation (Figure 8.2).

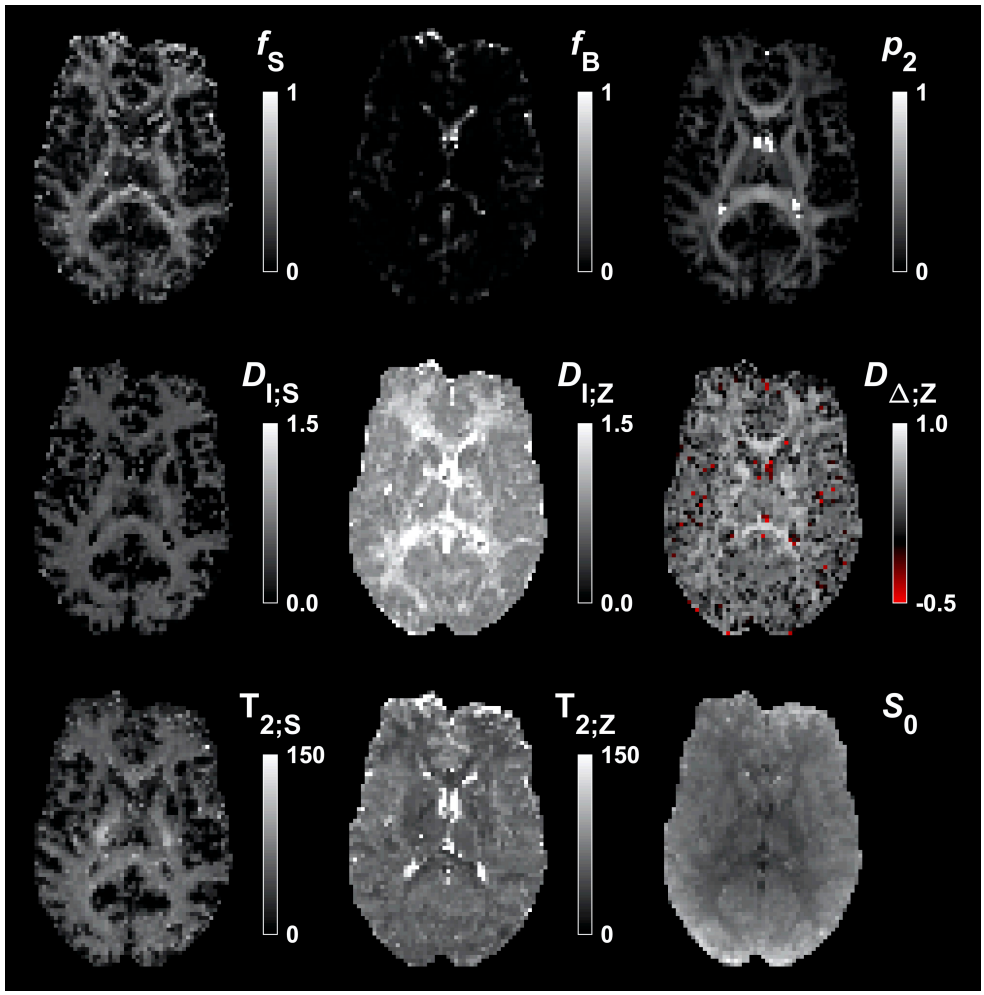

Figure 8.2 | In vivo maps of the seven kernel parameters of the PIV+ model (Table 7.1; together with p_2 and S_0). The maps were obtained using the DR_2 protocol (Table 8.1) in the brain of a healthy volunteer from Paper IV. Isotropic diffusivities are in $\mu m^2/ms$, T_2 values are in ms and remaining parameters are dimensionless. The 'stick' fraction (f_S) maps indicated high microscopic anisotropy in white matter but not in gray matter. The 'ball' fraction (f_B) maps were consistent with CSF. The orientation coherence (p_2) maps resembled FA maps. The maps of the 'stick' and 'zeppelin' isotropic diffusivities ($D_{I;S}$ and $D_{I;Z}$) were brightest in white matter tissue. The 'zeppelin' shape ($D_{\Delta;Z}$) maps were mostly positive (non-red), indicating no oblate diffusion tensors in the brain. The 'stick' T_2 value ($T_{2;S}$) maps were brighter than the 'zeppelin' T_2 value ($T_{2;Z}$) maps in white matter, and particularly in the cerebrospinal tract (cover image). The S_0 maps exhibited proton density-weighting rather than T_2-weighting, as expected. The figure was adapted, with permission, from Paper IV by Lampinen et al. (2020), published by Wiley.

9 The interpretation of microstructure model parameters

Microstructure models aim to estimate brain tissue quantities from dMRI data by fitting a forward model (Chapter 7) and use assumptions to avoid ambiguity of the inverse problem (Chapter 8). A unique solution does not guarantee a correct interpretation, however, since the estimated parameters could be biased in conditions where the assumptions do not hold true. Thus, the interpretation suggested for microstructure model parameters can be misleading. In Chapter 8, we showed that most model assumptions can be removed using multidimensional dMRI data. In this chapter, we use such data to test model assumptions and to investigate to what extent the interpretations suggested for microstructure model parameters can be trusted.

9.1 Model assumptions versus independent data

To test an individual model assumption, its associated parameter constraint can be compared with unconstrained parameter estimates obtained using independent data. To test a whole set of assumptions that defines a microstructure model, it can be assessed whether the model's fitted parameters can predict independent data. For example, acquired STE data can be compared with predicted STE data synthesized using a forward microstructure model with the model parameters obtained from a fitting that model to LTE data. Invariance with respect to data acquisition is a requirement for any method that aims to estimate true quantities, as these should not vary according to their estimation means.

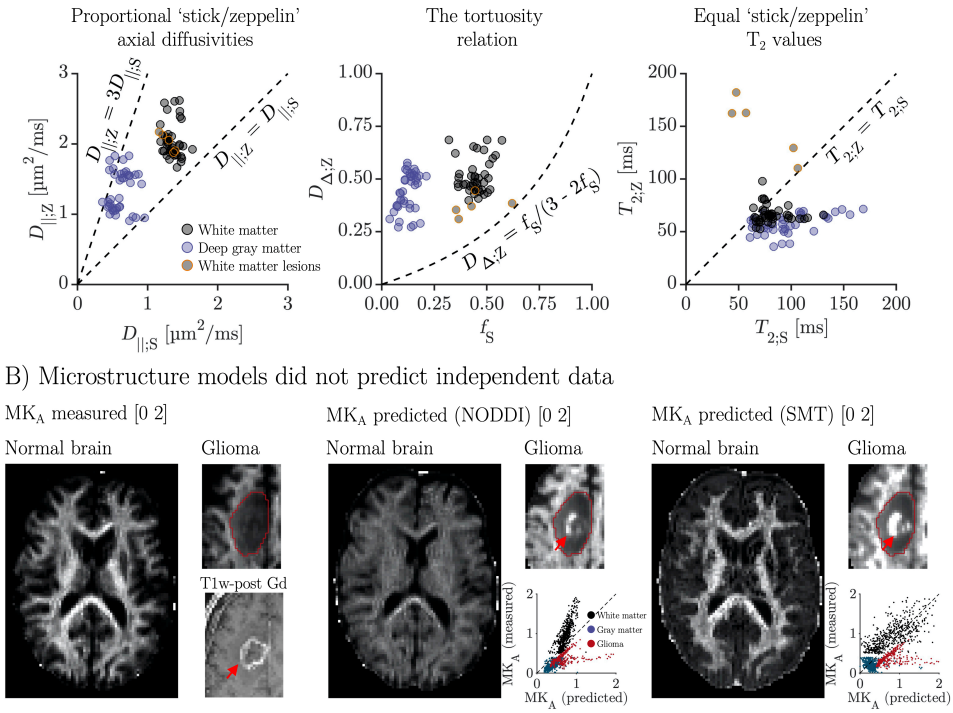

Figure 9.1 | Testing model assumptions with independent data. A) Parameter relations commonly assumed in models versus unconstrained estimates from Paper IV. The axial diffusivities of 'zeppelins' ($D_{\parallel;\mathrm{Z}}$) and 'sticks' ($D_{\parallel;\mathrm{S}}$) did not vary proportionally. While $D_{\parallel;\mathrm{Z}}$ was very variable, $D_{\parallel;\mathrm{S}}$ differed mainly between tissue types and featured lower values. The 'zeppelin' shape ($D_{\Delta;\mathrm{Z}}$) was more anisotropic than predicted by the tortuosity relation (Eq. 7.4) and exhibited high variability. The T_2 values were lower in 'zeppelins' ($T_{2;\mathrm{Z}}$) than in 'sticks' ($T_{2;\mathrm{S}}$) in normal brain, and the opposite held true in white matter lesions. The estimates were obtained by fitting the PIV model (Table 7.1) to data acquired using the DR_2 protocol (Table 8.1). B) Measured versus predicted $\mathrm{MK_A}$ in normal brain and a glioma brain tumor. NODDI predicted an $\mathrm{MK_A}$ that was comparatively low in white matter and high in gray matter. Both NODDI and SMT predicted a high $\mathrm{MK_A}$ in the contrast-enhancing region of the glioma ($\mathrm{T_1}$-weighted post-Gd). The measured $\mathrm{MK_A}$ was obtained by a covariance tensor analysis (Eq. 6.18) of LTE and STE data. The predicted $\mathrm{MK_A}$ was obtained by replacing the measured STE data by the STE data predicted by parameters obtained by fitting the NODDI and SMT models to the LTE data. The figure (A) was adapted, with permission, from Paper IV by Lampinen et al. (2020), published by Wiley.

9.1.1 Testing individual assumptions

Figure 9.1A shows results from Paper IV that compare independent parameter estimates with three commonly enforced parameter relations.

The axial diffusivities of 'sticks' ($D_{\parallel;\mathrm{S}}$) and 'zeppelins' ($D_{\parallel;\mathrm{Z}}$) did not vary proportionally across the normal brain and white matter lesions (Figure 9.1A), in contrary to common

assumptions (Behrens et al. 2003, Zhang et al. 2012, Kaden et al. 2016). In particular, the variation in axial diffusivities was considerably higher for 'zeppelins' than for 'sticks,' both in white matter and in deep gray matter. The axial diffusivity of 'sticks' was relatively different between these tissue types, however, which suggests that this parameter cannot be fixed to a single value in the brain. As a general observation, the axial diffusivities were markedly lower in 'sticks' than in 'zeppelins.' In white matter, this could possibly reflect a variation in axonal caliber that obstructs intra-axonal diffusion (Lee et al. 2019), although the difference in diffusivities was smaller in previous studies (Veraart et al. 2017, Novikov et al. 2018b, Dhital et al. 2019).

The 'zeppelin' shape ($D_{\Delta;\mathrm{Z}}$) was more anisotropic than predicted by the tortuosity relation (Eq. 7.4) and also exhibited high variability (Figure 9.1A). The relation in Eq. 7.4 was originally derived from simulations of diffusion around parallel cylinders (Szafer et al. 1995). In Paper IV, we point out that the use of this relation in microstructure modeling assumes that the 'stick' and 'zeppelin' components have the same geometric relationship as the intra- and extra-cylinder spaces in the simulation. However, this assumption ignores the presence of myelin around the true 'sticks' if these represent axons (Figure 3.1B, Eq. 3.1). Ignoring myelin should overestimate the volume fraction of the extracellular space and could explain the prediction of overly isotropic shapes. In Paper IV, we extended Eq. 7.4 to include myelin and showed that variability observed in 'zeppelin' shapes could reflect a variation in the g-ratio (Eq. 3.2) that was consistent with demyelination in the white matter lesions.

The T_2 of 'sticks' ($T_{2;\mathrm{S}}$) was higher than the T_2 of 'zeppelins' ($T_{2;\mathrm{Z}}$) in normal brain (Figure 9.1A), which contradicted the 'density assumption' of equal T_2 values (Eq. 7.7). In white matter, this is consistent with previous results, including a particularly high 'stick' T_2 in the cerebrospinal tract (cover image) (Veraart et al. 2017, McKinnon et al. 2019). If the 'stick' and 'zeppelin' components are interpreted as the intra- and extra-axonal space, then a lower 'zeppelin' T_2 could reflect exchange with short T_2 myelin water (Mackay et al. 1994, Dortch et al. 2013). In the cerebrospinal tract, the high 'stick' T_2 could reflect an axonal orientation parallel with the B_0 field (Knight et al. 2017, Birkl et al. 2021), or a large axonal diameter that reduces the surface-to-volume ratio and the exposure of intra-axonal water to membrane lipids with exchangeable protons (O'Brien et al. 1965). In white matter lesions, the T_2 of 'sticks' was similar to in normal white matter but the T_2 of 'zeppelins' was substantially increased, thus reversing the relationship seen in normal brain. This is consistent with lesions of the ischemic type, where histology has shown demyelination and loss of tissue integrity that enlarges the extracellular space (Englund et al. 1990) and increases T_2 (Englund et al. 1987). These results suggest that no reliable constraints can be placed on component T_2 values. The only consistent observation in normal brain was that the T_2 was lower in the 'zeppelin' than in the 'stick' component. However, the white matter lesions demonstrate how this does not hold true in conditions that involve oedema.

9.1.2 Testing entire models

In Paper II, we showed that the NODDI parameteters were not invariant with respect to the shape of the b-tensor in the normal brain. Fitting to STE data yielded very different results from fitting to LTE data, and the parameters obtained by fitting NODDI to LTE data could not be used to predict data acquired with STE. In Figure 9.1B, we show that neither NODDI nor SMT could accurately predict the microscopic kurtosis ($\mathrm{MK_A}$) in the normal brain or in a glioma brain tumor. In the normal brain, the measured $\mathrm{MK_A}$ was high in white matter and low in gray matter. The $\mathrm{MK_A}$ predicted by NODDI was comparatively low in white matter and high in gray matter, and thus featured a weaker contrast. The $\mathrm{MK_A}$ predicted by SMT was more alike in contrast to the measured $\mathrm{MK_A}$ but featured markedly higher values in white matter. In the glioma tumor, the measured $\mathrm{MK_A}$ was very low. However, both NODDI and SMT predicted high $\mathrm{MK_A}$ in the contrast-enhancing region. Thus, results indicate that the sets of assumptions used by NODDI and SMT are invalid in normal brain and in gliomas.

9.2 Invalid assumptions become confounders

In a model that aims to capture the true variation in brain tissue microstructure, tissue quantities that affect the signal but are not represented by free parameters must be accounted for by using assumptions—either explicitly (for example, Eq. 7.4) or implicitly by exclusion (for example, Eq. 7.7). When the true values of such quantities vary differently from the assumptions, they become confounders that bias the remaining free parameters and cause erroneous interpretations. In Figure 9.2, we simulate three scenarios that illustrate this effect on the interpretation of the NODDI and SMT 'stick' fractions (Table 7.1) as the neurite density. In each scenario, the true neurite density was represented by the volume fraction of 'stick' diffusion tensors, which was kept constant.

The first simulation (Figure 9.2A) challenged the models' ability to separate microscopic anisotropy with orientation dispersion from isotropic heterogeneity, which are entangled in SDE (Mitra 1995). Here, a variation in the variance in isotropic diffusivities among 'ball' diffusion tensors resulted in a variation in the NODDI and SMT 'stick' fractions, even though no 'sticks' were present. This confounding effect may explain findings of high 'neurite densities' in glioma tumors (Figure 9.1B) (Wen et al. 2015, Zhao et al. 2018), where no substantial amounts of neurites are expected but where high isotropic heterogeneity has been demonstrated (Szczepankiewicz et al. 2016a).

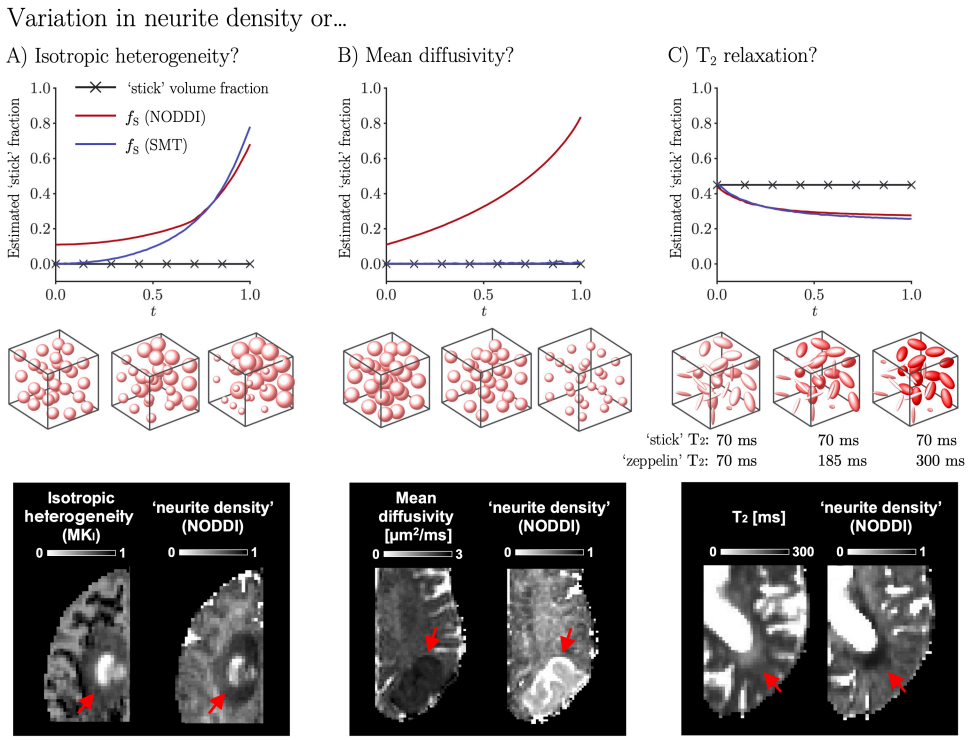

Figure 9.2 | Simulation of three scenarios where invalid assumptions confound the interpretation of the NODDI and SMT 'stick' fractinos (Table 7.1) as the neurite density (represented by the 'stick' volume fraction). The signal was generated using LTE with $b \leq 2.5$ ms/μm^2 and TE = 70 ms. A) The isotropic diffusivities of two sets of 'ball' diffusion tensors (equal volume fractions) were changed from $D_{\mathrm{I};1} = D_{\mathrm{I};2} = 1.3$ μm^2/ms to $D_{\mathrm{I};1} = 0.3$ μm^2/ms and $D_{\mathrm{I};2} = 2.3$ μm^2/ms. The NODDI and SMT 'stick' fractions were confounded by the independent variation of isotropic heterogeneity ($\mathrm{MK_I}$). This could explain findings of high 'neurite density' in glioma tumors. B) The isotropic diffusivities of 'ball' diffusion tensors were changed from $D_{\mathrm{I}} = 1.3$ μm^2/ms to $D_{\mathrm{I}} = 0.3$ μm^2/ms. The NODDI 'stick' fraction was confounded by the independent variation in mean diffusivity, which could explain increased 'neurite densities' in ischemic stroke. C) The 'zeppelin' T_2 value was changed between 70 and 300 ms while the 'stick' T_2 value was kept constant at 70 ms. This caused a variation in the 'stick' signal fraction that NODDI and SMT interpreted as a variation in neurite density. This effect may explain low 'neurite densities' in white matter lesions, where studies have reported changes in T_2 relaxation but minimal axon loss.

The second simulation (Figure 9.2B) challenged the NODDI assumptions that constrain all component diffusivities to estimate two fraction parameters (Table 7.1; Figure 7.1B). In Paper II, we show that this connects the neurite density to the mean diffusivity. Here, a variation in the isotropic diffusivity of 'ball' diffusion tensors resulted in a variation in the NODDI 'stick' fraction, even though no 'sticks' were present. This confounding effect may explain the high 'neurite density' detected by NODDI in acute ischemic stroke (Figure 9.2B, data from Paper VI) (Caverzasi et al. 2016, Wang et al. 2019), which induces a reduction

in mean diffusivity (Moseley et al. 1990). This effect should also explain the high MK_A predicted by NODDI in gray matter (Figure 9.1B) and why the NODDI 'stick' fraction was never non-zero in Figure 9.2A.

The third simulation (Figure 9.2C) challenged the density assumption of equal component T_2 values (Eq. 7.7) that is used to estimate the neurite density from the 'stick' signal fraction, which is ambiguous at a single TE (Eq. 7.6). Here, a variation of the 'zeppelin' T_2 value resulted in a variation in the NODDI and SMT 'stick' fractions that was unrelated to the neurite density. This confounding effect may explain the low 'neurite density' detected by NODDI in white matter lesions (Figure 9.2C, data from Paper IV), where histology has reported minimal axon loss (Coelho et al. 2018) but where extracellular oedema (Englund et al. 1990) could increase 'zeppelin' T_2 values (Englund et al. 1987).

9.3 The interpretation of model parameters has a small domain of validity

In previous sections, we demonstrated how assumptions of microstructure models were contradicted by independent data (Figure 9.1), and how invalid assumptions become confounders that bias the remaining free parameters (Figure 9.2). One may ask, however, whether such bias is of practical importance. An absolute numerical trueness of model parameters with respect to their target tissue quantities may not be necessary and is rarely claimed. Instead, one may argue that microstructure model parameters are useful as *indices* of tissue quantities (Zhang et al. 2012, Kaden et al. 2016). Such an index could lack absolute trueness but feature ordinal trueness, meaning that it correctly ranks observations from low to high with respect to a given quantity. An important question, then, is whether invalid assumptions become sufficiently large confounders to affect the ordinal trueness of model parameters.

In Paper III, we assessed the index property of the 'stick' fractions from contemporary models by comparing their rankings of different regions from normal brain tissue and white matter lesions (Figure 9.3). There, fitting six different microstructure models to the same data resulted in four different rankings of seven regions with respect to the 'stick' fraction. Since there can only be one true ranking with respect to a given tissue quantity, this means that the 'stick' fraction parameter of most of these models lack the ordinal trueness of an index across these regions. The conclusion was that the interpretation suggested for microstructure model parameters has a small 'domain of validity.'

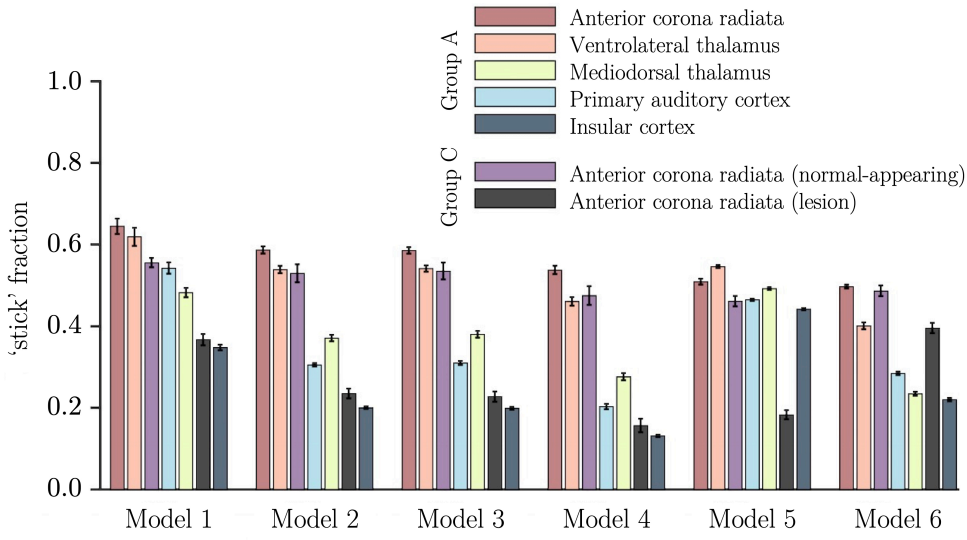

Figure 9.3 | Fitting six microstructure models to the same data resulted in significantly different rankings of seven regions from normal brain and white matter lesions ($p = 0.025$, permutation-based test, Paper III). Thus, the result of comparisons between brain regions depended on the choice of assumptions. For example, using model C1 would indicate a higher 'neurite density' in the mediodorsal thalamus than in white matter lesions, while model C6 would indicate the opposite. The figure was adapted, with permission, from Paper III by Lampinen et al. (2019), published by Wiley.

The domain of validity of microstructure model parameters can be expanded by using multidimensional dMRI to remove assumptions (Figure 8.1; Table 8.1) as well as their associated confounders (Figure 9.2). In Paper IV, we used diffusion-relaxation MRI with tensor-valued diffusion encoding (Table 8.1, DR_2) to remove the assumptions on both component diffusivities and T_2 relaxation. Accordingly, the resulting parameters (Figure 8.2) should be less biased in tissue types and conditions where these properties vary independently, including: gliomas (Figures 9.1B and 9.2A) (Wen et al. 2015, Szczepankiewicz et al. 2016a, Zhao et al. 2018), ischemic stroke (Figure 9.2B) (Caverzasi et al. 2016, Wang et al. 2019), oedematose conditions such as white matter lesions (Paper III; Figures 9.1A and 9.2C) (Englund et al. 1987, Englund et al. 1990), and the normal brain (Figure 9.1, Paper II).

Even the relatively unconstrained models presented in Paper IV (Table 7.1, PIV and PIV+) are incomplete. For example, to interpret the 'stick' fraction of PIV+ (Figure 8.2) in white matter as the axonal density ignores the presence of myelin (Eq. 3.1, Figure 3.1B). Variation in myelin content could confound this parameter like variation in T_2 relaxation confounds the 'stick' fractions from contemporary models (Figure 9.2C). Thus, its domain of validity may not encompass conditions that feature a combination of demyelination and axonal loss, such as multiple sclerosis (Criste et al. 2014). Moreover, component signal fractions are affected by T_1

relaxation. Even though dMRI is usually weakly T_1-weighted, severe variations in T_1 could be a confounder, for example, in oedema (Englund et al. 1987) or in acquisitions using a very short repetition time (Hutter et al. 2018). To further expand the domain of validity may require data acquired with very short **TE** to account for myelin water, sensitivity to proton density to account for myelin lipid (Stikov et al. 2011, Stikov et al. 2015), and multiple repetition times (de Almeida Martins et al. 2018, Hutter et al. 2018) or inversion recovery (De Santis et al. 2016, Benjamini et al. 2018) to account for T_1 relaxation.

10 The interpretation of microscopic diffusion anisotropy in the brain

To estimate the properties of neurites, microstructure models assume that axons and dendrites induce a similarly high level of microscopic anisotropy to be jointly represented by a 'stick' component (Jespersen et al. 2007, Jespersen et al. 2010, Zhang et al. 2012, White et al. 2013, Kaden et al. 2016). Until recently, the validity of this 'neurite assumption' has been difficult to assess since the level of microscopic anisotropy in gray matter is obscured by orientation dispersion in SDE (Mitra 1995). In Papers II–V, we used tensor-valued diffusion encoding to overcome that issue.

10.1 Microscopic anisotropy reflects axons but not neurites

In Papers II and III, we found that the level of microscopic diffusion anisotropy, as quantified by the $\mathrm{MK_A}$, was considerably lower in gray matter than in white matter (Figure 10.1A). This did not agree with the neurite assumption; that is, that axons and dendrites induce similar levels of microscopic anisotropy. If this was the case, then the level of $\mathrm{MK_A}$ should reflect the signal fraction from neurites. Histology shows that neurite signal fractions should be similar in gray and white matter (Section 3.2, discounting short $\mathrm{T_2}$ myelin), wherefore the neurite assumption predicts a similar $\mathrm{MK_A}$ between these tissue types. The low $\mathrm{MK_A}$ found in gray matter instead suggests that dendrites induce a relatively low level of microscopic anisotropy. Alternatively, the signal fraction of gray matter neurites could be reduced by a low $\mathrm{T_2}$ value (Figure 9.2C).

A) Microscopic anisotropy did not reflect neurites

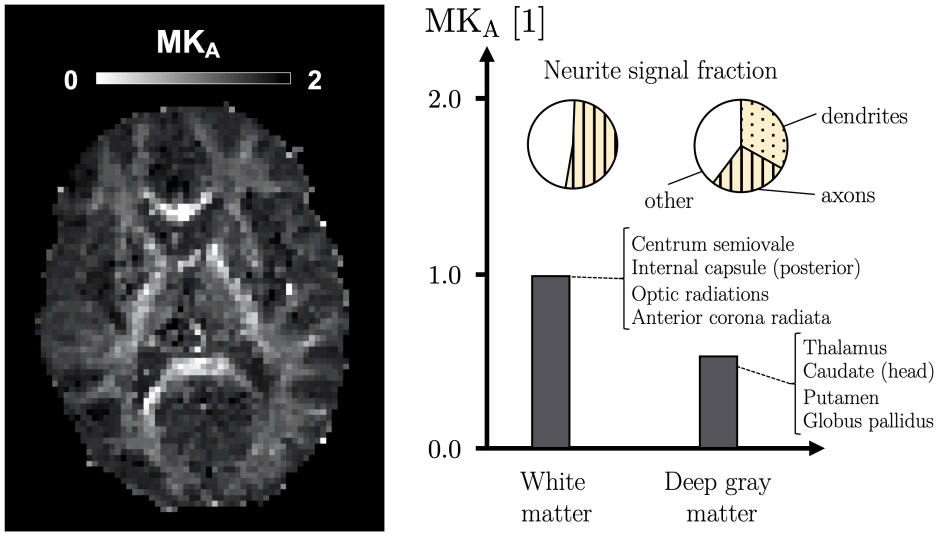

B) The 'stick' fraction reflected axons but not neurites

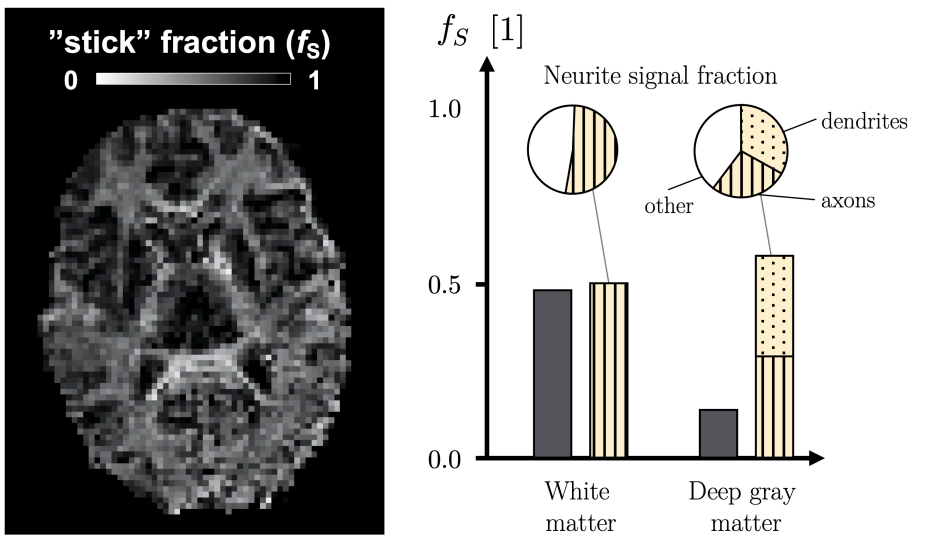

Figure 10.1 | Microscopic anisotropy reflects axons but not neurites. A) The MK_A was considerably higher in white matter than in gray matter, even though histology predicts similar neurite signal fractions (Section 3.2, discounting short T_2 myelin). B) The (T_2-independent) 'stick' fraction reflected the axonal signal fraction expected from histology in white matter ($f_S \approx 0.48$ vs. $f_n \approx 0.52$) but not in gray matter ($f_S \approx 0.14$ in deep gray matter vs. $f_n \approx 0.60$ in the cortex). The dMRI data were obtained with the DR_2 protocol (Table 8.1) from five healthy volunteers in Paper IV and the parameter values are inter-subject averages from four different white and deep gray matter regions. The MK_A was estimated by fitting Eq. 6.18 (for a subset of data) and the stick' fraction (f_S) was estimated by fitting the PIV model (Table 7.1).

In Paper IV, we found that the 'stick' fraction estimated independently of T_2 relaxation (Table 7.1 PIV) was considerably lower in deep gray matter than in white matter (Figure 10.1B). When compared with knowledge from histology (Section 3.2), the 'stick' fraction was close to the expected signal fraction of axons in white matter but lower than the expected signal fractions of either axons or dendrites in cortical gray matter. If axons contribute to the 'stick' fraction also in gray matter, this result indicates a near negligible contribution from dendrites and contradicts the neurite assumption.

10.2 Microscopic anisotropy correlates with myelin

In Paper III, we noted that maps of microscopic anisotropy, as quantified by the $\mathrm{MK_A}$, bore a similarity to myelin stains (Figure 10.2A). In particular, $\mathrm{MK_A}$ maps exhibited a similar intensity gradient from the low-myelin medial thalamus, through the high-myelin lateral thalamus, and into the white matter of the internal capsule. We further studied this relationship in the cortical gray matter of twenty healthy subjects in Paper III. We found that $\mathrm{MK_A}$ was significantly higher in cortical regions that were expected from histological studies to feature a high myelin content compared with cortical regions that were expected to feature a low myelin content (Figure 10.2B). Here, in Figure 10.2C, we compare $\mathrm{MK_A}$ values from regions across the whole brain with corresponding values of the myelin water fraction obtained by Whittall et al. (1997) using multi-exponential T_2 analysis. This revealed a strong linear correlation ($\rho \approx \mathbf{0.93}$, Pearson's r), where brain regions with lower myelin water fractions exhibited lower $\mathrm{MK_A}$, and vice versa. Also, the intercept of approximately zero indicated that the variation in microscopic anisotropy across the brain could be sufficiently explained by myelin, and thus axons, without any contribution from dendrites.

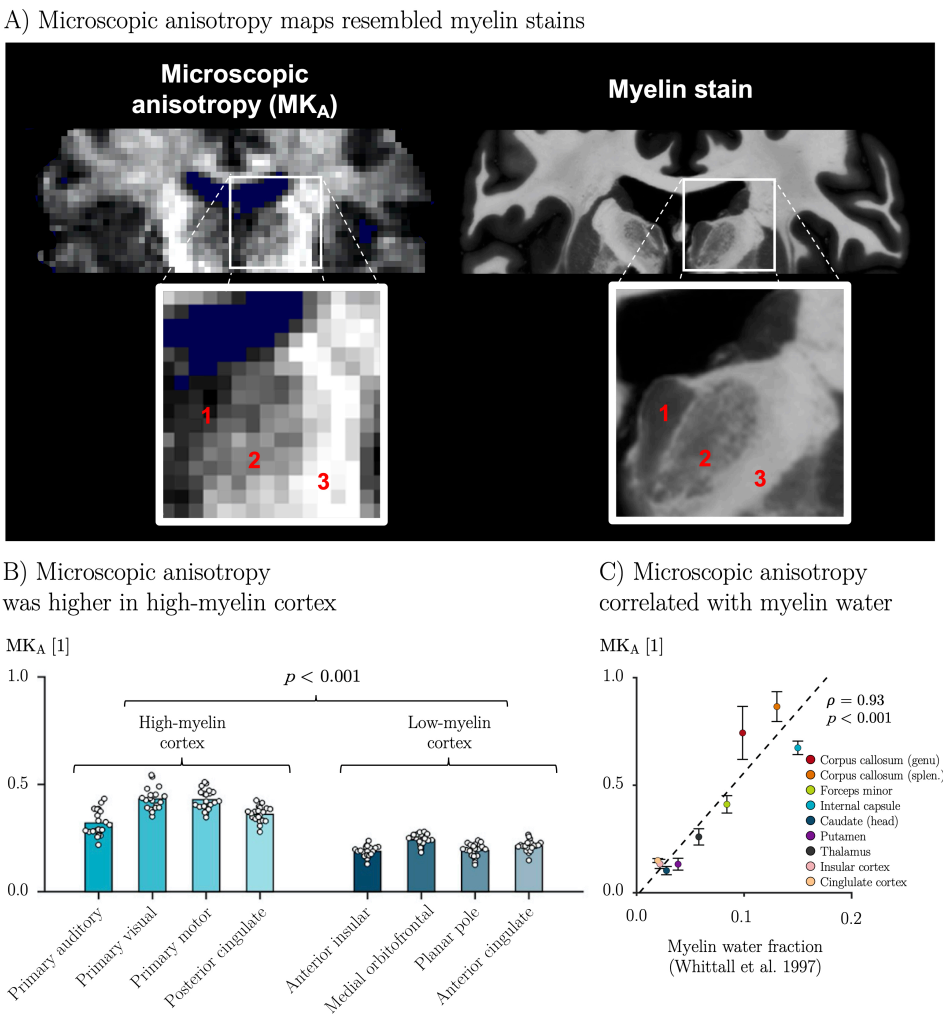

Figure 10.2 | Microscopic diffusion anisotropy was related to myelin (Paper III). A) MK_A maps resembled myelin stains down to the detail level, as seen from intensity gradient between the medial (1) and lateral (2) thalamus and the internal capsule (3). B) The MK_A was significantly higher in cortical regions expected from histology to feature a high myelin content ($p < 0.001$, two-sided t-test). C) MK_A values from across the whole brain (Paper II, averaged across the five Group A subjects) were almost entirely explained by the myelin water fraction reported in Whittall et al. (1997). The figure (A and B) was adapted, with permission, from Paper III by Lampinen et al. (2019), published by Wiley.

10.3 Microscopic anisotropy reveals axons in malformations of cortical development

In Paper V, we used tensor-valued diffusion encoding to estimate the $\mathrm{MK_A}$ in malformations of cortical development (MCD, Figure 10.3). MCD result from disrupted neuronal development and migration and consist of abnormal and disorganized gray matter (Guerrini et al. 2008). Anatomically, MCD may be located in both the cortex and white matter (Figure 10.3B and C) or by the ventricular walls (Figure 10.3A).

On T_1-weighted images, the MCD were seen as isointense with normal gray matter (Figure 10.3), which is typically associated with a low myelin content (Holland et al. 1986).

On the $\mathrm{MK_A}$ maps, some lesions were similarly isointense with gray matter (Figure 10.3A, blue arrow), exhibiting low levels that are typically seen outside white matter (Fig. 10.1A). However, some lesions exhibited mixed levels of $\mathrm{MK_A}$; with low levels in regions located anatomically in the cortex and high levels in regions located anatomically in white matter (Figure 10.3B and C, yellow arrows).

The high $\mathrm{MK_A}$ in some lesion regions suggested a higher content of a microstructural component that induces high microscopic anisotropy without affecting the T_1 properties (Figure 10.3). That component was unlikely to be dendrites, seeing that normal gray matter has low $\mathrm{MK_A}$ despite being dendrite-rich (Figure 10.1A). Instead, we hypothesized that the high-$\mathrm{MK_A}$ regions represented subcortical white matter that was myelin-poor, and therefore hypointense on T_1, but whose high axonal content still induced a high level of microscopic anisotropy. This interpretation is consistent with histopathology, which has demonstrated reduced myelin content in white matter adjacent to MCD (Colombo et al. 2009). Overall, the finding is consistent with axons as the main drivers of microscopic anisotropy, with a smaller role for myelin (Beaulieu 2002) and a minimal role for dendrites.

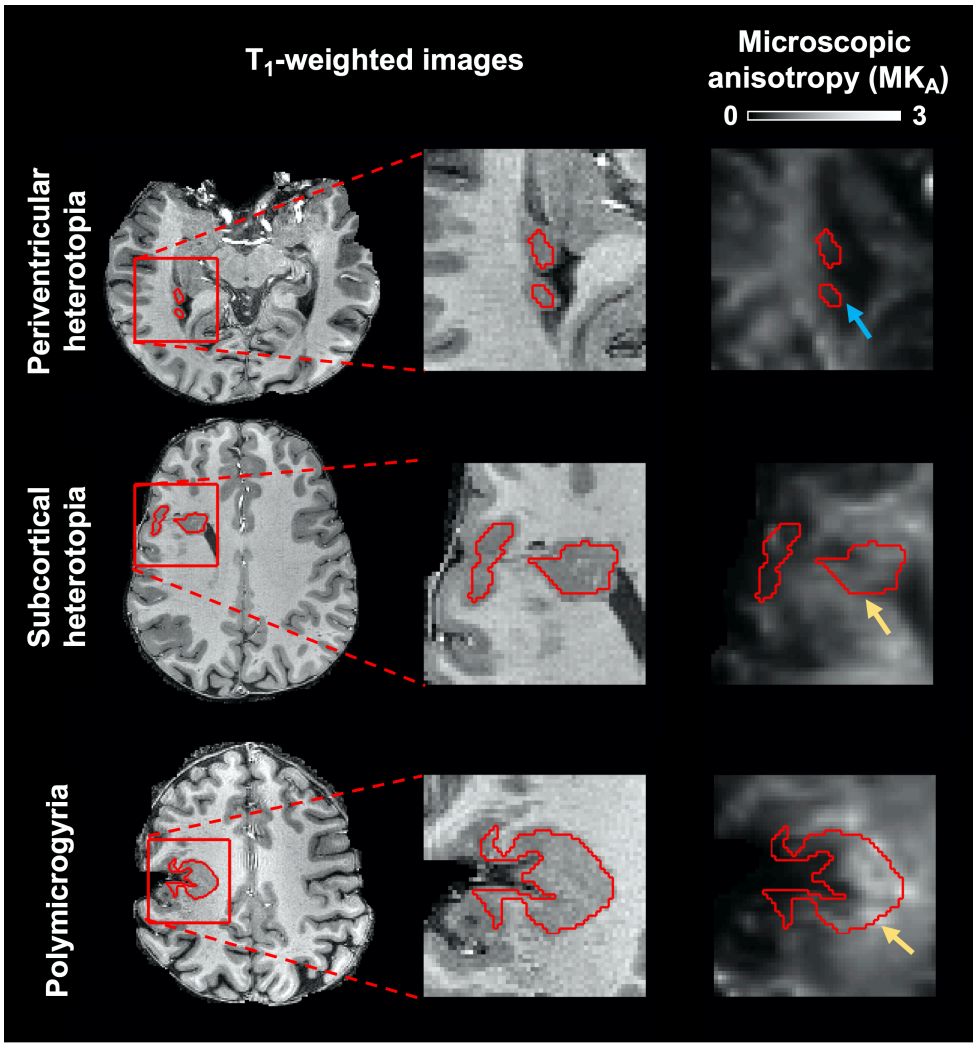

Figure 10.3 | Microscopic diffusion anisotropy revealed white matter-like regions in malformations of cortical development (MCD, Paper V). The MCD could be seen by the ventricles (top example), in white matter (middle example) or in the cortex (bottom examlpe) as abnormalities that were isointense with normal gray matter on T_1-weighted images. Some lesions were isointense with gray matter also on the MK_A (blue arrow). However, some lesions exhibited bright white matter-like regions (yellow arrows), particularly in the parts that were located anatomically in white matter. The figure was adapted, with permission, from Paper V by Lampinen et al. (2020), published by Wiley.

10.4 Microscopic anisotropy is an axon-based contrast

Our results with tensor-valued diffusion encoding suggest that microscopic diffusion anisotropy reflects axons but not dendrites, and thus contradict the neurite hypothesis. This is consistent with previous findings in normal brain (Lawrenz et al. 2018, Novikov et al. 2018b, Veraart et al. 2020) and in fixed tissue (Jespersen et al. 2010). The finding was not explained by T_2 relaxation (Figure 9.1B), and primarily suggest that the intra-dendritic space is not an environment with microscopically anisotropic diffusion on the time scale of dMRI measurements at clinical scanners. This could reflect that dendritic water undergoes fast diffusional exchange—a phenomenon that has been demonstrated in cortical gray matter of rats in vivo (Pfeuffer et al. 1998, Jelescu et al. 2021, Zhang et al. 2021) and ex vivo (Olesen et al. 2021). Fast exchange between dendrites and the extracellular space might be facilitated by water-permeable channels that are involved in swelling-induced volume regulation (Akita et al. 2014), or by a larger surface area conferred by dendritic spines. Fast exchange could plausibly occur also between dendritic segments with different orientations or between dendrites and soma.

The finding that microscopic anisotropy reflects axons but not dendrites has two important implications. On the one hand, microscopic anisotropy cannot be used to infer the properties of neurites, in contrary to what has been suggested (Jespersen et al. 2007, Jespersen et al. 2010, Zhang et al. 2012, White et al. 2013, Kaden et al. 2016). Thus, 'stick' fraction parameters should aim to capture axons, when not confounded by other phenomena (Figure 9.2). On the other hand, microscopic anisotropy may be a uniquely axon-based contrast. Parameters such as the $\mathrm{MK_A}$ may, therefore, provide more robust differentiation between gray and white matter in conditions that involve alterations to myelin content—which is a main determinant of conventional T_1- and T_2-weighted contrasts in the brain (Holland et al. 1986) (Figure 10.3). This could be important, for example, in malformations of cortical development, by improving the MRI delineation of lesions in the presurgical evaluation of epilepsy (Duncan et al. 2016) or in the evaluation of cortical thickness (Natu et al. 2019), for example, as a marker of progression in Alzheimer's disease (Cullen et al. 2020).

11 The role of diffusional exchange in normal brain and pathology

The previous chapters assumed diffusion in non-exchanging Gaussian environments described by a DTD (Chapter 5). This is known to be an approximation since diffusional exchange occurs continuously between different cellular components of brain tissue (Amiry-Moghaddam et al. 2003). In this chapter, we first overview water permeability mechanisms. We then discuss the impact of diffusional exchange on the DTD description of diffusion and on the statistical DTD properties that are encoded into the dMRI signal. Then, we describe two different techniques for exchange-encoding in dMRI. Finally, we use these techniques to assess the impact of exchange on dMRI in normal brain and to explore the clinical potential of exchange in intracranial tumors and in ischemic stroke.

11.1 Permeability of brain cell membranes

Diffusional water exchange is tightly linked to the permeability of cell membranes, which are the main barriers for diffusion between microscopic environments in the brain . Cell membranes are semipermeable, which means that they allow differential passage of water and solutes. The membrane water permeability (P) has the units of volume flow per unit area and defines two separate quantities. *Osmotic* water permeability (P_{osm}) regulates net flow in the presence of an osmotic gradient. *Diffusional* water permeability (P_{d}) is generally smaller and regulates the net zero flow that results from thermally driven diffusion (Reuss 2012). In the context of dMRI, we assume the absence of osmotic gradients and thus net flow, and permeability always refers to P_{d}. Below, we review three factors that influence permeability.

11.1.1 Membrane lipid composition

Upon collision with a cell membrane, a water molecule has a non-zero probability to partition into the hydrophobic lipid core and diffuse to the other side. This process is referred to as solubility-diffusion and is facilitated by higher membrane fluidity. Factors that increase fluidity include high temperature, high content of phospholipids with unsaturated lipid chains, and low content of cholesterol (Reuss 2012).

11.1.2 Water-selective aquaporins

Aquaporins (AQP) is a family of narrow-pore (approximately 28 nm) membrane channels with high selectivity for water molecules (Reuss 2012), whose discovery was awarded the 2003 Nobel Prize in Chemistry (Agre 2004). Cellular AQP expression greatly increases its membrane water permeability (King et al. 2004). This function is important, for example, in the kidney for controlled re-uptake of water, and in red blood cells for deformation in narrow capillaries (Reuss 2012). In the brain, three AQP isoforms have been identified. AQP1 is present in ependymal cells of the choroid plexuses where it may facilitate CSF-secretion (Oshio et al. 2005). AQP9 is known to be present in some ependymal cells that line the ventricles but have an unclear role (Amiry-Moghaddam et al. 2003). AQP4 is considered the predominant AQP of the brain and is particularly found in astrocytes (Amiry-Moghaddam et al. 2003).

The AQP4 of astrocytes have an important role in brain water transport. To exit or enter brain tissue, water must pass through a barrier whose permeability is largely determined by astrocytic AQP4 expression (King et al. 2004, Papadopoulos et al. 2007). Between blood and tissue, astrocytic end-feet contribute to the blood-brain-barrier by enveloping the endothelial cells of all brain capillaries. Between CSF and tissue, astrocytic end-feet form the so-called glia limitans that lines the ventricular, subarachnoid, and perivascular spaces (Papadopoulos et al. 2007). At these locations, the astrocytic membranes feature an order of magnitude larger concentrations of AQP4 (Amiry-Moghaddam et al. 2003). Inside brain tissue, water and solutes can also move rapidly through the intracellular network formed by astrocytes interconnected with gap-junctions (Amiry-Moghaddam et al. 2003, Sofroniew et al. 2010, Iliff et al. 2012). In rat brain, inhibition of AQP4-expression caused a 50% reduction in the apparent diffusion coefficient (Badaut et al. 2011).

11.1.3 Large non-selective membrane channels

Some large membrane channels may permit sufficient non-selective passage of water to significantly impact membrane water permeability.

The volume regulatory anion channel (VRAC) is present in both neurons and astrocytes and has a wide pore (110–120 nm) (Akita et al. 2014) that may allow non-selective passage of water (Nilius 2004a). VRAC are involved in compensatory volume regulation in response to cellular swelling. Membrane permeability to negatively charged solutes (anions) is dramatically increased when the channel is open, which results in a net outward flux and osmotic shrinking (Akita et al. 2014).

The urea transporter UT-B1 is a membrane channel protein expressed by astrocytes (Berger et al. 1998), which may allow non-selective passage of water with similar permeability as AQP (Yang et al. 1998). UT-B1 facilitates the elimination of urea, a toxic waste product from protein catabolism (Ogami et al. 2006). It is upregulated in gliosis, which may reflect the increased urea turnover associated with healing (Berger et al. 1998).

11.2 Diffusion in an ensemble of Gaussian environments with exchange

The impact of diffusional exchange in an ensemble of Gaussian environments is determined by the environments' exchange times $\tau_{\mathrm{ex};j}$ —the average durations of residence for water molecules in each environment before exchange occurs. The assumption of non-exchanging environments during the diffusion time T_{d} can be defined as $\tau_{\mathrm{ex};j} \gg T_{\mathrm{d}}$ for all j, meaning that each water molecule only experiences a single environment. The introduction of exchange among environments can be defined as $\tau_{\mathrm{ex};j} \sim T_{\mathrm{d}}$ for some j, meaning that some water molecules experience multiple environments. Finally, the condition of 'barrier-limited' exchange can be defined as $\tau_{\mathrm{ex};j} \gg \tau_{\mathrm{c}}$ for all j, meaning that water molecules spend sufficient time in each environment to make many statistically independent displacements and preserve Gaussian diffusion by the central limit theorem. The barrier-limited term is reflective of the fact that the probability of exchange for each particle is determined by barrier permeability rather than the particle's initial distance to barriers.

11.2.1 The Kärger model

The Kärger model describes exchange between two one-dimensional components (Kärger 1985), and can be seen as a minimal model of diffusion in an ensemble of Gaussian environments with exchange. The components are described by the fractions f_1 and $f_2 = 1 - f_1$ and the diffusion coefficients D_1 and D_2. Exchange between the components is determined by the outward rate constants $k_{\overline{12}}$ and $k_{\overline{21}}$, which are the fractions of particles in each component that move to the other component per unit time. Exchange rates are related to the exchange times, according to $k_{\overline{12}} = 1/\tau_{\mathrm{ex};1}$ and $k_{\overline{21}} = 1/\tau_{\mathrm{ex};2}$. The effective exchange rate can be defined as (Åslund et al. 2009)

$$k = k_{\overline{12}} + k_{\overline{21}} = \frac{1}{\tau_{\mathrm{ex};1}(1 - f_1)}, \tag{11.1}$$

using conservation of mass, according to $f_1 k_{\overline{12}} = f_2 k_{\overline{21}}$.

If the Kärger model components are interpreted as intra- and extracellular spaces in a system of cells suspended in water, then the exchange rate is related to the surface-to-volume ratio A/V and membrane permeability P_{d} of cells according to (Åslund et al. 2009)

$$k = P_{\mathrm{d}} \frac{A}{V}. \tag{11.2}$$

11.2.2 Diffusional exchange and the dMRI signal

The cumulants c_2 and c_4 of the phase distribution $P(\phi)$ were derived for the (one-dimensional) Kärger model by Ning et al (Ning et al. 2018), according to

$$c_2 = 2b(f_1 D_1 + f_2 D_2) = 2b\mathrm{MD} \tag{11.3}$$

and

$$\begin{aligned} c_4 &= 12b^2 \mathrm{V}[D]h, \text{where} \\ h &= \frac{2}{b^2} \int_0^{\mathrm{TE}} \exp(-kt)\, q_4(t) dt \text{ and} \\ q_4(t) &= \int_0^{\mathrm{TE}} q^2(t_1) q^2(t_1 + t) dt_1, \end{aligned} \tag{11.4}$$

where $\mathrm{V}[D]$ is the diffusional variance, k is from Eq. 11.1 and q is from Eq. 6.2. This yields the signal expression

$$S = S_0 \exp\left(-b \cdot \mathrm{MD} + \frac{1}{6} b^2 \cdot \mathrm{MK}h \cdot \mathrm{MD}^2\right), \tag{11.5}$$

where MK corresponds to the $\mathrm{MK_T}$ parameter (Eq. 6.27, $b_\Delta = 1$) in the absence of exchange ($k = 0$).

11.2.3 The impact of diffusional exchange on dMRI

In an ensemble of Gaussian environments with (barrier-limited) exchange, individual water molecules experience multiple environments with Gaussian diffusion and therefore have multi-Gaussian displacement paths. The second cumulant of the phase distribution is unaffected by such exchange (Eq. 11.3) because it is sensitive to the average absolute displacement among spin-carrying particles. By conservation of mass, any reduction in displacement experienced by one particle that enters an environment with lower diffusivity is offset by a corresponding increase in displacement experienced by another particle that exits that environment. The fourth phase cumulant is affected (11.4), however, because it is sensitive to the variance in absolute displacement among spin-carrying particles. Increasing exchange allows each particle to experience more of the total environment and results in more similar absolute displacements among particles.

An ensemble of Gaussian environments with exchange generalizes the conditions described in sections 6.3 and 6.4 to two extremes. For very slow exchange, $k \to 0$, $h \to 1$ (Eq. 11.4) and diffusional variance has maximal impact. All individual displacement paths occur within single environments and the ensemble can be described by a DTD. For very fast exchange, $k \to \infty$ and $h \to 0$ (11.4), diffusional variance has zero impact. All displacement paths reflect the average environment, which makes the central limit theorem valid for the whole ensemble and allows it to be described by a single diffusion tensor.

11.2.4 Three regimes of diffusional exchange

In Figure 11.1, we assessed the impact of exchange on dMRI by plotting MD and MK against the intracellular exchange time ($\tau_\mathrm{i} \equiv \tau_{\mathrm{ex};1}$, Eq. 11.1). This suggested three relatively non-overlapping regimes of exchange. First (shown in green), for intracellular exchange times approximately one order of magnitude longer than the diffusion time (T_d), exchange had no appreciable effect on either MD or MK. We refer to this as the 'slow regime' of minimal impact, where the ensemble is effectively non-exchanging and can be described by a DTD. Second (shown in yellow), for shorter intracellular exchange times, MK was progressively reduced towards zero while MD remained relatively unaffected. We refer to this as the 'intermediate regime' that is most simply described by the Kärger model. Third (shown in red), for intracellular exchange times approximately one order of magnitude shorter than the diffusion time, MD was progressively increased towards the diffusivity of the fast component and MK was approximately zero. We refer to this as the 'fast regime,' where the exchange is no longer barrier-limited.

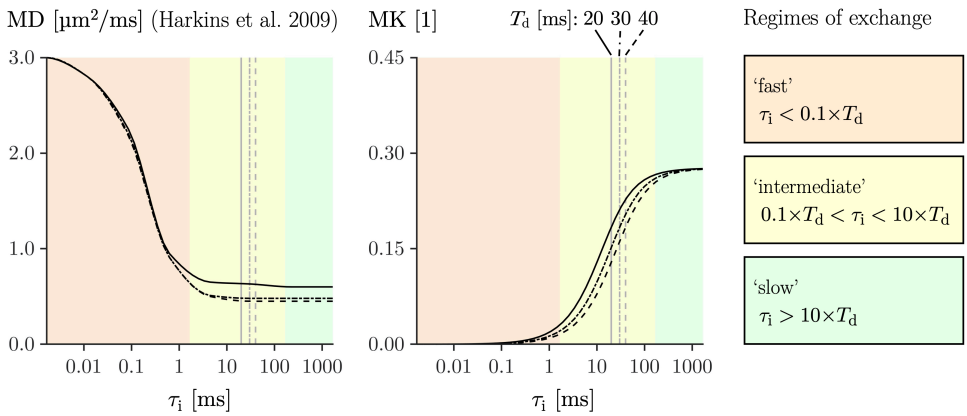

Figure 11.1 | Plotting MD and MK against the intracellular exchange time (τ_i) suggested three regimes of exchange. In the 'slow regime' (green), for τ_i approximately one order of magnitude longer than the diffusion time (T_d), diffusion affected neither MD nor MK. In the 'intermediate regime' (yellow), for shorter τ_i, MD remained unaffected but MK was reduced towards zero. In the 'fast regime' (red), for τ_i approximately one order of magnitude shorter than T_d, MD was increased toward the diffusivity of free water. MD values were borrowed from (Harkins et al. 2009). MK values were obtained by fitting Eq. 6.28 to data synthesized using $b \leq 2.5$ ms/μm^2, $b_\Delta = 1$ and $T_\mathrm{d} \in \{20\ 30\ 40\}$ ms with the Kärger forward model and the priors from (Harkins et al. 2009): $f_1 = 0.8$, $D_1 = 1$ μm^2/ms, $D_2 = 3$ μm^2/ms and τ_i logarithmically spaced between 1.7×10^{-3} and 1700 ms. The figure was adapted, with permission, from (Harkins et al. 2009), published by Wiley.

11.3 Exchange-encoding in dMRI

Diffusional exchange can be estimated by acquiring dMRI data using exchange-sensitive encoding parameters, describing its effect on the signal with a forward model and solving the inverse problem. Two techniques for exchange estimation were used in this thesis: SDE with multiple diffusion times (Paper VI) and filter exchange imaging (FEXI; Paper I).

11.3.1 SDE with multiple diffusion times

A forward model of the SDE signal including exchange based on Eqs. 11.3 and 11.4 has been presented by Ning et al. (2018). For small products kt, where $\exp(-kt) \approx 1 - kt$, Ning et al defined an exchange-sensitive encoding parameter Γ, or 'exchange-weighting time,' according to

$$\begin{aligned} h &\approx 1 - \Gamma k, \text{where} \\ \Gamma &= \frac{2}{b^2}\int_0^T t q_4(t) dt. \end{aligned} \tag{11.6}$$

This yields a simplified forward model of exchange, according to

$$S = S_0 \exp\left(-b \cdot \mathrm{MD} + \frac{1}{6} b^2 \cdot \mathrm{MK}(1 - \Gamma k) \cdot \mathrm{MD}^2\right) \tag{11.7}$$

The exchange rate k can be estimated by fitting Eq. 11.7 to powder-averaged data acquired with b-values in the high interval for multiple Γ (Paper VI).

11.3.2 Filter exchange imaging (FEXI)

The effects of diffusional exchange are entangled with the opposing effects of restricted diffusion for SDE with multiple diffusion times (Nilsson et al. 2009). To overcome this, the FEXI sequence uses a DDE design with constant diffusion times and a variable mixing time to isolate the effects of exchange (Figure 11.2A) (Callaghan et al. 2004, Åslund et al. 2009, Lasič et al. 2011).

FEXI estimates the apparent exchange rate (AXR) by analysing the equilibration of labeled spins (Figure 11.2B) (Lasič et al. 2011). The analysis is based on the Kärger model (Section 11.2.1) with a 'fast component' (F), described by f_F and D_F, and a 'slow component' (S) described by f_S and D_S, where $f_\mathrm{F} = 1 - f_\mathrm{S}$ and $D_\mathrm{F} > D_\mathrm{S}$. The mean diffusivity is given by

$$\mathrm{MD} = f_\mathrm{F} D_\mathrm{F} + f_\mathrm{S} D_\mathrm{S}. \tag{11.8}$$

At the beginning of the sequence, the signal fractions are determined only by non-diffusion properties such as T_1 and T_2 relaxation. Both the fractions and the MD are at equilibrium (f_F^eq, f_S^eq, and MD^eq). At the first diffusion-encoding block (the 'filter block' with strength b_f), the action of the gradients induces an additional phase dispersion among spins within each component depending on its diffusivity. This results in greater signal attenuation of the fast component and perturbed signal fractions, according to (Åslund et al. 2009)

$$f_\mathrm{F/S}(t_m = 0) = f_\mathrm{F/S}^\mathrm{eq} \frac{\exp\big(-b_f D_\mathrm{F/S}\big)}{\exp(-b_f D_\mathrm{F}) + \exp(-b_f D_\mathrm{S})}, \tag{11.9}$$

as well as a reduction in the MD (Eq. 11.8). During the mixing time, diffusional exchange equilibrates the phase dispersion between the components and restores the signal fractions, according to (Callaghan et al. 2004)

$$f_\mathrm{F/S}(t_m) = f_\mathrm{F/S}^\mathrm{eq} - (f_\mathrm{F/S}^\mathrm{eq} - f'_\mathrm{F/S}(0))\exp(-k t_m), \tag{11.10}$$

where the effective exchange rate k is given by Eq. 11.1. The restoration of the fractions also restores the MD, according to

$$\mathrm{MD}(t_m) = \mathrm{MD}^\mathrm{eq} + \exp(-k t_m)[\mathrm{MD}(0) - \mathrm{MD}^\mathrm{eq}]. \tag{11.11}$$

To estimate the exchange rate, FEXI assumes that the strength (b) of the second diffusion-encoding block (the 'detection block') is in the low interval (Section 8.1) where the isotropic fourth-order phase cumulant (Eq. 6.26) has a near negligible contribution to the signal. This allows its resulting diffusion attenuation to be approximated as (Lasič et al. 2011)

$$A \approx \exp\big(-b\mathrm{MD}(t_m)\big). \tag{11.12}$$

Then, defining the 'filter efficiency' as $\sigma = 1 - \mathrm{MD}(0)/\mathrm{MD}^\mathrm{eq}$ and renaming k as AXR yields

$$\begin{aligned} \mathrm{MD}(t_m) &= \mathrm{MD}^\mathrm{eq}[1 - \sigma\exp(-\mathrm{AXR}\, t_m)], \text{and} \\ S &= S_0(t_m)\exp(-b_f \mathrm{MD}^\mathrm{eq} - b\mathrm{MD}(t_m)), \end{aligned} \tag{11.14}$$

where $S_0(t_m) = S_0\exp(-t_m/T_1)$ and T_1 is the voxel-average longitudinal relaxation time constant. FEXI estimates MD^eq, σ, AXR, and S_0 (for each t_m) by fitting Eq. 11.14 to powder-averaged data acquired with two or more different b, both with filtering ($b_f \neq 0$) at two or more t_m, and without filtering ($b_f = 0$).

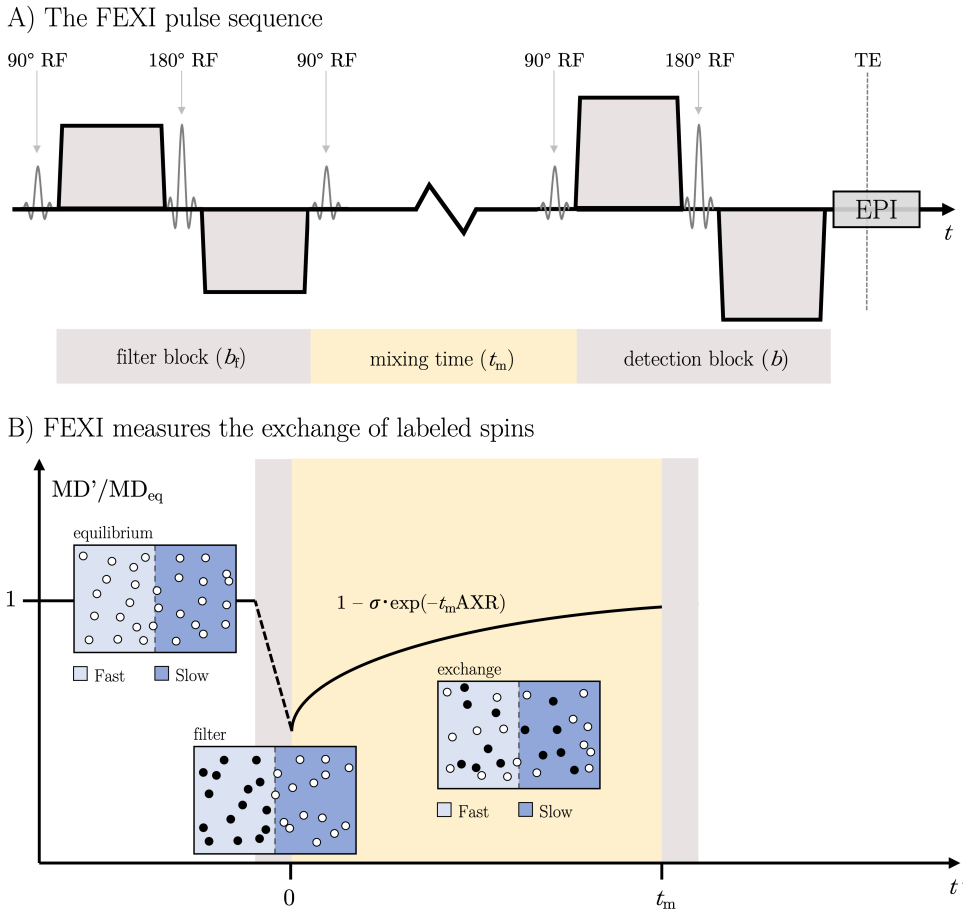

Figure 11.2 | A) The FEXI pulse sequence uses a DDE design with stimulated echoes. The first diffusion-encoding block with strength b_f is referred to as the 'filter block' and the second diffusion-encoding block with strength b is referred to as the 'detection block.' The second 90° RF pulse moves magnetization from the transversal plane to the longitudinal direction parallel to the field. There, during the mixing time (t_m), the signal undergoes T_1 but not T_2 relaxation. The third 90° RF pulse returns the magnetization to the transversal plane and induces a stimulated echo at TE where the signal is read-out using EPI. B) FEXI measures the exchange of labeled spins. At the beginning of the sequence, the signal fractions of spins with fast and slow diffusion are at equilibrium and MD = MD^{eq}. At the filter block, a higher phase dispersion is induced for among spins with fast diffusion. This perturbs the signal fractions and reduces the MD depending on the 'filter efficiency' (σ). During the mixing time, exchange equilibrates the spins that were 'labeled' with high phase dispersion at the filter block. This restores the signal fractions and the MD depending on the apparent exchange rate (AXR, Eq. 11.14). The AXR is then measured indirectly at the detection block by its effect of the MD. The figure (B) was adapted, with permission, from (Nilsson et al. 2013a), published by Wiley.

11.4 The impact of exchange on dMRI in normal brain

In Paper I, we used FEXI (Figure 11.2) to estimate the AXR (Eq. 11.14) in gray and white matter of 18 healthy volunteers (Figure 11.3A). The AXR maps were somewhat noisy but exhibited symmetry and anatomical structure. Here, a model selection map was obtained that indicated significant exchange across the whole brain. The average AXR values from the volunteers are shown in Figure 11.3B. AXR values were similar in gray and white matter, but lowest in the corpus callosum (0.3 s^{-1}) and highest in the anterior corona radiata (1.8 s^{-1}).

In Paper VI, we used SDE (Figure 6.1A) with multiple diffusion times to estimate the effective exchange rate (k, Eq. 11.7) in the brain of patients with subacute ischemic stroke (Figure 11.3C). The k maps appeared very noisy in the normal-appearing brain tissue outside the stroke lesions. Here, a model selection map was obtained that did not indicate

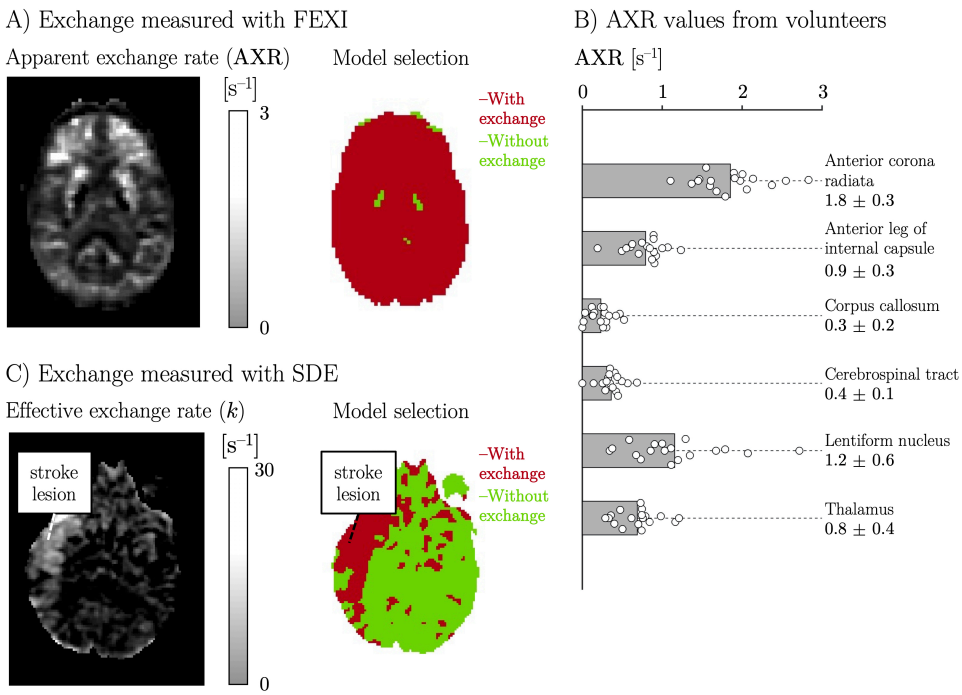

Figure 11.3 | A) Map of the apparent exchange rate (AXR) obtained using FEXI in a healthy volunteer from Paper I. The corresponding model selection map was calculated using the procedure described in Paper IV. The red voxels indicate where including AXR as a free parameter in Eq. 11.14 yielded a significantly better fit (with respect to an F-test) compared with fixing the AXR to zero. B) AXR values from each of the 18 healthy volunteers in six brain regions from Paper I together with means and inter-subject standard deviations. C) Map of the effective exchange rate (k) obtained using SDE with multiple diffusion times and Eq. 11.7 in a patient with subacute ischemic stroke. The model selection map indicated no significant exchange in normal-appearing brain tissue but fast exchange in the stroke lesion.

significant exchange in normal-appearing brain tissue, although the stroke lesion exhibited coherent regions with elevated exchange rates.

The $\mathbf{AXR}$ values estimated in white matter in Paper I (Figure 11.3B) were of similar magnitude as in those estimated in Nilsson et al. (2013a) (between 0.8 and 1.6 s^{-1}) and in Li et al. (2021) (between 1.5 and 2.9 s^{-1}). If the exchange occurs between intra- and extra-axonal spaces with approximately equal signal fractions (Section 3.2, discounting short T_2 myelin) and $\mathbf{AXR} \approx k$ in Eq. 11.1, then the estimated values correspond to intracellular exchange times (τ_i) between approximately 0.6 and 6 seconds. By the results in Figure 11.1, such exchange rates are safely in the slow regime and should have a negligible impact on the dMRI signal when using SDE with diffusion times below 60–600 ms. This may explain the low sensitivity to exchange when using SDE Paper VI (Figure 11.3C), using $T_d \in \{30\ 60\}$ ms, and the small effects observed in previous studies using SDE with T_d between 8 and 260 ms (Clark et al. 2000, Clark et al. 2001, Lätt et al. 2009, Nilsson et al. 2009). The exchange-weighting yielded by FEXI is on a somewhat longer timescale (Ning et al. 2018), however, and may detect such slow exchange (Figure 11.3A). Also, SDE with very long diffusion times have revealed exchange times at the shorter end of those detected with FEXI (0.6 s) (Nedjati-Gilani et al. 2017).

The $\mathbf{AXR}$ values estimated in gray matter in Paper I (Figure 11.3B) were of similar magnitude as in white matter and should thus be in the slow regime (Figure 11.1). However, previous studies using SDE with multiple diffusion times have indicated faster exchange in gray matter of the rat brain, with intracellular exchange times between 10 and 60 ms (Pfeuffer et al. 1998, Jelescu et al. 2021, Zhang et al. 2021). In the context of clinical dMRI, with T_d between 20 and 100 ms, such exchange is clearly in the intermediate regime where it affects the dMRI signal (Figure 11.1). Some estimates even approache the fast regime where exchange affects intra-component diffusivities, which could help in explaining the low microscopic anisotropy induced by dendrites (Chapter 10). The absence of fast exchange when using FEXI may reflect equilibration of fast-exchanging environments already during the filter block, leaving only slower-exchanging environments to be detected during the mixing time.

The slow diffusional exchange in white matter detected by FEXI may reflect exchange of water between the intra- and extra-axonal spaces associated with myelinated axons. Myelin appears to impede exchange (Nedjati-Gilani et al. 2017, Hill et al. 2021), wherefore intra-extra axonal exchange may preferentially occur across the nodes of Ranvier or through the myelin spirals (Figure 3.1B). Simulations of such exchange (Nilsson et al. 2010, Brusini et al. 2019) have yielded exchange rates that are consistent with the low $\mathbf{AXR}$ values observed in white matter in Paper I and in previous studies (Nilsson et al. 2013a, Li et al. 2021). The simulations also showed slower exchange rates for thicker myelin sheets (Brusini et al. 2019) and larger inter-nodal distances (Nilsson et al. 2010), wherefore the low AXR values in the

cerebrospinal tract and the corpus callosum could reflect larger axonal diameters (assuming similar g-ratios, Eq. 3.2) (Rushton 1951). That exchange in white matter is associated with axons is supported also by the finding of Li et al. (2021): that the AXR was anisotropic and higher in the direction perpendicular to fibers.

11.5 Clinical potential of exchange in intracranial tumors

In Paper I, we used FEXI to estimate the AXR in eleven brain tumors, comprising six meningiomas and five astrocytomas. The two tumor types appeared very differently in the AXR maps (Figure 11.4A). While the meningiomas were inconspicuous, the gliomas stood out as relatively bright against surrounding tissue. The exception was one outlier meningioma that was salient in the AXR map. The gliomas exhibited significantly higher AXR values compared with the meningiomas, excluding the outlier (Figure 11.4B).

The results suggested a relationship between diffusional exchange and tumor grade, both between and within different tumor types. The (malignant) grade II–IV gliomas generally exhibited higher AXR than the (benign) grade I meningiomas (Figure 11.4B). Among gliomas, the tumor with the highest grade (IV) exhibited the highest AXR. Among meningiomas, the outlier that exhibited an almost triple AXR was of intermediate grade (between I and II) and suspected to be invasive by the surgeon. A relationship between diffusional exchange and tumor aggressiveness has previously been indicated in breast cancer, both using FEXI in vitro (Lasič et al. 2016) and studying T_1 relaxation in mice (Ruggiero et al. 2018).

A higher level of diffusional exchange in higher-grade tumors could reflect an increased AQP expression that facilitates cell migration and metastasis (Saadoun et al. 2002, McCoy et al. 2007, Papadopoulos et al. 2008, Jung et al. 2011). A preliminary study in breast tumors also indicated a relationship between the AXR and AQP5 concentration (Shekar et al. 2021).

Diffusional exchange have potential clinical utility as a marker of tumor grade, which is key to the prognosis and management of gliomas (Louis et al. 2007). Another potential clinical utility of exchange is for evaluating tumor treatment response. MD is a marker of treatment response related to loss of cellularity due to treatment induced cell-kill and necrosis (Chenevert et al. 2000, Hamstra et al. 2005). MD is not affected until very high permeabilities (Figure 11.1), however, wherefore the AXR could be an even faster and more sensitive marker.

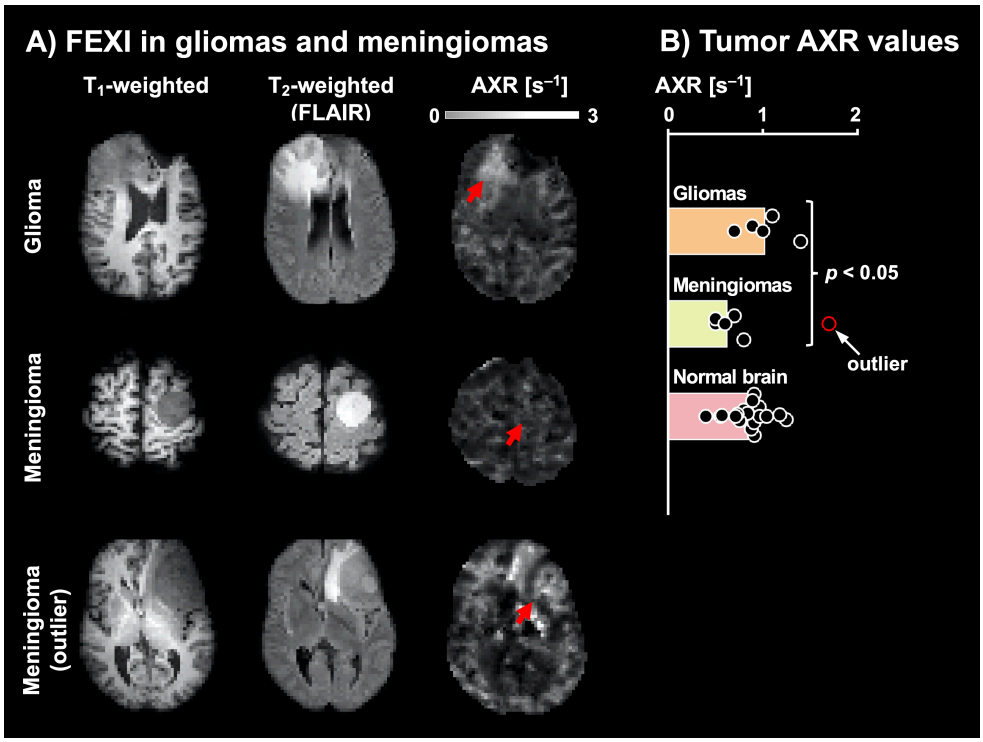

Figure 11.4 | FEXI in intracranial tumors from Paper I. A) Example AXR maps in one glioma, one meningioma and one outlier meningioma, together with T_1-weighted and T_2-weighted images. Both the gliomas and the meningiomas were hypointense on T_1-weighted images and hyperintense on T_2-weighted images. On the AXR maps, the gliomas were salient and relatively bright against the surrounding tissue, while the meningiomas were inconspicuous. One outlier meningioma exhibited very high AXR values. B) AXR values for the five gliomas, six meningiomas and 18 healthy volunteers (averaged across the six ROIs in Figure 11.3B and across test and retest data). The gliomas exhibited significantly higher AXR values compared with the meningiomas (1.0 ± 0.3 s^{-1} vs. 0.6 ± 0.1 s^{-1}, mean ± inter-subject SD, $p < 0.05$, two-sided t-test), excluding the outlier with AXR = 1.7 s^{-1}. For the normal brain, AXR = 0.8 ± 0.2 s^{-1}. The figure (A) was adapted, with permission, from Paper I by Lampinen et al. (2017), published by Wiley.

11.6 Clinical potential of exchange in ischemic stroke

In Paper VI, we used SDE (Figure 6.1A) with multiple diffusion times to obtain maps of the effective exchange rate (k, Eq. 11.14) in five ischemic stroke patients. Imaging was performed at the early and late subacute stage (on approximately day 2 and day 9, respectively) and at the chronic stage (on approximately day 100).

The stroke lesions were defined at the early subacute stage based on their associated reduction in MD (Figure 11.5A). The lesions exhibited a heterogeneous elevation in k both at the early and late subacute stage (Figure 11.5B), being bright in some regions (high k) but similar to normal-appearing tissue (low k) in other regions. The outcome of the lesions was heterogeneous by the chronic stage (Figure 11.5C), with a high MD indicating liquefaction of infarcted tissue in some regions but a near-normal MD indicating viable tissue in other regions.

Diffusional exchange at the subacute stage predicted tissue infarction by the chronic stage. There was a visual correspondence between the early patterns of elevated exchange and the late patterns of infarction (Figure 11.5B and C). Also, tissue that would be infarcted by the chronic stage exhibited significantly higher values of k compared with tissue that would remain viable, both on day two (9.5 ± 3.1 s^{-1} vs 3.6 ± 3.0 s^{-1}; mean $\pm$ SD, $p < 0.05$) and on day nine (7.2 ± 3.4 s^{-1} vs 3.6 ± 1.0 s^{-1}, $p < 0.05$). The MD values in lesions, however, were not predictive of outcome

Elevated rates of exchange in ischemic neural tissue has been demonstrated previously both in humans (Lätt et al. 2009) and in vitro (Yang et al. 2018). In Paper VI, we hypothesized that the association between ischemia and exchange reflects increased

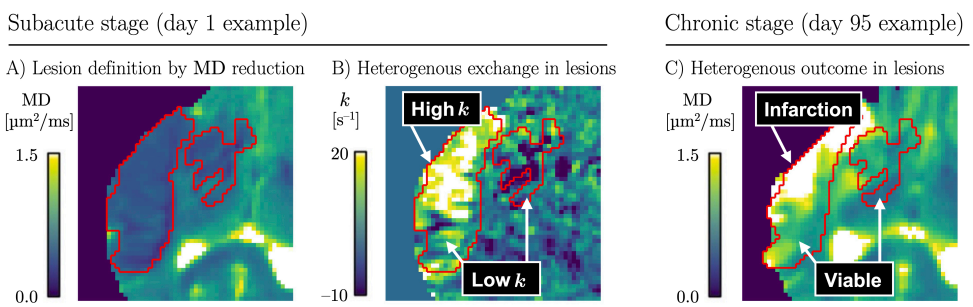

Figure 11.5 | Diffusional exchange in ischemic stroke from Paper VI. A) The lesions were defined in the subacute stage by their MD reduction. B) The effective exchange rate was heterogeneously elevated all lesions in the subacute stage, with a high k in some regions and a low k in other regions. C) The outcome of the lesions was heterogeneous by the chronic stage, with a high MD indicating infarction in some regions but a near-normal MD indicating viable tissue in other regions. The patterns of infarction by the chronic stage were similar to the patterns of exchange in the subacute stage, and tissue that would be infarcted exhibited significantly higher values of k. The figure was adapted, with permission, from Paper VI by Lampinen et al. (2021), published by Wiley.

membrane permeability of dead or dying cells. Ischemic cell death is thought to mainly involve necrosis (Buja et al. 1993) and is paralleled by an increased membrane permeability (O'Brien et al. 1997). In ischemic cardiomyocytes, membrane damage mechanisms include phospholipid depletion, oxidative stress, pore formation and unbalanced fatty acid metabolism (Buja et al. 1993, Weerasinghe et al. 2013). The process of excitotoxicity is another potential mechanism for the elevated exchange rates in ischemia, as it is dependent on the supposedly water-permeable VRAC (Nilius 2004b, Inoue et al. 2005, Mongin 2016).

A marker of necrosis and tissue damage in ischemic stroke may have clinical utility for deciding whether to perform revascularization outside the normal treatment time window, for example, in patients with wake-up stroke. Currently, a small volume of MD reduction is used to identify patients that have slow infarction progression and likely to benefit from such treatment. However, this may unnecessarily exclude patients, as MD reduction is unspecific for infarction (Paper VI) (Pierpaoli et al. 1996, Beaulieu et al. 1999, Ueda et al. 1999, Kidwell et al. 2000, Merino et al. 2007) and reflects reversible morphological changes (Hossmann 2006, Li et al. 2008, Baron et al. 2015) and possibly the loss of AQP4 from perivascular membranes (Frydenlund et al. 2006). As a marker of actual tissue damage, diffusional exchange may improve lesion characterization and enable the successful treatment of additional patients.

12 Conclusions

This thesis uses multidimensional dMRI to obtain additional information on human brain microstructure. In our work, we used tensor-valued diffusion encoding, diffusion-relaxation MRI, FEXI and SDE with multiple diffusion times to acquire data from normal brain tissue, white matter lesions, intracranial tumors, malformations of cortical development, and ischemic stroke.

We demonstrated that multidimensional dMRI data can remove model assumptions and that efficient acquisition protocols can be obtained using CRLB-based optimization. We applied the approach in vivo to remove all conventional assumptions on both diffusion and T_2 relaxation. This increased the number of free parameters from two to six or seven, depending on the specific context. By replacing assumptions with free parameters, the estimated parameters become less susceptible to bias and may represent tissue quantities across larger ranges of conditions.

We found that the domain of validity where the interpretation of microstructure model parameters can be trusted is small. Common assumptions were contradicted by independent data and resulted in parameter bias in normal brain, white matter lesions and intracranial tumors. Such bias prevented the 'stick' fraction from contemporary models to even compare different regions of normal brain and white matter lesions with respect to a tissue quantity like the neurite density.

We found that microscopic anisotropy in the brain reflects axons but not dendrites. One consequence is that microscopic anisotropy cannot be used to map neurites. Nevertheless, another consequence is that microscopic anisotropy may be a strong tool for tissue differentiation. As a primarily axon-based contrast, microscopic anisotropy may separate gray and white matter in conditions where alterations to myelin confounds conventional MRI contrasts such as T_1-weighted imaging.

We detected diffusional exchange with FEXI in normal brain, but at a rate that should have negligible impact on most dMRI acquisitions. In intracranial tumors, faster exchange was tentatively associated with higher histopathological grade. In ischemic stroke, fast exchange was predictive of infarction and may improve the definition of the ischemic core.

The conclusions of each individual publication were:

I. Optimization of the FEXI acquisition protocol allowed whole-brain estimation of the AXR in 13 minutes. Relevant AXR differences should be inferable between two populations for small group sizes. In vivo results showed slow exchange in the normal brain and in low-grade meningiomas but faster exchange in high-grade gliomas and in one meningioma of intermediate grade.

II. The assumptions of the NODDI model were contradicted by STE data and resulted in parameter bias in normal brain and in intracranial tumors. The CODIVIDE model uses joint analysis of LTE and STE data to remove assumptions from the NODDI model. This made it less susceptible to parameter bias and erroneous interpretations.

III. Microscopic diffusion anisotropy from tensor-valued diffusion encoding was associated with axons but not dendrites. Diffusion-relaxation MRI showed that the densities of microstructural components could not be estimated in the normal brain, and that T_2 relaxation may bias density estimates in white matter lesions. Contemporary microstructure models ranked the same regions of normal brain and white matter lesions differently with respect to the neurite density.

IV. Optimized diffusion-relaxation MRI with tensor-valued diffusion encoding removed all conventional assumptions on diffusion and T_2 relaxation from a two-component model and increased its number of free parameters from two to six. By removing the confounding effects of assumptions, the resulting parameters should be less susceptible to bias and represent tissue quantities across larger ranges of conditions. Independent parameter estimates contradicted assumptions of contemporary microstructure models. We found lower 'stick' fractions in children than in adults, and white matter lesions exhibited changes compatible with demyelination.

V. Microscopic anisotropy from tensor-valued diffusion encoding revealed white matter-like regions in malformations of cortical development that were gray matter-like in conventional MRI contrasts. We interpreted this as an indication of the presence of unmyelinated axons and that dendrites do not contribute to microscopic diffusion anisotropy. By reflecting axons rather than myelin or dendrites, microscopic diffusion anisotropy may differentiate gray and white matter in conditions where alterations to myelin confound conventional T_1- and T_2-weighted contrasts.

VI. Ischemic stroke lesions exhibited increased rates of diffusional exchange in the subacute stage. The rate of exchange was predictive of tissue infarction by the chronic stage, but the reduction in MD was not. Diffusional exchange may improve the definition of ischemic core and could allow selecting additional patients for late reperfusion therapy.

12.1 Future work

Future work will use multidimensional dMRI to remove additional assumptions and obtain model parameters with an even larger domain of validity. We will seek to extend the model in Paper IV (Table 7.1, Paper IV) to account for myelin water and myelin lipid (Figure 3.1B, Eq. 3.1). This would approach the estimation of true volume fractions in white matter and could enable the separation of demyelination from axonal loss. To sensitize the signal to myelin water, data can be acquired using a very short TE (Mackay et al. 1994, Whittall et al. 1997). To estimate the volume fraction of myelin lipid (v_{ML}), data can be acquired using multiple repetition times to account for T_1 relaxation and estimate proton density from the S_0 parameter. Preliminary results using this approach are presented in Figure 12.1, which shows a map of the myelin volume fraction ($v_{\mathrm{MW}} + v_{\mathrm{ML}}$, Eq. 3.1). Future work should also investigate the clinical utility of microscopic anisotropy for differentiating gray and white matter in myelin pathology (Figure 10.3), validate diffusional exchange as a marker of tumor grade (Figure 11.4), and explore the ability of diffusional exchange to improve the definition of ischemic core and identify additional patients for late revascularization (Figure 11.5).

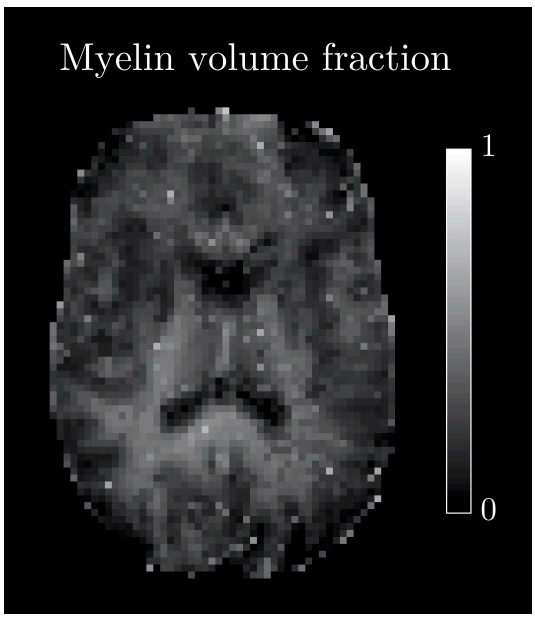

Figure 12.1 | Map of the myelin volume fraction in a healthy volunteer. The map was obtained by fitting a three-component model with free T_2 and T_1 values to dMRI data acquired using b between 0 and 4 $\mathrm{ms/\mu m^2}$ multiple shapes of the b-tensor, TE between 21 and 320 ms and repetition times between 2100 and 1400 ms The full acquisition took 30 minutes on a Siemens Prisma 3T system. The myelin water signal fraction was estimated based on the property of $T_2 = 15$ ms. The myelin lipid volume fraction was estimated by comparing the proton-density weighted S_0 parameter between tissue and CSF. The signal was corrected for receive- and transmit-field inhomogeneities using PrescanNormalize and tfl_b1map, respectively.

Acknowledgements

I first want to thank my main supervisor, Markus Nilsson. I owe this work to you. You taught me most of what I know about diffusion, writing and science. Most of the ideas were yours, especially the good ones. Your intelligence, dedication and friendship has made my PhD period a pleasant journey.

I also want to thank my co-supervisors. Freddy Ståhlberg, for the inclusive atmosphere in the MR physics group, for your interest in the work of junior colleagues, and for your help with finding my job position and navigating bureaucracy. Jimmy Lätt, for your trust when involving me in all kinds of projects. Linda Knutsson, for your dedication to the whole MR physics group and for your interest in my work.

Thank you also my co-authors. Your prior work and current contributions were essential to the final products. Special thanks to Filip Szczepankiewicz for your work with manuscripts and revisions, where your sharp sense for language and logical stringency has always mattered; and to C-F Westin and colleagues for your key theoretical work. Special thanks also to Pia Sundgren and Danielle van Westen for your dedication and willingness to pull strings and provide clinical data.

I want to thank my other past and current colleagues in the MR physics group, at Medical Radiation Physics and at associated institutions. Special thanks to Titti Owman, Boel Hansson and Ronnie Wirestam for being so welcoming and providing a sense of belonging. Special thanks also to André Ahlgren, Emelie Lindgren, Anna Rydhög, Renata Madru, Jan Brabec, Arthur Chakwizira and João de Almeida Martins for fun times during travel, on retreats and off work. Thank you, Karin Bryskhe, Daniel Topgaard, and Random Walk Imaging, for inviting and introducing me to so many people and places. Thank you Samo Lasič for friendly discussions.

Finally, I want to thank my family. My mother and father, for being the kindest and most supporting people I know. My parents in law, for all your help. My sisters and my children, Leon, Idun and Naia, for being yourselves. Lastly, the most important person of all, my beloved wife, Sara. Thank you for all your love and support that made the hard work possible.

Funding

This research was supported by:

- The Swedish Foundation for Strategic Research
  Grant AM13–0090

- The Swedish Cancer Society
  Grants CAN 2012/597 and CAN 2013/321

- The Swedish Research Council
  Grants K2011-52X-21737-01-3 and 2016-03443

- The Swedish Brain Foundation
  Grant FO2014-0133

- ALF
  Grant 2014/354

- Random Walk Imaging AB
  Grant MN15

- National Institutes of Health
  Grants R01MH074794, P41EB015902 and P41EB015898

- The Linnaeus Environment Thinking in Time: Cognition, Communication and Learning (via The Swedish Research Council)
  Grant 349-2007-869

- The Swedish Society for Medical Research
  Grant P15-0077

- BAGADILICO

- Stig and Ragna Gorthons Foundation

- Region Skåne

References

Agre P. Aquaporin water channels (Nobel lecture). *Angewandte Chemie International Edition*. 2004;43(33):4278-4290

Akita T, Okada Y. Characteristics and roles of the volume-sensitive outwardly rectifying (VSOR) anion channel in the central nervous system. *Neuroscience*. 2014;275(211-231

Albers GW. Expanding the window for thrombolytic therapy in acute stroke: the potential role of acute MRI for patient selection. *Stroke*. 1999;30(10):2230-2237

Alexander DC. A general framework for experiment design in diffusion MRI and its application in measuring direct tissue-microstructure features. *Magn Reson Med*. 2008;60(2):439-448

Alexander DC, Dyrby TB, Nilsson M, Zhang H. Imaging brain microstructure with diffusion MRI: practicality and applications. *NMR in Biomedicine*. 2019;32(4):e3841

Alexander DC, Hubbard PL, Hall MG, Moore EA, Ptito M, Parker GJ, Dyrby TB. Orientationally invariant indices of axon diameter and density from diffusion MRI. *Neuroimage*. 2010;52(4):1374-1389

Amiry-Moghaddam M, Ottersen OP. The molecular basis of water transport in the brain. *Nature Reviews Neuroscience*. 2003;4(12):991-1001

Åslund I, Nowacka A, Nilsson M, Topgaard D. Filter-exchange PGSE NMR determination of cell membrane permeability. *J Magn Reson*. 2009;200(2):291-295

Badaut J, Ashwal S, Adami A, Tone B, Recker R, Spagnoli D, Ternon B, Obenaus A. Brain water mobility decreases after astrocytic aquaporin-4 inhibition using RNA interference. *J Cereb Blood Flow Metab*. 2011;31(3):819-831

Baron CA, Kate M, Gioia L, Butcher K, Emery D, Budde M, Beaulieu CJS. Reduction of diffusion-weighted imaging contrast of acute ischemic stroke at short diffusion times. 2015;46(8):2136-2141

Basser PJ, Mattiello J, LeBihan D. MR diffusion tensor spectroscopy and imaging. *Biophysical journal*. 1994;66(1):259

Basser PJ, Pajevic S. A normal distribution for tensor-valued random variables: applications to diffusion tensor MRI. *IEEE transactions on medical imaging*. 2003;22(7):785-794

Basser PJ, Pajevic S. Spectral decomposition of a 4th-order covariance tensor: Applications to diffusion tensor MRI. *Signal Processing*. 2007;87(2):220-236

Beaulieu C. The basis of anisotropic water diffusion in the nervous system–a technical review. *NMR in Biomedicine*. 2002;15(7-8):435-455

Beaulieu C, Allen PS. Determinants of anisotropic water diffusion in nerves. *Magnetic resonance in medicine*. 1994a;31(4):394-400

Beaulieu C, Allen PS. Water diffusion in the giant axon of the squid: implications for diffusion-weighted MRI of the nervous system. *Magnetic Resonance in Medicine*. 1994b;32(5):579-583

Beaulieu C, De Crespigny A, Tong DC, Moseley ME, Albers GW, Marks MP. Longitudinal magnetic resonance imaging study of perfusion and diffusion in stroke: evolution of lesion volume and correlation with clinical outcome. *Ann Neurol*. 1999;46(4):568-578

Beaulieu C, Fenrich FR, Allen PS. Multicomponent water proton transverse relaxation and T2-discriminated water diffusion in myelinated and nonmyelinated nerve. *Magnetic resonance imaging*. 1998;16(10):1201-1210

Behrens TE, Woolrich MW, Jenkinson M, Johansen-Berg H, Nunes RG, Clare S, Matthews PM, Brady JM, Smith SM. Characterization and propagation of uncertainty in diffusion-weighted MR imaging. *Magnetic resonance in medicine*. 2003;50(5):1077-1088

Benjamini D, Basser P. Use of marginal distributions constrained optimization (MADCO) for accelerated 2D MRI relaxometry and diffusometry. *Journal of magnetic resonance*. 2016;271(40-45

Benjamini D, Basser PJ. Towards clinically feasible relaxation-diffusion correlation MRI using MADCO. 2018;269(93-96

Benjamini D, Basser PJ. Multidimensional correlation MRI. *NMR in Biomedicine*. 2020;33(12):e4226

Bennett M (2013). Virginia Woolf and Neuropsychiatry, Springer Netherlands.

Berger UV, Tsukaguchi H, Hediger M. Distribution of mRNA for the facilitated urea transporter UT3 in the rat nervous system. *Anatomy and embryology*. 1998;197(5):405-414

Bingham C. An antipodally symmetric distribution on the sphere. *The Annals of Statistics*. 1974;1201-1225

Birkl C, Doucette J, Fan M, Hernández-Torres E, Rauscher A. Myelin water imaging depends on white matter fiber orientation in the human brain. *Magnetic resonance in medicine*. 2021;85(4):2221-2231

Boss B, Stejskal E. Anisotropic diffusion in hydrated vermiculite. *The Journal of Chemical Physics*. 1965;43(3):1068-1069

Braitenberg V, Schüz A (2013). Cortex: statistics and geometry of neuronal connectivity, Springer Science & Business Media.

Brusini L, Menegaz G, Nilsson M. Monte Carlo simulations of water exchange through myelin wraps: Implications for diffusion MRI. *IEEE transactions on medical imaging*. 2019;38(6):1438-1445

Buja L, Eigenbrodt ML, Eigenbrodt EH. Apoptosis and necrosis. Basic types and mechanisms of cell death. *Archives of pathology & laboratory medicine*. 1993;117(12):1208-1214

Callaghan P, Jolley K, Lelievre J. Diffusion of water in the endosperm tissue of wheat grains as studied by pulsed field gradient nuclear magnetic resonance. *Biophysical journal*. 1979;28(1):133-141

Callaghan PT, Furo I. Diffusion-diffusion correlation and exchange as a signature for local order and dynamics. *J Chem Phys*. 2004;120(8):4032-4038

Caverzasi E, Papinutto N, Castellano A, Zhu AH, Scifo P, Riva M, Bello L, Falini A, Bharatha A, Henry RG. Neurite orientation dispersion and density imaging color maps to characterize brain diffusion in neurologic disorders. *Journal of Neuroimaging*. 2016;26(5):494-498

Cercignani M, Alexander DC. Optimal acquisition schemes for in vivo quantitative magnetization transfer MRI. *Magn Reson Med*. 2006;56(4):803-810

Chenevert TL, Brunberg JA, Pipe JG. Anisotropic diffusion in human white matter: demonstration with MR techniques in vivo. *Radiology*. 1990;177(2):401-405

Chenevert TL, Stegman LD, Taylor JM, Robertson PL, Greenberg HS, Rehemtulla A, Ross BD. Diffusion magnetic resonance imaging: an early surrogate marker of therapeutic efficacy in brain tumors. *Journal of the National Cancer Institute*. 2000;92(24):2029-2036

Chklovskii DB, Schikorski T, Stevens CF. Wiring optimization in cortical circuits. *Neuron*. 2002;34(3):341-347

Clark CA, Hedehus M, Moseley ME. Diffusion time dependence of the apparent diffusion tensor in healthy human brain and white matter disease. *Magnetic resonance in medicine*. 2001;45(6):1126-1129

Clark CA, Le Bihan D. Water diffusion compartmentation and anisotropy at high b values in the human brain. *Magnetic Resonance in Medicine*. 2000;44(6):852-859

Clark DL, Boutros NN, Mendez MF (2010). The brain and behavior: an introduction to behavioral neuroanatomy, Cambridge university press.

Coelho S, Pozo JM, Costantini M, Highley JR, Mozumder M, Simpson JE, Ince PG, Frangi AF. Local volume fraction distributions of axons, astrocytes, and myelin in deep subcortical white matter. *NeuroImage*. 2018;179(275-287

Coelho S, Pozo JM, Jespersen SN, Frangi AFJapa. Optimal experimental design for biophysical modelling in multidimensional diffusion MRI. 2019a;

Coelho S, Pozo JM, Jespersen SN, Jones DK, Frangi AF. Resolving degeneracy in diffusion MRI biophysical model parameter estimation using double diffusion encoding. *Mag Reson Med*. 2019b;82(1):395-410

Colgan N, Siow B, O'Callaghan JM, Harrison IF, Wells JA, Holmes HE, Ismail O, Richardson S, Alexander DC, Collins EC. Application of neurite orientation dispersion and density imaging (NODDI) to a tau pathology model of Alzheimer's disease. *Neuroimage*. 2016;125(739-744

Collorone S, Cawley N, Grussu F, Prados F, Tona F, Calvi A, Kanber B, Schneider T, Kipp L, Zhang H. Reduced neurite density in the brain and cervical spinal cord in relapsing–remitting multiple sclerosis: A NODDI study. *Multiple Sclerosis Journal*. 2020;26(13):1647-1657

Colombo N, Salamon N, Raybaud C, Özkara Ç, Barkovich AJJED. Imaging of malformations of cortical development. 2009;11(3):194-205

Comon P. Tensors: a brief introduction. *IEEE Signal Processing Magazine*. 2014;31(3):44-53

Cory D, Garroway A, Miller J. Applications of spin transport as a probe of local geometry

Cramér H (1946). Mathematical methods of statistics, Princeton university press.

Criste G, Trapp B, Dutta R. Axonal loss in multiple sclerosis: causes and mechanisms. *Handbook of clinical neurology*. 2014;122(101-113

Cullen NC, Zetterberg H, Insel PS, Olsson B, Andreasson U, Initiative AsDN, Blennow K, Hansson O, Mattsson-Carlgren N. Comparing progression biomarkers in clinical trials of early Alzheimer's disease. *Annals of Clinical and Translational Neurology*. 2020;7(9):1661-1673

de Almeida Martins JP, Topgaard D. Multidimensional correlation of nuclear relaxation rates and diffusion tensors for model-free investigations of heterogeneous anisotropic porous materials. *Scientific reports*. 2018;8(1):2488

De Santis S, Barazany D, Jones DK, Assaf Y. Resolving relaxometry and diffusion properties within the same voxel in the presence of crossing fibres by combining inversion recovery and diffusion-weighted acquisitions. *Magnetic resonance in medicine*. 2016;75(1):372-380

Dhital B, Reisert M, Kellner E, Kiselev VG. Intra-axonal diffusivity in brain white matter. *Neuroimage*. 2019;189(543-550

Does MD, Gore JCJMrim. Compartmental study of diffusion and relaxation measured in vivo in normal and ischemic rat brain and trigeminal nerve. 2000;43(6):837-844

Dortch RD, Harkins KD, Juttukonda MR, Gore JC, Does MD. Characterizing inter-compartmental water exchange in myelinated tissue using relaxation exchange spectroscopy. *Mag Reson Med*. 2013;70(5):1450-1459

Driscoll JR, Healy DM. Computing Fourier transforms and convolutions on the 2-sphere. *Advances in applied mathematics*. 1994;15(2):202-250

Duncan JS, Winston GP, Koepp MJ, Ourselin SJTLN. Brain imaging in the assessment for epilepsy surgery. 2016;15(4):420-433

Edgar JM, Griffiths IR (2009). White matter structure: a microscopist's view. Diffusion MRI, Elsevier**:** 74-103.

Einstein A. On the motion of small particles suspended in liquids at rest required by the molecular-kinetic theory of heat. *Annalen der physik*. 1905;17(549-560):208

Englund E, Brun A. White matter changes in dementia of Alzheimer's type: the difference in vulnerability between cell compartments. *Histopathology*. 1990;16(5):433-439

Englund E, Brun A, Persson B. Correlations between histopathologic white matter changes and proton MR relaxation times in dementia. *Alzheimer disease and associated disorders*. 1987;1(3):156-170

Eriksson S, Lasič S, Nilsson M, Westin C-F, Topgaard D. NMR diffusion-encoding with axial symmetry and variable anisotropy: Distinguishing between prolate and oblate microscopic diffusion tensors with unknown orientation distribution. *The Journal of chemical physics*. 2015;142(10):104201

Eriksson S, Lasic S, Topgaard D. Isotropic diffusion weighting in PGSE NMR by magic-angle spinning of the q-vector. *Journal of Magnetic Resonance*. 2013;226(13-18

Falangola MF, Guilfoyle DN, Tabesh A, Hui ES, Nie X, Jensen JH, Gerum SV, Hu C, LaFrancois J, Collins HR. Histological correlation of diffusional kurtosis and white matter modeling metrics in cuprizone-induced corpus callosum demyelination. *NMR in Biomedicine*. 2014;27(8):948-957

Fieremans E, Jensen JH, Helpern JA. White matter characterization with diffusional kurtosis imaging. *Neuroimage*. 2011;58(1):177-188

Frydenlund DS, Bhardwaj A, Otsuka T, Mylonakou MN, Yasumura T, Davidson KG, Zeynalov E, Skare Ø, Laake P, Haug F-M. Temporary loss of perivascular

aquaporin-4 in neocortex after transient middle cerebral artery occlusion in mice. *Proceedings of the National Academy of Sciences*. 2006;103(36):13532-13536

Goveas J, O'Dwyer L, Mascalchi M, Cosottini M, Diciotti S, De Santis S, Passamonti L, Tessa C, Toschi N, Giannelli M. Diffusion-MRI in neurodegenerative disorders. *Magnetic resonance imaging*. 2015;33(7):853-876

Guerrini R, Dobyns WB, Barkovich AJ. Abnormal development of the human cerebral cortex: genetics, functional consequences and treatment options. *Trends in neurosciences*. 2008;31(3):154-162

Hamstra DA, Chenevert TL, Moffat BA, Johnson TD, Meyer CR, Mukherji SK, Quint DJ, Gebarski SS, Fan X, Tsien CI. Evaluation of the functional diffusion map as an early biomarker of time-to-progression and overall survival in high-grade glioma. *Proceedings of the National Academy of Sciences of the United States of America*. 2005;102(46):16759-16764

Harkins KD, Galons JP, Secomb TW, Trouard TP. Assessment of the effects of cellular tissue properties on ADC measurements by numerical simulation of water diffusion. *Magnetic Resonance in Medicine*. 2009;62(6):1414-1422

Henriques RN, Jespersen SN, Shemesh N. Correlation tensor magnetic resonance imaging. *Neuroimage*. 2020;211(116605

Hildebrand C, Remahl S, Persson H, Bjartmar C. Myelinated nerve fibres in the CNS. *Progress in neurobiology*. 1993;40(3):319-384

Hill I, Palombo M, Santin M, Branzoli F, Philippe A-C, Wassermann D, Aigrot M-S, Stankoff B, Baron-van Evercooren A, Felfli M. Machine learning based white matter models with permeability: An experimental study in cuprizone treated in-vivo mouse model of axonal demyelination. *NeuroImage*. 2021;224(117425

Holland BA, Haas DK, Norman D, Brant-Zawadzki M, Newton TH. MRI of normal brain maturation. *American Journal of Neuroradiology*. 1986;7(2):201-208

Horsfield MA, Jones DK. Applications of diffusion-weighted and diffusion tensor MRI to white matter diseases–a review. *NMR in Biomedicine*. 2002;15(7-8):570-577

Hossmann K-A. Pathophysiology and therapy of experimental stroke. *Cellular and molecular neurobiology*. 2006;26(7-8):1055-1081

Hutter J, Slator PJ, Christiaens D, Teixeira RPA, Roberts T, Jackson L, Price AN, Malik S, Hajnal JV. Integrated and efficient diffusion-relaxometry using ZEBRA. *Scientific reports*. 2018;8(1):1-13

Ianuş A, Jespersen SN, Duarte TS, Alexander DC, Drobnjak I, Shemesh N. Accurate estimation of microscopic diffusion anisotropy and its time dependence in the mouse brain. *Neuroimage*. 2018;183(934-949

Ikari K, Hayashi M. Aging in the Neuropil of Cerebral Cortex–A Quantitative Ultrastructural Study. *Psychiatry and Clinical Neurosciences*. 1981;35(4):477-486

Iliff JJ, Wang M, Liao Y, Plogg BA, Peng W, Gundersen GA, Benveniste H, Vates GE, Deane R, Goldman SA. A paravascular pathway facilitates CSF flow through the brain parenchyma and the clearance of interstitial solutes, including amyloid β. *Science translational medicine*. 2012;4(147):147ra111-147ra111

Inoue H, Mori Si, Morishima S, Okada Y. Volume-sensitive chloride channels in mouse cortical neurons: characterization and role in volume regulation. *European Journal of Neuroscience*. 2005;21(6):1648-1658

Jelescu IO, de Skowronski A, Palombo M, Novikov DS. Neurite Exchange Imaging (NEXI): A minimal model of diffusion in gray matter with inter-compartment water exchange. *arXiv preprint arXiv:2108.06121*. 2021;

Jelescu IO, Palombo M, Bagnato F, Schilling KG. Challenges for biophysical modeling of microstructure. *Journal of Neuroscience Methods*. 2020;108861

Jelescu IO, Veraart J, Fieremans E, Novikov DS. Degeneracy in model parameter estimation for multi-compartmental diffusion in neuronal tissue. *NMR in Biomedicine*. 2016a;29(1):33-47

Jelescu IO, Zurek M, Winters KV, Veraart J, Rajaratnam A, Kim NS, Babb JS, Shepherd TM, Novikov DS, Kim SG. In vivo quantification of demyelination and recovery using compartment-specific diffusion MRI metrics validated by electron microscopy. *Neuroimage*. 2016b;132(104-114

Jensen JH, Helpern JA, Ramani A, Lu H, Kaczynski K. Diffusional kurtosis imaging: The quantification of non-gaussian water diffusion by means of magnetic resonance imaging. *Magnetic Resonance in Medicine*. 2005;53(6):1432-1440

Jespersen SN, Bjarkam CR, Nyengaard JR, Chakravarty MM, Hansen B, Vosegaard T, Østergaard L, Yablonskiy D, Nielsen NC, Vestergaard-Poulsen P. Neurite density from magnetic resonance diffusion measurements at ultrahigh field: comparison with light microscopy and electron microscopy. *Neuroimage*. 2010;49(1):205-216

Jespersen SN, Kroenke CD, Østergaard L, Ackerman JJ, Yablonskiy DA. Modeling dendrite density from magnetic resonance diffusion measurements. *Neuroimage*. 2007;34(4):1473-1486

Jespersen SN, Lundell H, Sønderby CK, Dyrby TB. Orientationally invariant metrics of apparent compartment eccentricity from double pulsed field gradient diffusion experiments. *NMR in Biomedicine*. 2013;26(12):1647-1662

Jian B, Vemuri BC, Özarslan E, Carney PR, Mareci TH. A novel tensor distribution model for the diffusion-weighted MR signal. *NeuroImage*. 2007;37(1):164-176

Jones DK, Basser PJ. "Squashing peanuts and smashing pumpkins": how noise distorts diffusion-weighted MR data. *Magnetic Resonance in Medicine: An Official Journal of the International Society for Magnetic Resonance in Medicine*. 2004;52(5):979-993

Jung HJ, Park J-Y, Jeon H-S, Kwon T-H. Aquaporin-5: a marker protein for proliferation and migration of human breast cancer cells. *PloS one*. 2011;6(12):e28492

Kaden E, Kelm ND, Carson RP, Does MD, Alexander DC. Multi-compartment microscopic diffusion imaging. *NeuroImage*. 2016;139(346-359

Kaden E, Kruggel F, Alexander DC. Quantitative mapping of the per-axon diffusion coefficients in brain white matter. *Magnetic resonance in medicine*. 2015;

Kärger J. NMR self-diffusion studies in heterogeneous systems. *Advances in Colloid and Interface Science*. 1985;23(129-148

Kasthuri N, Hayworth KJ, Berger DR, Schalek RL, Conchello JA, Knowles-Barley S, Lee D, Vázquez-Reina A, Kaynig V, Jones TR. Saturated reconstruction of a volume of neocortex. *Cell*. 2015;162(3):648-661

Kidwell CS, Saver JL, Mattiello J, Starkman S, Vinuela F, Duckwiler G, Gobin YP, Jahan R, Vespa P, Kalafut M. Thrombolytic reversal of acute human cerebral ischemic

injury shown by diffusion/perfusion magnetic resonance imaging. *Ann Neurol*. 2000;47(4):462-469

King LS, Kozono D, Agre P. From structure to disease: the evolving tale of aquaporin biology. *Nature reviews Molecular cell biology*. 2004;5(9):687-698

Kiselev VG. The cumulant expansion: an overarching mathematical framework for understanding diffusion NMR. *Diffusion MRI*. 2010;152-168

Kiselev VG, Il'yasov KA. Is the "biexponential diffusion" biexponential? *Magnetic resonance in medicine*. 2007;57(3):464-469

Knight MJ, Dillon S, Jarutyte L, Kauppinen RA. Magnetic resonance relaxation anisotropy: Physical principles and uses in microstructure imaging. *Biophysical journal*. 2017;112(7):1517-1528

Kollo T (2005). Advanced multivariate statistics with matrices, Springer.

Kroenke CD, Ackerman JJ, Yablonskiy DA. On the nature of the NAA diffusion attenuated MR signal in the central nervous system. *Magnetic resonance in medicine*. 2004;52(5):1052-1059

Lasič S, Nilsson M, Latt J, Stahlberg F, Topgaard D. Apparent exchange rate mapping with diffusion MRI. *Magn Reson Med*. 2011;66(2):356-365

Lasič S, Oredsson S, Partridge SC, Saal LH, Topgaard D, Nilsson M, Bryskhe K. Apparent exchange rate for breast cancer characterization. *NMR in Biomed*. 2016;29(5):631-639

Lasič S, Szczepankiewicz F, Eriksson S, Nilsson M, Topgaard D. Microanisotropy imaging: quantification of microscopic diffusion anisotropy and orientational order parameter by diffusion MRI with magic-angle spinning of the q-vector. *Frontiers in Physics*. 2014;2(11

Lätt J, Nilsson M, van Westen D, Wirestam R, Ståhlberg F, Brockstedt S. Diffusion-weighted MRI measurements on stroke patients reveal water-exchange mechanisms in sub-acute ischaemic lesions. *NMR in Biomedicine*. 2009;22(6):619-628

Lawrenz M, Finsterbusch J. Double-wave-vector diffusion-weighted imaging reveals microscopic diffusion anisotropy in the living human brain. *Magnetic resonance in medicine*. 2013;69(4):1072-1082

Lawrenz M, Finsterbusch J. Detection of microscopic diffusion anisotropy in human cortical gray matter in vivo with double diffusion encoding. *Magnetic resonance in medicine*. 2018;81(2):1296-1306

Le Bihan D. Looking into the functional architecture of the brain with diffusion MRI. *Nat Rev Neurosci*. 2003;4(6):469-480

Le Bihan D, Breton E, Lallemand D, Grenier P, Cabanis E, Laval-Jeantet M. MR imaging of intravoxel incoherent motions: application to diffusion and perfusion in neurologic disorders. *Radiology*. 1986;161(2):401-407

Lebel C, Walker L, Leemans A, Phillips L, Beaulieu C. Microstructural maturation of the human brain from childhood to adulthood. *Neuroimage*. 2008;40(3):1044-1055

Lee H-H, Papaioannou A, Kim S-L, Novikov DS, Fieremans E. Probing axonal swelling with time dependent diffusion MRI. *arXiv preprint: 12685*. 2019;

Lee H-H, Papaioannou A, Novikov DS, Fieremans E. In vivo observation and biophysical interpretation of time-dependent diffusion in human cortical gray matter. *NeuroImage*. 2020;222(117054

Leenders K, Perani D, Lammertsma A, Heather J, Buckingham P, Jones T, Healy M, Gibbs J, Wise R, Hatazawa J. Cerebral blood flow, blood volume and oxygen utilization: normal values and effect of age. *Brain*. 1990;113(1):27-47

Li P, Murphy TH. Two-photon imaging during prolonged middle cerebral artery occlusion in mice reveals recovery of dendritic structure after reperfusion. *Journal of Neuroscience*. 2008;28(46):11970-11979

Li Z, Hsu Y-C, Bai R. Characterization of Apparent Exchange Rate in Human Brain White Matter. In Proceedings of the ISMRM Virtual Conference, 2021, p 0205. 2021;

Löbel U, Sedlacik J, Güllmar D, Kaiser WA, Reichenbach JR, Mentzel H-J. Diffusion tensor imaging: the normal evolution of ADC, RA, FA, and eigenvalues studied in multiple anatomical regions of the brain. *Neuroradiology*. 2009;51(4):253-263

Louis DN, Ohgaki H, Wiestler OD, Cavenee WK, Burger PC, Jouvet A, Scheithauer BW, Kleihues P. The 2007 WHO classification of tumours of the central nervous system. *Acta neuropathologica*. 2007;114(2):97-109

Mackay A, Whittall K, Adler J, Li D, Paty D, Graeb D. In vivo visualization of myelin water in brain by magnetic resonance. *Magnetic Resonance in Medicine*. 1994;31(6):673-677

Mardia KV, Jupp PE (2009). Directional statistics, John Wiley & Sons.

McCaslin AF, Chen BR, Radosevich AJ, Cauli B, Hillman EM. In vivo 3D morphology of astrocyte—vasculature interactions in the somatosensory cortex: implications for neurovascular coupling. *Journal of cerebral blood flow & metabolism*. 2011;31(3):795-806

McCoy E, Sontheimer H. Expression and function of water channels (aquaporins) in migrating malignant astrocytes. *Glia*. 2007;55(10):1034-1043

McKinnon ET, Jensen JH. Measuring intra-axonal T2 in white matter with direction-averaged diffusion MRI. *Mag Reson Med*. 2019;81(5):2985-2994

McKinnon ET, Jensen JH, Glenn GR, Helpern JA. Dependence on b-value of the direction-averaged diffusion-weighted imaging signal in brain. *Magnetic resonance imaging*. 2017;36(121-127

Merino JG, Latour LL, Todd JW, Luby M, Schellinger PD, Kang D-W, Warach S. Lesion volume change after treatment with tissue plasminogen activator can discriminate clinical responders from nonresponders. *Stroke*. 2007;38(11):2919-2923

Mills R. Self-diffusion in normal and heavy water in the range 1-45. deg. *The Journal of Physical Chemistry*. 1973;77(5):685-688

Minati L, Węglarz WP. Physical foundations, models, and methods of diffusion magnetic resonance imaging of the brain: A review. *Concepts in Magnetic Resonance Part A: An Educational Journal*. 2007;30(5):278-307

Mitra PP. Multiple wave-vector extensions of the NMR pulsed-field-gradient spin-echo diffusion measurement. *Physical Review B*. 1995;51(21):15074

Mongin AAJPA-EJoP. Volume-regulated anion channel—a frenemy within the brain. 2016;468(3):421-441

Mori S, Crain BJ, Chacko VP, Van Zijl PC. Three-dimensional tracking of axonal projections in the brain by magnetic resonance imaging. *Annals of Neurology: Official Journal of the American Neurological Association and the Child Neurology Society*. 1999;45(2):265-269

Mori S, Van Zijl PC. Diffusion weighting by the trace of the diffusion tensor within a single scan. *Magnetic resonance in medicine*. 1995;33(1):41-52

Moseley M, Cohen Y, Mintorovitch J, Chileuitt L, Shimizu H, Kucharczyk J, Wendland M, Weinstein P. Early detection of regional cerebral ischemia in cats: comparison of diffusion-and T2-weighted MRI and spectroscopy. *Magnetic resonance in medicine*. 1990;14(2):330-346

Moseley ME, Kucharczyk J, Asgari HS, Norman D. Anisotropy in diffusion-weighted MRI. *Magnetic Resonance in Medicine*. 1991;19(2):321-326

Natu VS, Gomez J, Barnett M, Jeska B, Kirilina E, Jaeger C, Zhen Z, Cox S, Weiner KS, Weiskopf N. Apparent thinning of human visual cortex during childhood is associated with myelination. *Proceedings of the National Academy of Sciences*. 2019;116(41):20750-20759

Nedjati-Gilani GL, Schneider T, Hall MG, Cawley N, Hill I, Ciccarelli O, Drobnjak I, Wheeler-Kingshott CAG, Alexander DC. Machine learning based compartment models with permeability for white matter microstructure imaging. *NeuroImage*. 2017;150(119-135

Nilius B. Is the volume-regulated anion channel VRAC a "water-permeable" channel? *Neorochem Res*. 2004a;29(1):3-8

Nilius BJNr. Is the volume-regulated anion channel VRAC a "water-permeable" channel? 2004b;29(1):3-8

Nilsson M, Hagslätt H, Van Westen D, Wirestam R, Ståhlberg F, Lätt J. A mechanism for exchange between intraaxonal and extracellular water: Permeable nodes of Ranvier. In Proceedings of the 18th Annual Meeting of ISMRM, Stockholm, Sweden, 2010, p 1570. 2010;

Nilsson M, Lätt J, Nordh E, Wirestam R, Ståhlberg F, Brockstedt S. On the effects of a varied diffusion time in vivo: is the diffusion in white matter restricted? *Magnetic resonance imaging*. 2009;27(2):176-187

Nilsson M, Lätt J, van Westen D, Brockstedt S, Lasič S, Stahlberg F, Topgaard D. Noninvasive mapping of water diffusional exchange in the human brain using filter-exchange imaging. *Magn Reson Med*. 2013a;69(6):1573-1581

Nilsson M, van Westen D, Ståhlberg F, Sundgren PC, Lätt J. The role of tissue microstructure and water exchange in biophysical modelling of diffusion in white matter. *MAGMA*. 2013b;26(4):345-370

Ning L, Gagoski B, Szczepankiewicz F, Westin C-F, Rathi YJb. Joint RElaxation-Diffusion Imaging Moments (REDIM) to probe neurite microstructure. *IEEE Trans Med Imaging*. 2019;

Ning L, Nilsson M, Lasič S, Westin C-F, Rathi YJTJocp. Cumulant expansions for measuring water exchange using diffusion MRI. 2018;148(7):074109

Ning L, Szczepankiewicz F, Nilsson M, Rathi Y, Westin C-F. Probing tissue microstructure by diffusion skewness tensor imaging. *Scientific Reports*. 2021;11(1):1-10

Novikov DS, Kiselev VG, Jespersen SN. On modeling. *Magnetic resonance in medicine*. 2018a;

Novikov DS, Veraart J, Jelescu IO, Fieremans E. Rotationally-invariant mapping of scalar and orientational metrics of neuronal microstructure with diffusion MRI. *NeuroImage*. 2018b;174(518-538

O'Brien JS, Sampson EL. Lipid composition of the normal human brain: gray matter, white matter, and myelin. *Journal of lipid research*. 1965;6(4):537-544

O'Brien MC, Healy Jr SF, Raney SR, Hurst JM, Avner B, Hanly A, Mies C, Freeman JW, Snow C, Koester SK. Discrimination of late apoptotic/necrotic cells (type III) by flow cytometry in solid tumors. *Cytom Part A*. 1997;28(1):81-89

Ogami A, Miyazaki H, Niisato N, Sugimoto T, Marunaka Y. UT-B1 urea transporter plays a noble role as active water transporter in C6 glial cells. *Biochemical and biophysical research communications*. 2006;351(3):619-624

Olesen JL, Østergaard L, Shemesh N, Jespersen SN. Diffusion time dependence, power-law scaling, and exchange in gray matter. *arXiv preprint arXiv:2108.09983*. 2021;

Oshio K, Watanabe H, Song Y, Verkman A, Manley GT. Reduced cerebrospinal fluid production and intracranial pressure in mice lacking choroid plexus water channel Aquaporin-1. *The FASEB journal*. 2005;19(1):76-78

Özarslan E. Compartment shape anisotropy (CSA) revealed by double pulsed field gradient MR. *Journal of Magnetic Resonance*. 2009;199(1):56-67

Papadopoulos M, Saadoun S, Verkman A. Aquaporins and cell migration. *Pflugers Arch*. 2008;456(4):693-700

Papadopoulos MC, Verkman AS. Aquaporin-4 and brain edema. *Pediatric nephrology*. 2007;22(6):778-784

Pasternak O, Sochen N, Gur Y, Intrator N, Assaf Y. Free water elimination and mapping from diffusion MRI. *Mag Reson Med*. 2009;62(3):717-730

Perge JA, Koch K, Miller R, Sterling P, Balasubramanian V. How the optic nerve allocates space, energy capacity, and information. *Journal of Neuroscience*. 2009;29(24):7917-7928

Pfeuffer J, Flögel U, Dreher W, Leibfritz D. Restricted diffusion and exchange of intracellular water: theoretical modelling and diffusion time dependence of 1H NMR measurements on perfused glial cells. *NMR in Biomedicine: An International Journal Devoted to the Development and Application of Magnetic Resonance In Vivo*. 1998;11(1):19-31

Pierpaoli C, Alger JR, Righini A, Mattiello J, Dickerson R, Pres DD, Barnett A, Chiro GD. High temporal resolution diffusion MRI of global cerebral ischemia and reperfusion. *Journal of Cerebral Blood Flow & Metabolism*. 1996;16(5):892-905

Plewes DB, Kucharczyk W. Physics of MRI: a primer. *Journal of magnetic resonance imaging*. 2012;35(5):1038-1054

Rao CR. Information and accuracy attainable in the estimation of statistical parameters. *Bulletin of the Calcutta Mathematical Society*. 1945;37(3):81-91

Reisert M, Kiselev VG, Dhital B. A unique analytical solution of the white matter standard model using linear and planar encodings. *Mag Reson Med*. 2019;81(6):3819-3825

Reuss L (2012). Water Transport Across Cell Membranes. eLS, John Wiley & Sons, Ltd.

Romano A, D'andrea G, Minniti G, Mastronardi L, Ferrante L, Fantozzi L, Bozzao A. Pre-surgical planning and MR-tractography utility in brain tumour resection. *European radiology*. 2009;19(12):2798-2808

Ruggiero MR, Baroni S, Pezzana S, Ferrante G, Geninatti Crich S, Aime S. Evidence for the role of intracellular water lifetime as a tumour biomarker obtained by in vivo field-cycling relaxometry. *Angewandte Chemie*. 2018;130(25):7590-7594

Rushton W. A theory of the effects of fibre size in medullated nerve. *The Journal of physiology*. 1951;115(1):101-122

Saadoun S, Papadopoulos M, Davies D, Krishna S, Bell B. Aquaporin-4 expression is increased in oedematous human brain tumours. *Journal of Neurology, Neurosurgery & Psychiatry*. 2002;72(2):262-265

Sagi Y, Tavor I, Hofstetter S, Tzur-Moryosef S, Blumenfeld-Katzir T, Assaf Y. Learning in the fast lane: new insights into neuroplasticity. *Neuron*. 2012;73(6):1195-1203

Scholz J, Klein MC, Behrens TE, Johansen-Berg H. Training induces changes in white-matter architecture. *Nature neuroscience*. 2009;12(11):1370

Schüz A, Palm G. Density of neurons and synapses in the cerebral cortex of the mouse. *Journal of Comparative Neurology*. 1989;286(4):442-455

Sepehrband F, Cabeen RP, Choupan J, Barisano G, Law M, Toga AW, Initiative AsDN. Perivascular space fluid contributes to diffusion tensor imaging changes in white matter. *Neuroimage*. 2019;197(243-254

Setsompop K, Gagoski BA, Polimeni JR, Witzel T, Wedeen VJ, Wald LL. Blipped-controlled aliasing in parallel imaging for simultaneous multislice echo planar imaging with reduced g-factor penalty. *Mag Reson Med*. 2012;67(5):1210-1224

Shekar N, Biswas D, Kim A, Rendi M, Nilsson M, Bryskhe K, Lasic S, Partridge S. Apparent Exchange Rate Mapping with Diffusion MRI: A Novel Marker For In Vivo Breast Cancer Characterization. In Proceedings of the 27th Annual Meeting of ISMRM, Montreal, QC, Canada, 2019, p 1863. 2021;

Shemesh N, Jespersen SN, Alexander DC, Cohen Y, Drobnjak I, Dyrby TB, Finsterbusch J, Koch MA, Kuder T, Laun F. Conventions and nomenclature for double diffusion encoding NMR and MRI. *Magnetic resonance in medicine*. 2016;75(1):82-87

Shemesh N, Özarslan E, Komlosh ME, Basser PJ, Cohen Y. From single-pulsed field gradient to double-pulsed field gradient MR: gleaning new microstructural information and developing new forms of contrast in MRI. *NMR in Biomedicine*. 2010;23(7):757-780

Sjölund J, Szczepankiewicz F, Nilsson M, Topgaard D, Westin C-F, Knutsson H. Constrained optimization of gradient waveforms for generalized diffusion encoding. *Journal of Magnetic Resonance*. 2015;261(157-168

Slator PJ, Hutter J, Marinescu RV, Palombo M, Young AL, Jackson LH, Ho A, Chappell LC, Rutherford M, Hajnal JV. InSpect: INtegrated SPECTral component estimation and mapping for multi-contrast microstructural MRI. International Conference on Information Processing in Medical Imaging. 2019.

Sofroniew MV, Vinters HV. Astrocytes: biology and pathology. *Acta neuropathologica*. 2010;119(1):7-35

Stejskal E, Tanner J. Spin diffusion measurements: spin echoes in the presence of a time-dependent field gradient. *The journal of chemical physics*. 1965a;42(1):288-292

Stejskal EO, Tanner JE. Spin diffusion measurements: spin echoes in the presence of a time-dependent field gradient. *The journal of chemical physics*. 1965b;42(1):288-292

Stepišnik J. Time-dependent self-diffusion by NMR spin-echo. *Physica B: Condensed Matter*. 1993;183(4):343-350

Stikov N, Campbell JS, Stroh T, Lavelée M, Frey S, Novek J, Nuara S, Ho M-K, Bedell BJ, Dougherty RF. In vivo histology of the myelin g-ratio with magnetic resonance imaging. *Neuroimage*. 2015;118(397-405

Stikov N, Perry LM, Mezer A, Rykhlevskaia E, Wandell BA, Pauly JM, Dougherty RF. Bound pool fractions complement diffusion measures to describe white matter micro and macrostructure. *Neuroimage*. 2011;54(2):1112-1121

Sundgren P, Dong Q, Gomez-Hassan D, Mukherji S, Maly P, Welsh R. Diffusion tensor imaging of the brain: review of clinical applications. *Neuroradiology*. 2004;46(5):339-350

Syková E, Nicholson C. Diffusion in brain extracellular space. *Physiological reviews*. 2008;88(4):1277-1340

Szafer A, Zhong J, Anderson AW, Gore JC. Diffusion-weighted imaging in tissues: Theoretical models. *NMR in Biomedicine*. 1995;8(7):289-296

Szczepankiewicz F, Lasič S, van Westen D, Sundgren PC, Englund E, Westin C-F, Ståhlberg F, Lätt J, Topgaard D, Nilsson M. Quantification of microscopic diffusion anisotropy disentangles effects of orientation dispersion from microstructure: Applications in healthy volunteers and in brain tumors. *Neuroimage*. 2015;104(241-252

Szczepankiewicz F, Nilsson M. Maxwell-compensated waveform design for asymmetric diffusion encoding. Accepted for the 24th Annual Meeting of ISMRM, Paris, France, 2018.

Szczepankiewicz F, Sjölund J, Ståhlberg F, Lätt J, Nilsson M. Whole-brain diffusional variance decomposition (DIVIDE): Demonstration of technical feasibility at clinical MRI systems. *arXiv preprint arXiv:1612.06741*. 2016a;

Szczepankiewicz F, van Westen D, Englund E, Westin C-F, Ståhlberg F, Lätt J, Sundgren PC, Nilsson M. The link between diffusion MRI and tumor heterogeneity: Mapping cell eccentricity and density by diffusional variance decomposition (DIVIDE). *NeuroImage*. 2016b;142(522-532

Szczepankiewicz F, Westin C-F, Nilsson M. Gradient waveform design for tensor-valued encoding in diffusion MRI. *Journal of Neuroscience Methods*. 2021;109007

Tariq M, Schneider T, Alexander DC, Wheeler-Kingshott CAG, Zhang H. Bingham–NODDI: mapping anisotropic orientation dispersion of neurites using diffusion MRI. *NeuroImage*. 2016;133(207-223

Topgaard D. Multidimensional diffusion MRI. *Journal of Magnetic Resonance*. 2017;275(98-113

Trapp BD, Kidd GJ (2004). Structure of the myelinated axon. Myelin biology and disorders, Elsevier: 3-27.

Ueda T, Yuh WT, Maley JE, Quets JP, Hahn PY, Magnotta VA. Outcome of acute ischemic lesions evaluated by diffusion and perfusion MR imaging. *AJNR Am*. 1999;20(6):983-989

Van Harreveld A, Crowell J, Malhotra S. A study of extracellular space in central nervous tissue by freeze-substitution. *The Journal of cell biology*. 1965;25(1):117-137

Van Kampen NG (1992). Stochastic processes in physics and chemistry, Elsevier.

Veraart J, Fieremans E, Novikov DS. On the scaling behavior of water diffusion in human brain white matter. *NeuroImage*. 2019;185(379-387

Veraart J, Novikov DS, Fieremans E. TE dependent Diffusion Imaging (TEdDI) distinguishes between compartmental T2 relaxation times. *Neuroimage*. 2017;

Veraart J, Nunes D, Rudrapatna U, Fieremans E, Jones DK, Novikov DS, Shemesh N. Noninvasive quantification of axon radii using diffusion MRI. *Elife*. 2020;9(e49855

Vogt O. Die myeloarchitektonische Felderung des menschlichen Stirnhirns. *J Psychol Neurol*. 1910;15(4/5):221-232

Wang Z, Zhang S, Liu C, Yao Y, Shi J, Zhang J, Qin Y, Zhu W. A study of neurite orientation dispersion and density imaging in ischemic stroke. *Magnetic resonance imaging*. 2019;57(28-33

Weerasinghe P, Hallock S, Brown RE, Loose DS, Buja LM. A model for cardiomyocyte cell death: insights into mechanisms of oncosis. *Experimental and molecular pathology*. 2013;94(1):289-300

Weigel M, Hennig J. Contrast behavior and relaxation effects of conventional and hyperecho-turbo spin echo sequences at 1.5 and 3 T. *Magnetic Resonance in Medicine: An Official Journal of the International Society for Magnetic Resonance in Medicine*. 2006;55(4):826-835

Wen Q, Kelley DA, Banerjee S, Lupo JM, Chang SM, Xu D, Hess CP, Nelson SJ. Clinically feasible NODDI characterization of glioma using multiband EPI at 7 T. *NeuroImage: Clinical*. 2015;9(291-299

Werring D, Clark C, Barker G, Thompson A, Miller D. Diffusion tensor imaging of lesions and normal-appearing white matter in multiple sclerosis. *Neurology*. 1999;52(8):1626-1626

Westin C-F, Knutsson H, Pasternak O, Szczepankiewicz F, Özarslan E, van Westen D, Mattisson C, Bogren M, O'Donnell LJ, Kubicki M. Q-space trajectory imaging for multidimensional diffusion MRI of the human brain. *NeuroImage*. 2016;135(345-362

Westin C-F, Szczepankiewicz F, Pasternak O, Özarslan E, Topgaard D, Knutsson H, Nilsson M. Measurement tensors in diffusion MRI: generalizing the concept of diffusion encoding. International Conference on Medical Image Computing and Computer-Assisted Intervention, 2014

White NS, Leergaard TB, D'Arceuil H, Bjaalie JG, Dale AM. Probing tissue microstructure with restriction spectrum imaging: histological and theoretical validation. *Human brain mapping*. 2013;34(2):327-346

Whittall KP, Mackay AL, Graeb DA, Nugent RA, Li DK, Paty DW. In vivo measurement of T2 distributions and water contents in normal human brain. *Magnetic Resonance in Medicine*. 1997;37(1):34-43

Winston GP, Micallef C, Symms MR, Alexander DC, Duncan JS, Zhang H. Advanced diffusion imaging sequences could aid assessing patients with focal cortical dysplasia and epilepsy. *Epilepsy research*. 2014;108(2):336-339

Wong EC, Cox RW, Song AW. Optimized isotropic diffusion weighting. *Magnetic resonance in medicine*. 1995;34(2):139-143

Xu J, Li H, Harkins KD, Jiang X, Xie J, Kang H, Does MD, Gore JC. Mapping mean axon diameter and axonal volume fraction by MRI using temporal diffusion spectroscopy. *NeuroImage*. 2014;103(10-19

Yang B, Verkman A. Urea transporter UT3 functions as an efficient water channel: direct evidence for a common water/urea pathway. *Journal of Biological Chemistry*. 1998;273(16):9369-9372

Yang DM, Huettner JE, Bretthorst GL, Neil JJ, Garbow JR, Ackerman JJ. Intracellular water preexchange lifetime in neurons and astrocytes. *Magnetic resonance in medicine*. 2018;79(3):1616-1627

Zatorre RJ, Fields RD, Johansen-Berg H. Plasticity in gray and white: neuroimaging changes in brain structure during learning. *Nature neuroscience*. 2012;15(4):528-536

Zelinka I (2004). SOMA—self-organizing migrating algorithm. New optimization techniques in engineering, Springer: 167-217.

Zhang H, Schneider T, Wheeler-Kingshott CA, Alexander DC. NODDI: practical in vivo neurite orientation dispersion and density imaging of the human brain. *Neuroimage*. 2012;61(4):1000-1016

Zhang J, Lemberskiy G, Moy L, Fieremans E, Novikov DS, Kim SG. Measurement of cellular-interstitial water exchange time in tumors based on diffusion-time-dependent diffusional kurtosis imaging. *NMR in Biomedicine*. 2021;34(6):e4496

Zhao J, Li J-b, Wang J-y, Wang Y-l, Liu D-w, Li X-b, Song Y-k, Tian Y-s, Yan X, Li Z-h. Quantitative analysis of neurite orientation dispersion and density imaging in grading gliomas and detecting IDH-1 gene mutation status. *NeuroImage: Clinical*. 2018;19(174-181

Printed by Media-Tryck, Lund 2021 NORDIC SWAN ECOLABEL 3041 0903

FACULTY
OF SCIENCE

Lund University
Clinical Sciences Lund
Department of Medical Radiation Physics
ISBN 978-91-8039-037-8